REMOVAL OF DYES AND BACTERIA FROM WASTEWATER USING GREEN SYNTHESISED METAL DECORATED CARBON BASED MATERIALS

MASTER OF SCIENCE IN CHEMISTRY

N.M NGOEPE

2021

REMOVAL OF DYES AND BACTERIA FROM WASTEWATER USING GREEN SYNTHESISED METAL DECORATED CARBON BASED MATERIALS

BY

NKGAETSI MARIUS NGOEPE

A DISSERTATION SUBMITTED FOR DEGREE OF MASTER SCIENCE IN CHEMISTRY, SCHOOL OF PHYSICAL AND MINERAL, FACULTY OF SCIENCE AND AGRICULTURE, UNIVERSITY OF LIMPOPO

Supervisor: Dr NC HINTSHO-MBITA

2021

Declaration

I declare that this dissertation titled, ***'Removal of dyes and bacteria from wastewater using green synthesised metal decorated carbon based materials'***, is my own, unaided work. It is being submitted for the degree of Master of Science in Chemistry at the University of Limpopo. It has not been submitted before for any degree or examination in any other university.

Ngoepe NM (Mr) **12/04/2021**

Date

Signature……

Abstract

Water pollution associated with dyes and bacteria has become a concern to researchers due to lack of quality sanitation. South Africa falls amongst the water scarce countries. Thus, it is important to develop materials that can effectively remove a variety of pollutants such as dyes and bacteria. Titanium dioxide (TiO_2) and Zinc Oxide (ZnO) are materials that have been shown to have great potential in removing these pollutants since they have both the antibacterial and photocatalytic properties. However, due to their large bandgap, fast recombination rate, selective activity and the use of toxic solvents during the synthesis, a need was identified to improve these materials. In this study, the use of *Monsonia burkeana (MB)* plant extract for the synthesis of TiO_2 and ZnO was conducted, to ensure that environmentally safe products were produced and to assist in the antibacterial activity. Also, carbon nanomaterials were loaded on these metal oxides to assist with the reduction of the recombination rate and increase the active sites to ensure that an enhanced photodegradation process took place. Green synthesised TiO_2 and ZnO as antibacterial agents and photocatalyst were investigated and compared. Moreover, carbon based materials decorated with green synthesised metal oxides for photocatalytic degradation of dyes was also conducted.

In the first section, TiO_2 and ZnO nanoparticles were synthesised using *MB* extract as a reducing agent. The synthesised TiO_2 and ZnO nanoparticles were characterised using UV-vis, FTIR, TEM, SAED, SEM, XRD and TGA. These materials were then tested for their antibacterial and photocatalytic potential. From the results, LC-MS and FTIR provided evidence of the compounds, functional groups and elements that contributed to the mechanism of metal oxide formation. The UV-vis of TiO_2 and ZnO nanoparticles exhibited absorbance peaks at 327 and 325 nm, respectively, confirming their formation. In support, FTIR showed vibration bands at the fingerprint region belonging to the metal oxides. SEM showed a spherical shape of TiO_2 nanoparticles whereas ZnO nanoparticles exhibited a hexagonal shape. Particle size analysis showed that ZnO nanoparticles had a broad size distribution from 5 to 35 nm and TiO_2 had a distribution size from 2 to 18 nm. Thereafter, the metal oxides were tested for their antibacterial and photocatalytic activity. Upon testing their antibacterial potential, ZnO nanoparticles were active against all the four bacterial strains, *Staphylococcus*

aureus, *Pseudomonas aeruginosa, Enterococcus faecalis* and *Escherichia coli*, while for TiO_2 nanoparticles, the strains were resistant and only partially active against *Escherichia coli*. The water samples collected from tap, sewage, pond and river were tested for their presence of total pollution, *Escherichia coli,* total coliform and *Enterobacteriaceae* strains. TiO_2 nanoparticles inhibited most of the strains compared to ZnO nanoparticles. For photocatalytic degradation using Methylene blue (MB) as a model pollutant, the TiO_2 nanoparticles showed a higher photocatalytic activity than ZnO nanoparticles with a percentage degradation of 85.5% and 61.3%, respectively. The optimum degradation was obtained at pH (10), dosage (60 mg), concentration (20 ppm) and time (120 min). For reusability, the stability behaviour of TiO_2 and ZnO nanoparticles gradually decreased with an increase in the number of testing cycles. To improve the activity of TiO_2 nanoparticles, carbon based materials (Carbon spheres (CSs) and Carbon nanofibers (CNFs)) were loaded with 5, 10 and 20% of TiO_2 and tested for their photocatalytic activity. The 20%TiO_2/CSs composite, degraded 88.5% of MB in solution at 120 min. The addition of a low bandgap material, CuO on to the composites (TiO_2/CNFs and TiO_2/CSs) did not improve the photocatalytic degradation of MB. This study has shown that low cost and safe materials can be produced and can be used to inhibit and degrade various pollutants.

Dedication

I dedicate this work to my family and friends

for the support and love they have shown to me.

Acknowledgements

I would like to thank the following:

- God for the strength and protection.
- My supervisor Dr NC Hintsho-Mbita for her guidance, patience and knowledge provided throughout this study.
- The DSI/NRF Centre of Excellence in Strong materials for the financial support.
- The University of Limpopo, Department of Chemistry for the opportunity to conduct research and complete my studies with their facilities.
- Special thanks to Mathipa MM for the assistance with antibacterial activity experiments.
- Dr Z Tetana and Victor for the assistance with carbon based materials synthesis at the University of the Witwatersrand as well as their colleagues in the CATMAT group.
- My collegueas, LM Mahlaule-Glory and S Munyai for their support.
- My friends and more importantly, my family.

Publications and Presentations

Publications

- **Ngoepe, N.M.**, Mbita, Z., Mathipa, M., Mketo, N., Ntsendwana, B. and Hintsho-Mbita, N.C*., 2018. Biogenic synthesis of ZnO nanoparticles using *Monsonia burkeana* for use in photocatalytic, antibacterial and anticancer applications. *Ceramics International*, *44*(14), pp.16999-17006.

- **Ngoepe, N.M,** Mathipa M.M, Hintsho-Mbita N.C*, Biosynthesis of Titanium dioxide nanoparticles for the photodegradation of dyes and removal of bacteria, *Accepted* (Optik) https://doi.org/10.1016/j.ijleo.2020.165728

Book Chapters

- **NM Ngoepe,** MJ Hato, KD Modibane and NC Hintsho-Mbita* 2020. Biogenic Synthesis of Metal Oxide Nanoparticle Semiconductors for Wastewater Treatment. Scrivener Publishing, Chapter 1, pg. 3–32.

Presentations

- **Ngoepe N.M,** Hintsho-Mbita N.C, Biosynthesis of TiO_2 and ZnO nanostructures and their use in wastewater treatment. 2019. 10^{th} Faculty of Science and Agriculture research day. *Oral presentation*.
- **Ngoepe N.M**, Hintsho-Mbita N.C, Biosynthesis of CuO/TiO_2 nanostructures and its use in wastewater 2019. Young symposium South African Chemistry Institute, NORTH section. *Poster presentation*.
- **Ngoepe N.M**, Hintsho-Mbita N.C, Biosynthesis of TiO_2 nanoparticles via a green route for photocatalytic and antibacterial applications. 2019. Annual CoE-SM*I*AMSEN Student Presentation Workshop. *Poster presentation*.

Table of contents

List of figures

Chapter 2

Chapter 3

Chapter 4

Chapter 5

Appindices

List of tables

Chapter 2

Chapter 4

Chapter 5

Chemical compounds and Elements

Au:	Gold
C_2H_2:	Acetylene
Ca:	Calcium
CuO:	Copper oxide
Fe:	Iron
H_2:	Hydrogen
HCL:	Hydrochloric acid
HNO_3:	Nitric acid
H_2O:	Water
H_2SO_4:	Sulphuric acid
K:	Potassium
Mg:	Magnesium
Na:	Sodium
NiO:	Nickel oxide
O:	Oxygen
P:	Phosphurus
SnO_2:	Tin oxide
TiF_4:	Titanium flouride
TiO_2:	Titanium dioxide
$ZnCl_2$:	Zinc chloride
ZnO:	Zinc oxide

Abbreviations and Symbols

A:	Armstrong
a.u:	Arbitrary units
c.a:	Approximately
°C:	Degrees Celsius
CBM:	Carbon based materials
CFU/100 mL:	Colony-forming units per 100 millilitres
CNFs:	Carbon nanofibers
CNTs:	Carbon nanotubes
CSs:	Carbon spheres
CVD:	Chemical vapour deposition
EDS:	Energy dispersive spectrometer
eV:	Electron volts
FTIR:	Fourier transform infrared spectroscopy
JEOL:	Japan electron optics laboratory(s)
LC-MS:	Liquid chromatography mass spectrometer
g:	Grams
MB:	Methylene blue
mg:	Milligrams
mg/mL:	Milligram per millilitres
min:	Minutes
mL:	Millilitres

mm:	Millimetres
mL/min:	Millilitres per minute
MWCNTs:	Multi walled carbon nanotubes
nm:	Nanometre
ppm:	Parts per million
RSA:	Republic of South Africa
s:	Seconds
SEM:	Scanning electron microscopy
TEM:	Transmission electron microscopy
TGA:	Thermogravimetric analysis
USA:	United State of America
UV-vis:	Ultraviolet-visible spectroscopy
WHO:	World Health Organisation
XRD:	X-ray diffraction
%:	Percentage
ɵ:	Theta

CHAPTER 1

Overview and scope

1.1. Introduction

South Africa is considered one of the water scarce nations even though water is abundant on earth [1]. The existence of dyes and microorganisms in wastewater has resulted in a negative impact on human beings in terms of health disorders and to aquatic life [2]. The treatment of wastewater is a major concern to researchers since human survival and health depends on its quality.

Carbon nanomaterials are amongst the well-studied materials since the landmark discovery that was reported by Ijima in 1991 [3]. They have been used in several applications including water treatment, due to their impressive properties. These materials have also been shown to be good support materials for semiconductors with good photocatalytic activity because they are chemically stable, have high mechanical strength and because of their unique large surface area, they can assist in the adsorption of the reacting species [4]. All these qualities allow them to form a good photocatalysts composite with metal oxide nanostructures.

Plant materials have been shown to have traits that could be incorporated onto nanostructures during their synthesis using the green chemistry route. Green chemistry involves the invention, designing and development of processes that are environmentally friendly. It is used to avoid the use of toxic and expensive chemicals since it is eco-friendly, cost effective and simple [5, 6]. The biosynthesis approach uses enzymes [7], fungus [8], bacteria [9] and plant extracts [10] as a medium for the reduction of the metal precursor. Enzymes and bacteria consist of bioactive compounds that are able to act as reducing, stabilising and capping agents. The plant extracts on the other hand use phytochemicals that are present for their reduction process [7, 8, 9, 10].

In this study, biological synthesis was conducted using the *Monsonia burkeana (MB)* plant extract, since it has been shown to contain phytochemicals that can reduce the metal salts to metal oxide. Tshivhandekano *et al*., [11] reported on the comparison of bush tea and *Monsonia burkeana* (special tea), exhibiting some of the compounds

such as tannin, phenols etc. The metal oxides were synthesised and incorporated within the carbon nanomaterials to investigate the photocatalytic degradation of methylene blue dye in water and assist in the removal of common bacterial strains.

1.2. Background

Dyes and bacteria stand in the centre of water contaminants that cause a serious concern in society. Nonetheless, they differ in terms of occurrence, bacteria results from animal or human waste, by contrast dyes are effluents generated from industries including textile, leather, paper, printing and so on [12, 13, 14, 15, 16, 17]. The end results are that they form part of wastewater and river water. As they pose a threat to society, they also serve a very important purpose. Bacteria such as *E. coli*, *S. aureus* and *E. facaelis* serve as fatal bacterial indicators present in water [13]. On the other hand, dyes are heavily used in the industrial sectors that contribute to the economy [18].

Both contaminants are toxic, carcinogenic and mutagenic towards human beings [14]. The World Health Organisation (WHO) estimated that about one million people die each year due to lack of quality sanitation [19]. The production of dyes was approximated to be 7×10^5 to 1×10^6 tons annually with more than 100,000 economical dyes generated worldwide [20]. Almost, 15% of these dyes are lost with influents during the industrial processes, resulting into large quantities of wastewater discharged into nearby water [20]. Regarding bacteria, in a developing country such as South Africa, the required water quality is zero (0) CFU/100 ml for domestic use, 130 CFU/100 ml for recreational use and 200 CFU/100 ml for agricultural use [19, 2, 21, 22, 23].

Several studies have been done to assist in finding proper and adaptable solutions to resolve the problem by developing suitable methods and materials to work hand in hand with the emerging technology. Nanostructured materials have been identified as some of the most promising and suitable photocatalytic semiconductors [24]. Semiconductor materials often consist of physicochemical properties such as generation of electron-hole pair under irradiation wavelength, redox potential, and adsorption ability which makes them suitable for photocatalytic degradation [25]. Generally, there are two types of semiconductors namely p-type and n-type. The p-type semiconductor suffers from instability, photocorrosion and reconstruction of itself

during photocatalysis [26, 27]. For photocatalytic studies, the semiconductors employed are n-type e.g. SnO_2 [28], ZnO [29] and TiO_2 [30] *etc* due to their cost-effective stability, non-toxicity and photocorrosion resistance.

Semiconductors offer excellent optical properties, electronic and photocatalytic activity that depends on size and crystalline shape. TiO_2 and ZnO, have been recognised amongst the most photocatalytic semiconductors. These materials share similar properties, whereby ZnO has a wide band gap of 3.37 eV which is close to the TiO_2 band gap of 3.2 eV [6, 31, 32, 33]. Although, they are good photocatalysts, having a large bandgap has limited their ability to degrade a wide range of pollutants. Other metal oxides such as CuO with lower band gap have been used as good dopants to reduce the energy gap [34]. These nanostructures are synthesised easily using the green route since they require a few steps and can be manufactured at a low cost. Also, with this method more properties are incorporated on the material.

Plants such as *Monsonia burkeana* can be used for the green route. This plant consists of compounds that can act as reducing or capping agents [11]. *Monsonia burkeana* is a herbal tea mostly used in South Africa and locally referred to as special tea. It is concentrated more in the northern side (Limpopo) of South Africa. Several studies have shown that the constituents of *M. burkeana* includes tannis, phenols and antioxidants [35, 36, 37]. These compounds are responsible for the formation of metal oxide nanostructures and can be used as antibacterial agents and photocatalysts. As a photocatalyst, there are ways of enhancing the photocatalytic activity through other semiconductor and carbon based materials. Carbon based materials have been used in composite chemistry for wastewater remediation [38].

Carbon based metal oxide composite have gained a lot of attention in solving water pollution. The carbon based materials are used as a support to metal oxides for photocatalytic degradation of organic dyes [38, 39]. Some of these carbon based materials are carbon nanotubes, graphene, carbon nanospheres and carbon nanofibers. Many allotropes are formed because of the diversity bonding of carbon [40]. These depend on the hybridization, physical and chemical properties of the carbon atom. For diamond and graphite, the sp^3 hybridization for diamond is the hardest carbon material which exists in nature, forming a 3D network and graphite hybridization is sp^2 carbon forming 2D planar sheets [40, 41]. This study advances on

the combination of carbon-based nanomaterials and green synthesised metal oxides nanostructures. The idea is to improve the efficiency of metal oxides nanostructures towards degradation of organic dyes.

1.3. Problem statement

There is an increase in the demand for clean water throughout the world as freshwater sources are depleting due to prolonged droughts, population growth, climate change, and strict water quality standards [1]. Furthermore, access to clean and healthy water is one of the biggest problems faced by many communities such as the Limpopo province. Dyes such as methylene blue produced at textile industries are carcinogenic while bacteria such as *Escherichia coli* cause diarrhoea and abdominal pain with bloody stools [42]. There is a need for low cost materials that are able to degrade various harmful pollutants and can be applied in several fields.

In terms of removing dyes, several methods such as microbial degradation [43], flocculation [44] and adsorption [45] have been used. However, these methods produce secondary pollutants that can be environmentally destructive. The most common and reported method for the removal of dyes has been photocatalytic degradation [46]. The use of this method is preferred because it converts contaminants into less harmful molecules. It is simple, effective, economical and different composite materials can be used as photocatalysts [47]. The two most commercially used nanostructures have been successfully used as photocatalysts and antibacterial agents.

TiO_2 and ZnO are some of the preferred nanomaterials that have been shown to be both photocatalytic and have antibacterial properties, since they are less toxic, Though, that has been the case these materials have a limited surface area and also the metal oxide synthesised via chemical methods tends to have antibacterial activity against a limited number of strains [48, 49]. The limitations associated with the materials are selectivity, stability, high recombination rate and a large band gap [50, 51].

Thus, in this study these materials were synthesised using the green route. This was done to ensure that the materials would be environmentally friendly and have traits that would be incorporated in an effort to expand on the biological properties. Also, upon loading these materials with CuO and on carbon nanomaterials, their

recombination rate would be reduced and thus potentially increase the photocatalytic activity.

1.4. Research questions

1. Can TiO_2 and ZnO nanoparticles be formed via the green route using *Monsonia Burkeana*
2. Can TiO_2 and ZnO nanoparticles have enhanced antibacterial properties from *Monsonia Burkeana* synthesis?
3. Can green synthesised TiO_2 and ZnO nanoparticles maintain their photocatalytic activity?
4. What conditions can produce high percentage of MB degradation?
5. Will the addition of CSs and CNFs improve the photodegradation ability of the metal oxides?

1.5. Aim and objectives

1.5.1. Aim

The aim of this work was to investigate the photocatalytic and antibacterial activity of green synthesised metal decorated carbon based materials.

1.5.2. Objectives

The objectives of the study were to

(i) synthesise ZnO, TiO_2 and CuO metal oxide using *Monsonia burkeana*/Carbon based material.

(ii) characterise the synthesised materials using the following instruments: Scanning Electron Microscopy (SEM), Transmission Electron Microscopy (TEM), X-ray Diffraction (XRD), Thermal Gravimetric Analysis (TGA), Fourier Transform Infrared Spectroscopy (FTIR), Ultraviolet-Visible spectroscopy (UV-Vis).

(iii) evaluate the efficiency of the green synthesised materials on simulated wastewater for the removal of dyes and microbes.

(iv) determine the optimum variable conditions for photocatalytic degradation such as pH, dosage, concentration and time.

(v) conduct reusability studies of the photocatalysts using the optimum conditions.

(vi) determine the antibacterial potential of the nanoparticles on the bacterial strains *Staphylococcus aureus*, *Pseudomonas aeruginosa, Enterococcus faecalis* and *Escherichia coli*.

(vii) check the effect of carbon-based nanomaterials (CNFs and CSs) and CuO on the chosen metal oxides for photocatalytic activity.

1.6. Structure of the dissertation

Chapter 1, presents the introduction based on the background, motivation, problem statement and objectives behind this dissertation.

In chapter 2, a short literature review on green chemistry, metal oxide classifications, modification with functionalised carbon nanomaterials, photocatalysis, antibacterial studies and characterisation techniques are discussed.

Chapter 3, focusses on the synthesis methods, and characterisation techniques for the synthesised materials and the use of materials in antibacterial and photocatalysis application.

Chapter 4, presents the comparison of green synthesised ZnO and TiO_2 nanoparticles. Their antibacterial and photocatalytic ability is investigated using simulated wastewater consisting of dyes for photocatalysis and various bacterial strains for antibacterial activity. In context, the best photocatalysts is deduced.

Chapter 5, presents the synthesis of the carbon based material composite with the better nanocatalyst deduced in chapter 4. The percentage loading of nanocatalyst on carbon based materials is varied. Furthermore, different loadings of CuO are loaded on the best performed nanocatalyst/carbon based materials composite. The composites are tested for their photocatalytic activity.

Chapter 6, gives the general conclusion and recommendations for future work related to the presented study.

CHAPTER 2

Literature review

This chapter provides a background on the contaminants of focus in the study, the treatment strategies and the methods used for the green synthesis of these materials. It also discusses the modification strategies through coupling with other semiconductors and carbon based materials. Lastly, the review highlights the characterisation methods used.

2. Introduction

Environmental pollution has become a concern for researchers, thus alternative methods are being explored to provide for safe and quality water. Industries such as cosmetics, paper and textile, produce wastewater containing a number of organic dyes such as methylene blue (MB), methyl orange (MO) and rhodamine blue (RhB) [10, 17]. These effluents contaminate natural reservoirs such as rivers, lakes and dams. The need for exploring reliable economic methods for treating water has risen greatly. Several methods such as microbial degradation, reverse osmosis, adsorption and photocatalysis to mention a few, have been used to eliminate organic dyes from wastewater [52, 53, 54, 55]. These methods have one form of a drawback or the other, for example microbial degradation is time consuming, ineffective with some of the dyes and some carcinogenic materials can be produced [56]. On the other hand, in reverse osmosis, pre-treatment of the membrane is required before use [57]. Other methods such as adsorption have been highly explored, their regeneration process is complicated [58]. However, a common drawback amongst all these methods is that they transform organic dyes from one phase to another and do not eliminate these pollutants completely, thereby creating secondary pollutants. In photocatalysis, the main advantage it has over the other methods is that it dissociates organic dyes to less harmful intermediates. Photocatalysis is an advanced oxidation process that is mostly used since it is inexpensive and eco-friendly [59]. In this method, semiconductor materials are the preferred candidates for advanced oxidation process [7]. TiO_2 and ZnO have been recognised amongst the most photocatalytic semiconductors. Although, they are good photocatalysts, their ability to degrade a wide variety of pollutants has been limited. Materials such as CuO with a lower band

gap and carbon based materials have been used as dopants to reduce the energy gap and as supporting materials, respectively [62, 63]. Furthermore, TiO_2 and ZnO are important in microorganism application as well, because of their reported antibacterial properties [64]. Various methods have been used to produce metal oxide nanostructures namely chemical, physical and green methods. Chemical methods involve wet chemical [65], co-precipitation [66] and spray pyrolysis [67]. The process involves mixing of a solvent with the metal salt, casting, gelation, aging, drying and densification [68]. During the chemical synthesis, the reagents that are used are hazardous to humans and the environment. Physical methods though involve molecular beam epitaxy and pulsed laser deposition [69, 70]. During this process, a milling technique such as crushing metal ions with thermal stress and energy is used, thus requiring high energy and expensive equipment [68]. Due to the above-mentioned reasons, environmentally friendly procedures are needed to avoid the destruction of the ecosystem. In an effort to mitigate these, eco-friendly methods have been explored, such as the synthesis of nanostructures using the green technology. These nanostructures are of interest because they are cost effective and easy to produce. From the word green synthesis, it can be defined as the synthesis of various nanostructures using microorganisms such as bacteria and fungi and plants. [71, 72]. Recently, the move towards eco-friendly and keeping the environment safe from pollutants has been given considerable attention, hence the number of reports on green synthesis technology had increased [9, 10, 31]. A free pollutant water stream environment is the purpose of this study. Hence, key aspects of keeping the environment clean are discussed in this chapter as indicated by flow chart in Figure 2.1. In the next section, dye and bacterial contaminants in water and their effect on the environment are discussed.

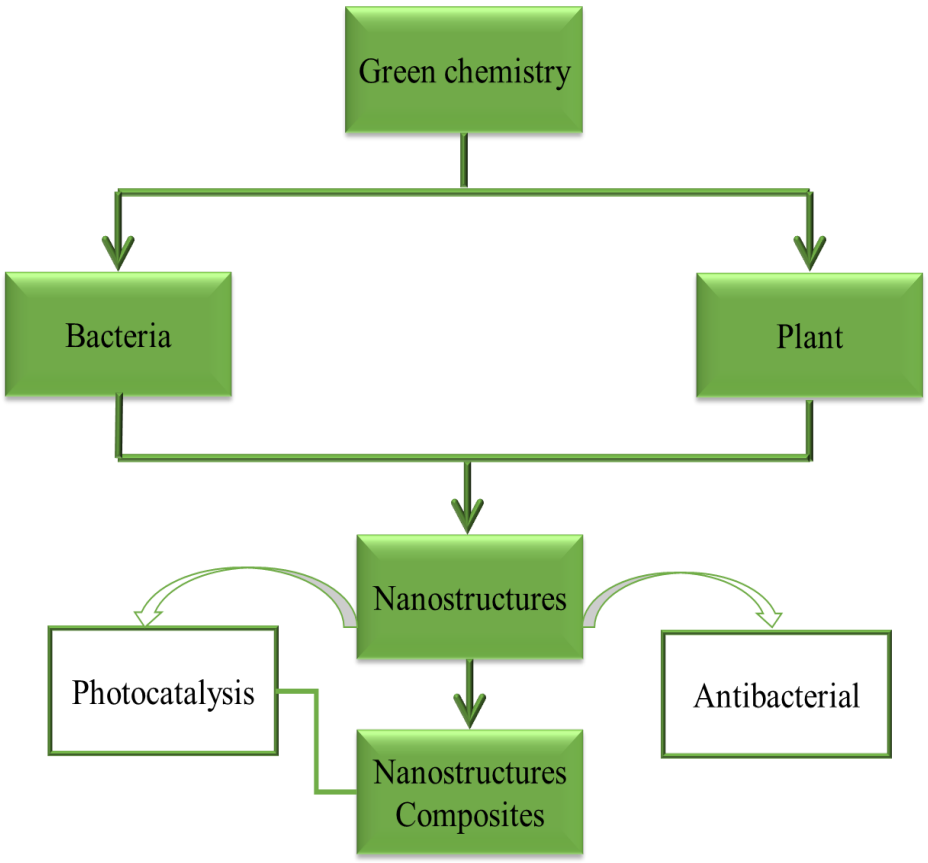

Figure 2.1: Flow chart of biosynthesis to photocatalysis and antibacterial of nanostructures and their composites.

2.1. Contaminants

Contaminants are generated through various activies such as waste disposal and effluents from households, agriculture and industries. They can contaminate water and land, affecting the humans and environment negatively. Dyes can be considered contaminants in water.

2.1.1. Dyes

A dye is a coloured substance that absorbs light at the visible region of a spectrum. The dye substances exist naturally or via a synthetic route. Natural sources originate from inorganic materials, minerals, stones and metal salts. Dyes are used in our daily life for industrial purposes. They are classified by a unique chemistry, nature of structure and the functional groups around [73, 74] as indicated in Figure 2.2. The dyes are utilised in the industrial sectors such as textiles, paper, rubber, printing, cosmetics, leather, pharmaceutics and wood preservation [10, 17]. These dyes are

lost with effluents during the industrial processes, resulting into large quantities of wastewater discharged into nearby water. The aqua species, animals and human being's health are at risk. They have carcinogenic and mutagenic effect, thus causing skin irritation, blood disorders, liver and kidney damage with the poisoning of the central nervous system and reproductive system in humans [75, 76]. The colour content of dyes hinders the sunlight from penetrating through water. Furthermore, the sunlight it is absorbed or reflected by dyes. As a result, the survival of aqua species is compromised [77].

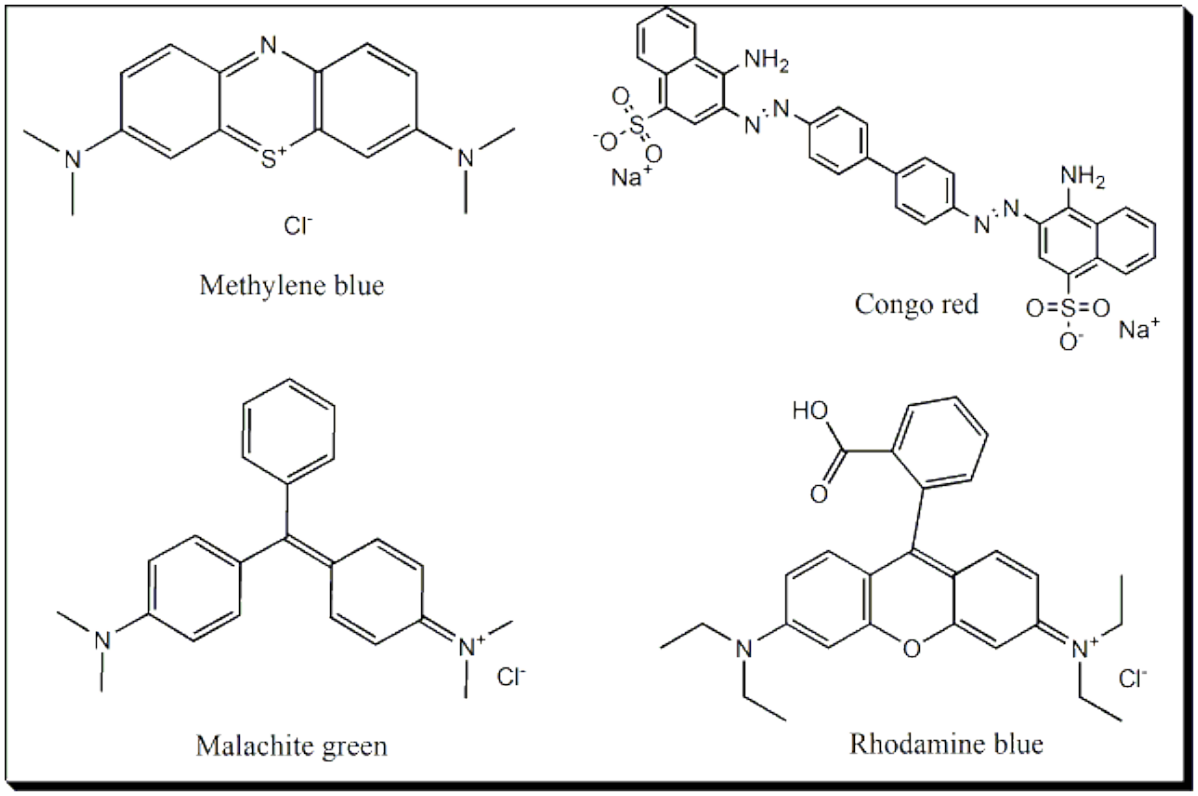

Figure 2.2: Some of the organic pollutants found in wastewater and their structure.

2.1.2. Bacteria

Bacteria are single-celled microorganisms that are a build-up of the cell wall, cell membrane and cytoplasm [78]. The cell wall serves as a cover to cell membrane, as well as maintaining osmotic pressure and the cell shape of the cytoplasm [79]. Classified into genera and species, for example, *Enterococcus faecalis*, *Enterococcus* is assigned as the genus while *faecalis* is designated as the species. They are categorised as either gram negative (*E. coli* and *P. aeruginosa*) or positive bacteria

(*S. aureus* and *E. faecalis*). Gram positive bacteria contain a peptidoglycan thick layer in the cell wall, while gram negative bacteria have peptidoglycan thin layer in the cell wall [80]. Bacteria are few of the pollutants traced in wastewater. Sources of bacteria might be agricultural activities and septic tanks for wastewater [81]. These microorganisms affect living organisms negatively. Contaminated water has been used due to lack of quality sanitation access in developing countries, which has generated a serious concern [82]. However, their quality depends on the CFU/100 mL concerning the specific bacteria. If the water quality exceeds the accepted permissible levels, it will be a problem to society. Exposure to this exceeding level of quality water has put consumers' health at risk with diseases such as cholera and diarrhoea [83]. Hence, researchers are developing materials that can be suitable for the water pollution application.

2.2. Treatment of contaminants

In an effort to ensure quality water, metal oxide nanostructures have been taken under consideration as putative candidates for photocatalysis and bacteria inhibition. Owing to their physiochemical properties, as well as antimicrobial, anticancer, catalysing and optical properties it is important to prepare metal oxide nanostructures with well-defined sizes and shape [84, 85, 86, 87]. This section outlines the activity of nanostructures in their application of photocatalysis and antibacterial.

2.2.1. Photocatalytic degradation of dyes

For decades, methods such as adsorption, co-agulation, membrane separation, ion exchange, microbial degradation as well as catalytic degradation have been applied for the removal of dyes from wastewater [56]. These methods were developed due to increasing population and pacing industrialisation that caused a decline in quality water. The advantages and disadvantages of these methods are tabulated in Table 2.1. The photocatalysis process offers a lot of advantages over other methods. It includes multiple processes such adsorption and production of radicals which contribute to the elimination of organic dyes in water. The process mineralizes organic pollutants to less harmful constituents while other methods concentrate on the organic pollutants which does not destroy or eliminate dyes completely.

Table 2.1 Advantages and disadvantages of removal methods for dyes [56].

Method	**Advantages**	**Disadvantages**
Adsorption	Cost-effective, easy to handle the process	Not effective to all dyes, costly regeneration process, produce secondary pollutants
Coagulation	Simple to operate, economically feasible	High production of sludge and disposal issue
Membrane separation	High efficiency	Short lifespan, not effective to all dyes, require many steps
Ion exchange	Easy regeneration	Not effective to all dyes, economically unattractive
Electrochemical	Produce non-hazardous Intermediates	Electricity consumption
Photochemical	Rapid, no sludge production	Produce by-products and power consumption
Biodegradation	Economically attractive and simple	Time consuming, Require sophisticated environmental conditions
Biological Treatment	Can remove some pollutants	Not yet commercialized or upscaled
Advanced oxidation process	High effiency, rapid, formation of non-hazardous products	Sludge production, economically unfeasible, high chemical reagents and electricity consumption

Photocatalysis can be described as a rate of transformation of a chemical species initiated under the absorbed light by the photocatalyst [88]. A photocatalyst is a material that can generate electron-hole pairs under the exposure of photons when absorbed on the surface. The transformed chemical species can be organic pollutants

such as dyes. This method has been researched for decades for the degradation of organic dye pollutants from water and wastewater. It employs various semiconductor nanostructure materials such as CuO, ZnO and TiO_2. The mechanism of photocatalysis for the semiconductors follows the principle which can be defined as a redox mechanism, which is indicated in Figure 2.3. The semiconductor materials consist of two bands namely the valence band (filled with electrons before excitation) and conduction band (unoccupied before excitation). The light with a suitable amount of energy is irradiated through the dye solution aiming at the surface of the photocatalyst to excite the electrons. The excited electrons move to the conduction band generating the holes at the valence band. The electrons in the conduction band react with absorbed oxygen species to form radical oxygen. Furthermore, positively charged holes created at the valence band dissociate the absorbed water molecules to produce highly reactive hydroxyl radicals. The radicals generated degrade the dye to less harmful compounds namely, carbon dioxide and water. The electron-hole pairs and radicals produced play an important role in the performance of the semiconductor photocatalyst [89, 90].

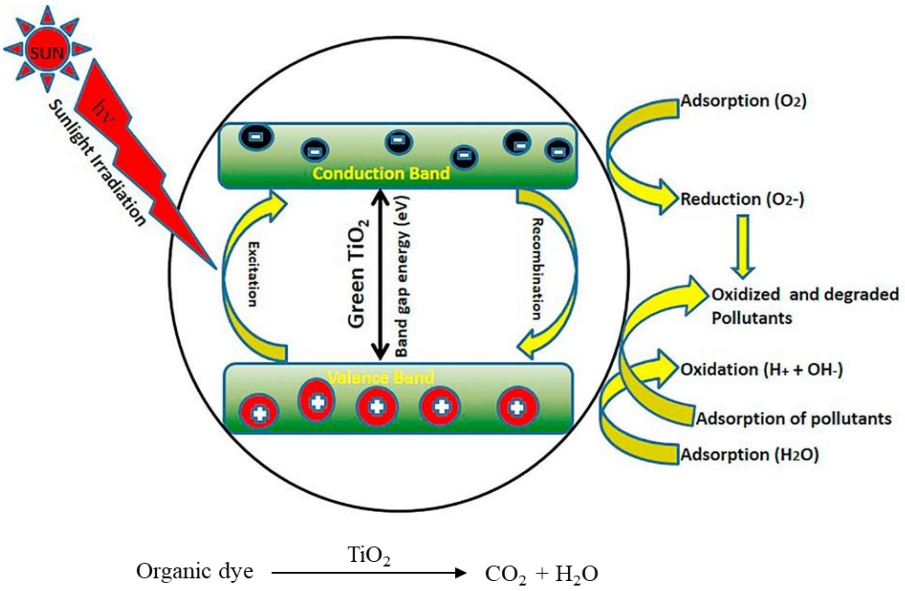

Figure 2.3: General mechanism of photocatalysis using TiO_2 nanoparticles under sunlight radiation [55].

An enormous amount of research has been done on the use of TiO_2 and ZnO nanostructures for photocatalytic degradation of organic dyes. The degradation of

organic dyes is performed in different light immersions. Lin *et al*., [91] used light (250W Hg lamp, 365 nm) to degrade methylene blue (MB) in the presence of mixed ZnO nanoparticles morphologies, depicted as quasi spherical with an average of 150 nm diameter. The nanoparticles degraded 67.8% of the MB within 60 minutes. Ishwarya *et al*., [92] investigated the photocatalytic activity of ZnO nanoparticles against MB dye using direct sunlight irradiation for 120 minutes. At the end of that period, 90.4% of MB was degraded. Siripireddy *et al*., [93] used ZnO nanoparticles to degrade methyl orange (MO) under UV irradiation. Approximately, 98.3% of MO was degraded within 50 minutes. In another study, ZnO nanoparticles degraded 98% of the dye and they also evaluated the stability of the nanoparticles. For the study, the photocatalytic activity of 94% was retained after three consecutive cycles [31]. Hiremath *et al*, [94] degraded 95% of titan yellow using nano-TiO_2 catalyst within 120 minutes via UV irradiation. Khan *et al*., [95] used the UV irradiation in the presence of bacteria mediated TiO_2 nanoparticles. TiO_2 nanoparticles were able to degrade 75% of reactive red 31 (RR31) in 3 hours. Gnanasekaran *et al*., [96] prepared CuO and ZnO where FE-SEM images displayed nanoleaves and a spherical shape, respectively. Thereafter, their activities were tested through the photocatalytic degradation of MO and MB under UV light irradiation (365 nm). ZnO was more active compared to the other metal oxides within the period of 2 hours. The superior degradation rate was inspired by the spherical shape, which was also supported by several studies [97, 98, 99]. The morphology contributed towards surface properties of the materials, promoting the performance of the materials in photocatalytic degradation. Sorbium *et al*., [100] compared the photocatalytic activity of quazi-spherical CuO nanoparticles and uniform spherical ZnO nanoparticles under simulated visible light. The results showed that ZnO exhibited a higher photocatalytic activity than CuO whereby ZnO had a percentage degradation of 93% whereas CuO had a percentage degradation of 86%.

Table 2.2 Photocatalytic activity of CuO, TiO_2 and ZnO nanostructures.

Metal oxide	Shape	Size (nm)	Dye*	Time (min)	Efficiency (%)	Light source	References
ZnO	Spherical	28 (SEM)	MB	90	92	UV light (365)	[6]
TiO_2	-	50 (TEM)	BR X-3B	90	63.4	Mercury lamp UV (250W)	[101]
ZnO	-	30 (XRD)	MB	-	81.0 92.5	UV lamp (12W)	[102]
TiO_2	Nanofibers	400±32 (FESEM)	MB	720	41.9	UV lamp (10W)	[103]
TiO_2	Spherical	21 (XRD)	MO	30	27.0	UV light (365)	[104]
TiO_2	-	20-30 (TEM)	MB RhB	240	>95.0	UV lamp (Hg 15W 362 nm)	[105]
TiO_2	Spherical	20-40 (TEM)	TY	120	95.0	UV light (125W)	
TiO_2	Spherical	20-50 (FESEM)	MB	360	95.8		[106]

			MO CV		77.5 86.7		
TiO_2	Ellipsoidal	20x40um (SEM)	RhB	120	95	-	[107]
ZnO	-	52 (XRD)	TY	60	96	Visible light	[108]
ZnO	Spherical	20-50 (TEM)	MB	90	-	Sunlight	[109]

* Methylene blue (MB), titan yellow (TY), methyl orange (MO), crystal violet (CV), rhodamine blue (RhB), phenol red (PR), Brilliant red dye (BR X3-B), Evans blue (EB).

From the reported studies, it can be seen that the efficiency of degradation differs due to factors such as complexities of organic structure [110], size and the shape of the photocatalyst as well as source of light [111]. Generally, TiO_2 and ZnO nanostructures have been shown to be preffered materials for the removal of organic dyes using photocatalysis. Moreover, the studies elucidated that these nanostructures can also be used as antibacterial agents.

2.2.1. Antibacterial activity

An antibacterial agent is a material that inhibits or destroys the bacterial growth at its growth standard conditions [112]. As mentioned in Section 2.1.2, bacteria consist of cells that channel their growth and survival [78, 79]. Since their existence affects living organisms negatively, antibacterial agents are developed to counteract their growth. Hence, the antibacterial agents' mode of growth inhibition of bacteria cell has been a centre of required understanding. Plausible mechanisms of bacteria inhibition have been reported by several authors [113, 114, 115] such as the one indicated in Figure 2.4. Although, there is still some controversy on how bacterial inhibition occurs using nanoparticles, several authors have shown that metal oxide nanostructures have a small size compared to bacterial strains which allows them to enter easily when in direct contact with the cell wall and generate reactive oxygen species, resulting in destructing the bacterial cell wall [116]. The mechanism involves the formation of ^{-}OH and O_2^{-} species from nanostructures in aquatic suspension. Thus, leading to formation of H_2O_2 from H^+ and electron participants [117]. The ^{-}OH and O_2^{-} species accumulate the surface of the cell wall while the H_2O_2 molecule has the ability to penetrate the cell wall, resulting in destructing the cell wall. Metal oxide nanostructures are positively charged, and the bacteria surface is negatively charged and unlike charges create the electrostatic force. The bond force is formed in between nanostructures and bacteria, resulting in destructing the bacterial cell wall growth [118].

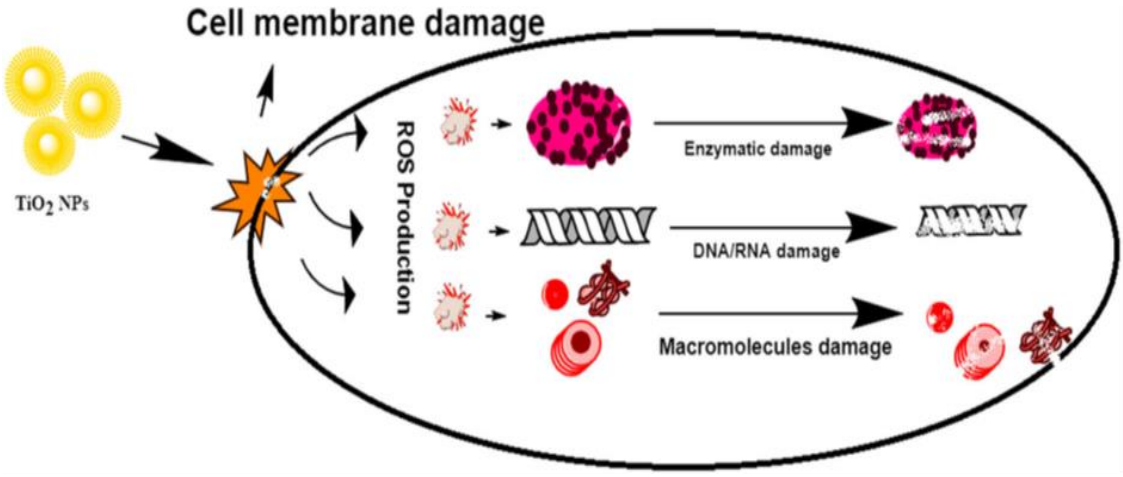

Figure 2.4: Mechanistic representation of TiO_2 semiconductor nanoparticles effect on bacteria cell [5].

Despite the antimicrobial agents' existence, some strains have shown resistance [119, 120]. Metal oxides are the proposed materials as the solution for bacterial inhibition treatment. The spherically shaped TiO_2 nanoparticles were synthesised and tested against *E. coli* and *S. aureus*. The nanoparticles were shown to be active against gram-negative and gram-positive strains [121]. This shows that the bacteria can be vulnerable against nanoparticles irrespective of the strain type. Dadi *et al*., [122] prepared CuO and ZnO nanoparticles with a size of 3 nm. Both materials were then tested against *E. coli*, *S. aureus* and *P. aeruginosa* with varying concentrations using the disk diffusion method. These materials showed a greater zone of inhibition with an increase in concentration. However, CuO nanoparticles were more active than ZnO nanoparticles. Authors pointed out that, the weaker aggregation of the CuO nanoparticles resulted in a larger contact area as the reason for more activity than ZnO nanoparticles. Sharmila *et al*., [123] prepared spherically shaped ZnO with the size of 70-75 nm. The activity of ZnO nanoparticles was tested against *B. subtilis*, *S. aureus*, *E. coli* and *P. aeruginosa* assayed using a well diffusion method. The strains showed a maximum zone of inhibition as *E. coli* (17 mm), *P. aeruginosa* (15 mm), *B. subtilis* (15 mm) and *S. aureus* (17 mm) at 100 µg of ZnO nanoparticles concentration. Amanulla *et al*., [124] prepared TiO_2 nanoparticles with a triangular shape and size ranging from 20 to 50 nm. The antibacterial activity of the TiO_2 nanoparticles was assayed by agar well diffusion against *E. coli*, *P. aeruginosa* and *S. aureus*. The nanoparticles showed a higher activity in this order *P. aeruginosa* > *E. coli* > *S. aureus.*

Table 2.3 Antibacterial activity of CuO, TiO_2 and ZnO nanostructures.

Metal Oxide	Shape	Size (nm)	Strains (ZOI mm)*	References
CuO	-	20±1.24 (TEM)	*E. coli* (20), *P. aeruginosa* (21), *B. subtilis* (24), *S. aureus* (22)	[125]
ZnO	Quazi-spherical	29.79 (TEM)	*E. coli* (7), *S. aureus* (18)	[126]
TiO_2	Spherical	20 (HRTEM)	*E. coli* (10.8), *S. aureus* (11.2) *E. faecalis* (11.4), *S. faecalis* (11.6)	[127]
ZnO	Rods	70 (SEM)	*E. coli* (11), *P. aeruginosa* (12). *S. aureus* (11), *B. ceresus* (10), *S. thermophilis* (9.0)	[128]
TiO_2	Spherical	20 (HRTEM)	*E. coli* (10.8), *S. aureus* (11.2), *E. faecalis* (11.4) *S. faecalis* (11.6)	[129]
ZnO	Spherical	2-10 (TEM)	*E. coli* (23.5), *S. aureus* (14), *S. enterica* (16)	[130]
ZnO	Spherical to nanoflowers	170-250 300-600	*E. coli* and *S. aureus* (1.6-2.4)	[131]

		185-365 (SEM)		
CuO	Nanorods	20-200 (TEM)	*S. aureus* (15.5), *E. coli* (11.0), *K. pneumonia* (13.5)	[132]
ZnO	Spherical	9-11 (HRTEM)	*S. aureus* (26), *E. coli* (26), *K. pneumonia* (25), *S. enterica* (12)	[133]

Staphylococcus aureus, Pseudomonas aeruginosa, Enterococcus faecalis, Escherichia coli, Klebsiella pneumonia and salmonella enterica.

The section addressed the critical findings of three metal oxide nanostructures activity as photocatalyst and antibacterial agents in particular ZnO and TiO_2. It was shown that the nanostructures utility depends on the stability, size as well as morphology. Hence, researchers have moved towards the use of biological-mediated synthesis, since they fit the criteria.

2.3. Synthesis methods of metal oxides nanostructures

This section discusses methods that are employed during synthesis of metal oxides, more especially ZnO nanostructures since they are mostly studied using biosynthesis and other methods. The methods of synthesis of metal oxide nanostructures decide the outcome of the morphology, structural and physiochemical features. The synthesis of nanostructures can be categorised into two major pathways namely, top down and bottom up method. Top-down methods involve the production of nanoparticles by size reduction, whereby they include synthesis using various physical and chemical methods. The approach has been shown to be slow and costly which means it cannot be used at a large scale for the production of nanoparticles [134]. The bottom-up methods use small entities, like atoms and molecules to produce nanoparticles, where the main reaction is reduction/oxidation [135]. The bottom-up approach includes chemical methods and biological-mediated synthesis.

2.3.1. Top-down method of metal oxides nanostructures synthesis

The top-down method is one of the most applicable strategies for preparing nanoparticles. The method was first introduced by Feynman [136] as a method of making particles in nanometre dimensions. In this method, mechanical devices, shaving, and milling were utilised as a strategy to produce particles through size reduction. Top down synthesis involves various physical and chemical methods.

2.3.1.1. Chemical Top-down Method

Wu *et al*, [137] used an oxidising mixture solution of DMSO and NaOCl and mixed it with a metal screw precursor. They then added HNO_3, immediately HNO_2 gas was formed which indicated the decomposition/corrosion of the screw. The temperature of decomposition was kept at 75 °C throughout. A dark brown powder alloy obtained was washed and neutralised thereafter, the nanorods of the metal alloy were formed. Navale *et al,* [138] reported the solid state method, in which they used 5 g of $Zn(NO_3)_2{\cdot}6H_2O$ as a metal precursor and mixed it with NaOH without the addition of

any other solvent. To allow the reaction to occur, the solution was stirred for 10-15 minutes. The NaOH was used as a precipitation promoter, which occurs when the sodium hydroxide comes into contact with metal precursor assisted by heat. Firstly, forms the $Zn(OH)_2$ which eventually decomposes to ZnO nanoparticles on air annealing. The characterisation using SEM and TEM showed that nanoparticles were aggregated with an average size of 37.5 nm.

2.3.1.2 Physical Top-down method

The method involves a flux material, substrate and growth temperature. Gold-catalysed plasma-assisted MBE was studied to synthesise ZnO nanobelts [69]. In this study, sapphire was utilised as a substrate, which was deposited with Au and heated until the growth temperature was reached. Afterwards, zinc flux and oxygen plasma were directed to the substrate. The obtained ZnO nanobelts were tapered, forming triangles at 750 ^oC and with an increase in temperature to 800 and 850 ^oC had almost no tapering. It shows that tapering occurs more at lower temperatures [69]. Laser ablation is one of the physical methods used to synthesise nanostructures through the reduction of size. In this method, laser ablation was used to produce colloids solution of nanostructures in a solvent. Metal ions of interest were immersed in solvents which could be ethanol, ethyl glycol or water. In a typical experiment, laser with wavelength of 1064 nm was used to synthesise ZnO nanostructures. Therefore, this implies that Zn ion plasma resonance properties appeared at that wavelength [70]. The metallic materials had plasmon resonance at different wavelengths that would allow to form their respective oxides.

These methods have been successfully used to prepare the nanoparticles. However, they involve expensive processes (instruments and time) and harsh reaction conditions (solvents and acids).

2.3.2. Bottom-up method of metal oxides nanostructures synthesis

The bottom-up methods use small entities, like atoms and molecules to produce nanoparticles, were the main reaction is reduction/oxidation. This is the most flexible method that generates pure metal oxide amongst other methods. Examples of bottom up methods include co-precipitation, sol-gel, spray pyrolysis and biological methods. The other methods excluding biological method they belong to the bottom-up chemical method.

2.3.2.1. Chemical Bottom-up Method

Sol-gel is a wet chemical technique used for the production of novel metal oxide nanostructures. The approach is useful in fabricating functionalised nanostructures, such as photocatalysts, antibacterial agents and superconductors. The pathway of synthesising nanostructures consists of the following consecutive steps, precursor solution hydrolysis, condensation, gel-formation, drying process, xerogel or aerogel and final product nanostructures. Alwan *et al*., [65] used the sol-gel to prepare ZnO nanoparticles. The zinc acetate dehydrate was dissolved in double distilled water medium. The synthesis was referred to as aqueous sol-gel method since it uses water as a medium. However, in a case of organic solvent, it was referred to as a nonaqueous sol-gel approach [65]. In a co-precipitation method, a multi-process occured simultaneously to form the nanoparticles. The processes included were nucleation, coarsening and growth. The reaction required a metal salt and a solvent. The reaction was influenced by factors such as temperature, concentration, pH and the manner in which the factors were adjusted. In a typical experiment, the metal salt solution forms metal oxide precipitates. The precipitates formed while adding a base, drop wise to the metal solution [66].

2.3.2.2. Biological Bottom-up method

Biological methods have become some of the best choices for the synthesis of nanoparticles because they are cost effective, flexible and use nontoxic reagents. These methods assist in overcoming the harmful by-products produced during the synthesis. Researchers have noted a growing need for developing eco-friendly and viable procedures of producing metal oxide semiconductors. In the greener route, microbes (bacteria and fungi) and plants parts (leaves, flowers and roots) are used to avoid usage of toxic chemicals [139]. The type of synthesis or reagents used to prepare nanostructures plays an important role in the desired application. These biological materials have been shown in anticancer and antibacterial applications [140]. Their utilisation in the synthesis of metal oxides nanostructures can also enhance their biological properties. Hence, green synthesised nanostructures are mostly utilized in anticancer and antibacterial applications. These biological materials are abundant and readily available. The presence of biomolecules in a biological material facilitates the synthesis of metal oxides. Biomolecules have been shown to have functional groups that can link with metal ions, in so doing, reducing the metal

salt. The extracts generally contain phytochemical constituents such as polyphenols, flavonoids, alkaloids, terpenoids, heterocyclic compounds and polysaccharides that can act significantly as reducing, capping and stabilizing agents [141]. The compounds found in plant extracts with functional groups NH_2 and OH are responsible for reduction of metal ions [142]. Microbial synthesis of nanostructures involves enzymes and proteins that lie between the layers of microorganisms. The mechanism involves the electrostatic force to create biosorption, extracellular complexation or precipitation of metal ion and bioaccumulation. The focus will be on green synthesis using plants and microorganisms (i.e. bacteria) as depicted in Figure 2.5 and their mechanism of formation.

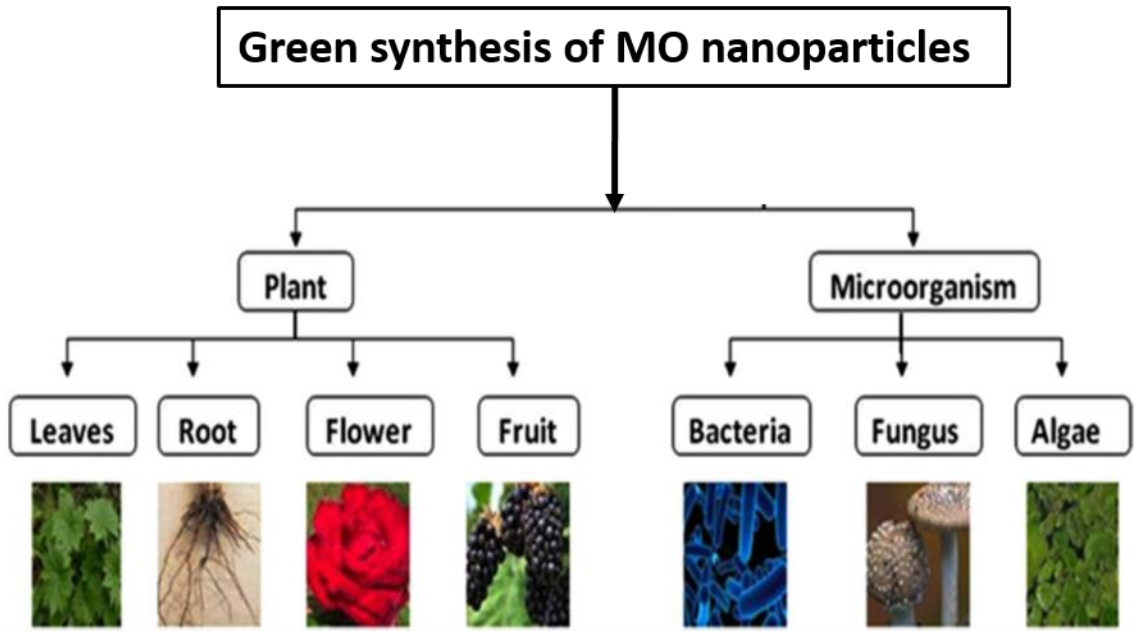

Figure 2.5: Biogenic synthesis of metal oxides (MOs) nanoparticles using plants and microorganisms.

2.3.2.2.1. Synthesis of metal oxides nanostructures using microorganisms.

Microorganisms-mediated biosynthesis forms part of a fast-growing green synthesis of metal oxide semiconductors. The method involves microorganisms such as fungus and bacteria cultures that act as bioreduction agents. Before use, these cultures are allowed to grow in the media for a day. Thereafter, the centrifugation process and sterilization are required, with dilutions, then allowed to grow again for another day. The diluted culture is used, whereby it interacts with the metal precursor of interest

[143]. Generally, microorganism's synthesis of metal ions can either be intracellular or extracellular. To illustrate the mechanism in both paths, enzymes in the bacterial or fungi play a role in bio-reduction. These mechanisms are mostly illustrated by the reduction of Ag and Au ions to nanoparticles [144, 145]. The metal ion is added to bacteria culture. Intracellular mechanism reduction of metal ion is through the bacteria cell wall. The cell wall consists of enzymes that are able to reduce metal ions. The metal ions are positively charged while the cell wall is negatively charged. Firstly, nucleation take place through electrostatic interaction of metal ions and the bacterial cell wall. The metal ions in the medium are then attracted to the bacteria cell wall. In the process, the nanoscale metal ions diffuse in the cell wall. The reduction of metal ions to nanostructures takes place on the surface of mycelia and also on the periplasmic space as indicated in Figure 2.6 [145, 146, 147]. It also indicates the extracellular mechanism in which NADH transfer electron by NADH-dependent reductase enzyme (electron carrier) to initiate reduction of metal ions to form metal nanostructures [145, 149].

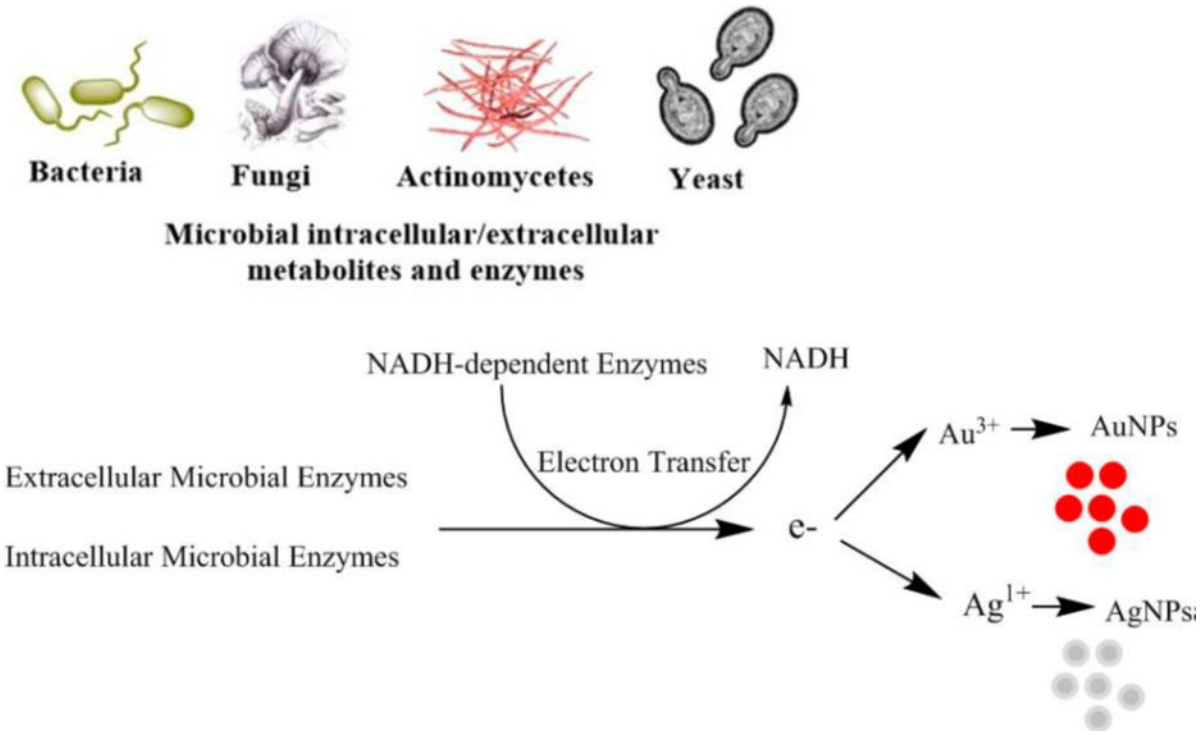

Figure 2.6: Formation of nanoparticles via Intracellular and Extracellular mechanism [8].

Bacillus amyloliquefaciens was explored in the reduction of titanyl sulfate ($TiOSO_4$) to TiO_2 nanostructures. From the mixture of titanium precursor with *Bacillus*

amyloliquefaciens, precipitates formed and were calcined to remove biomass to produce TiO_2 nanoparticles [95]. Ibrahem *et al*., [150] used *lactobacillus crispatus* for the synthesis of TiO_2 nanoparticles. The reductase enzyme in *lactobacillus crispatus* was responsible for the extracellular formation of TiO_2 nanoparticles with a 70.98 nm size. Triphati *et al*., [71] used *Bacillus licheniformis* bacteria strain which was mixed with Zinc acetate dehydrate solution for the synthesis of ZnO nanoflowers. The analysis performed confirmed the formation of ZnO nanoflowers in the presence of *Bacillus licheniformis* at room temperature. Jayasseelan *et al*., [151] used *Aeromonas hydrophilia* at room temperature to dehydrate titanyl hydroxide to give TiO_2 nanoparticles. SEM images showed a spherical shape with individual sizes of 40.50 nm of TiO_2 nanoparticles.

Table 2.4 Biosynthesis using various microorganism's strains to synthesis of CuO, TiO_2 and ZnO nanostructures.

Microorganisms	Precursor	Metal oxide	Shape	Size (nm)	References
Aeromonas hydrophilia	Zinc acetate	ZnO	Spherical, oval	57.72 (AFM)	[9]
Aeromonas hydrophilia	Dihydroxy(oxo)titanium	TiO_2	Spherical	40.50 (XRD)	[151]
Bacillus sp	Copper sulphate	CuO	Spherical	2-41 (SEM)	[152]
Aspergillus fumigatus JCT	Zinc sulphate	ZnO	Spherical	60-80 (SEM)	[153]
Bacillus licheniformis	Zinc acetate	ZnO	Nanoflowers	-	[71]
Penicillium chrysogenum	Copper nitrate	CuO	Spherical	9.7 (TEM)	[154]

Bacillus mycoides	Titanyl hydroxide	TiO_2	Spherical	40-60 (TEM)	[155]
Pseudomonas aeruginosa	Zinc nitrate	ZnO	Spherical	35-80 (TEM)	[156]
Seiratia urellytica	Zinc acetate	ZnO	Spherical	170-250 (SEM)	[157]
Bcillus subtilis	Dihydroxy(oxo) titanium	TiO_2	Spherical-oval	66-77 (SEM)	[158]
Candida albicans	Zinc oxide	ZnO	Quazi-spherical	20 (TEM)	[159]

Though the microorganisms mediated synthesis of metal oxides has been employed to synthesise metal oxide nanostructures, the method suffers from a lot of limitations. The problem is that it includes complex steps, such as isolation, culturing, maintenance and recovering of metal oxides nanostructures [160]. In addition, the metal oxide nanostructures production is slow and low.

2.3.2.2.2. Synthesis of metal oxides nanostructures using plant

Plant mediated biosynthesis has been shown as the most viable route compared to the microorganism's method. The route does not produce pathogenic species and is safe. The use of plants offers promising outcomes for the scientific field. Generally, a variety of fresh plants are collected from their geographic location. The collected plant is allowed to dry, then crushed. Afterwards, it can be extracted with solvents like water. The interaction between the metal and compounds in plant extract is not yet established, but metals differ in terms of oxidation state existence as Zn^{2+} and Ti^{4+}.In this section Zn is used as an example to describe possible formation of ZnO. As indicated in Figure 2.7, three compounds are depicted in the proposed mechanism of forming the ZnO nanostructures. The phenolic acid, flavonoid and vitamin B based phytochemicals compounds obtained from *Moringa oleifera* illustrated three possible ways of solvating the Zn^{2+} ions. A plausible mechanism is that the metal ions in the solution of the plant extract are altered by oxidation of the present biological compounds via free radicals, followed by electrostatic attraction between free radicals and metal precursors. For example, L-ascorbic acid to dehydro L-ascorbic acid via free radical, it interacts with zinc ion from zinc nitrate as shown in Figure 2.7.

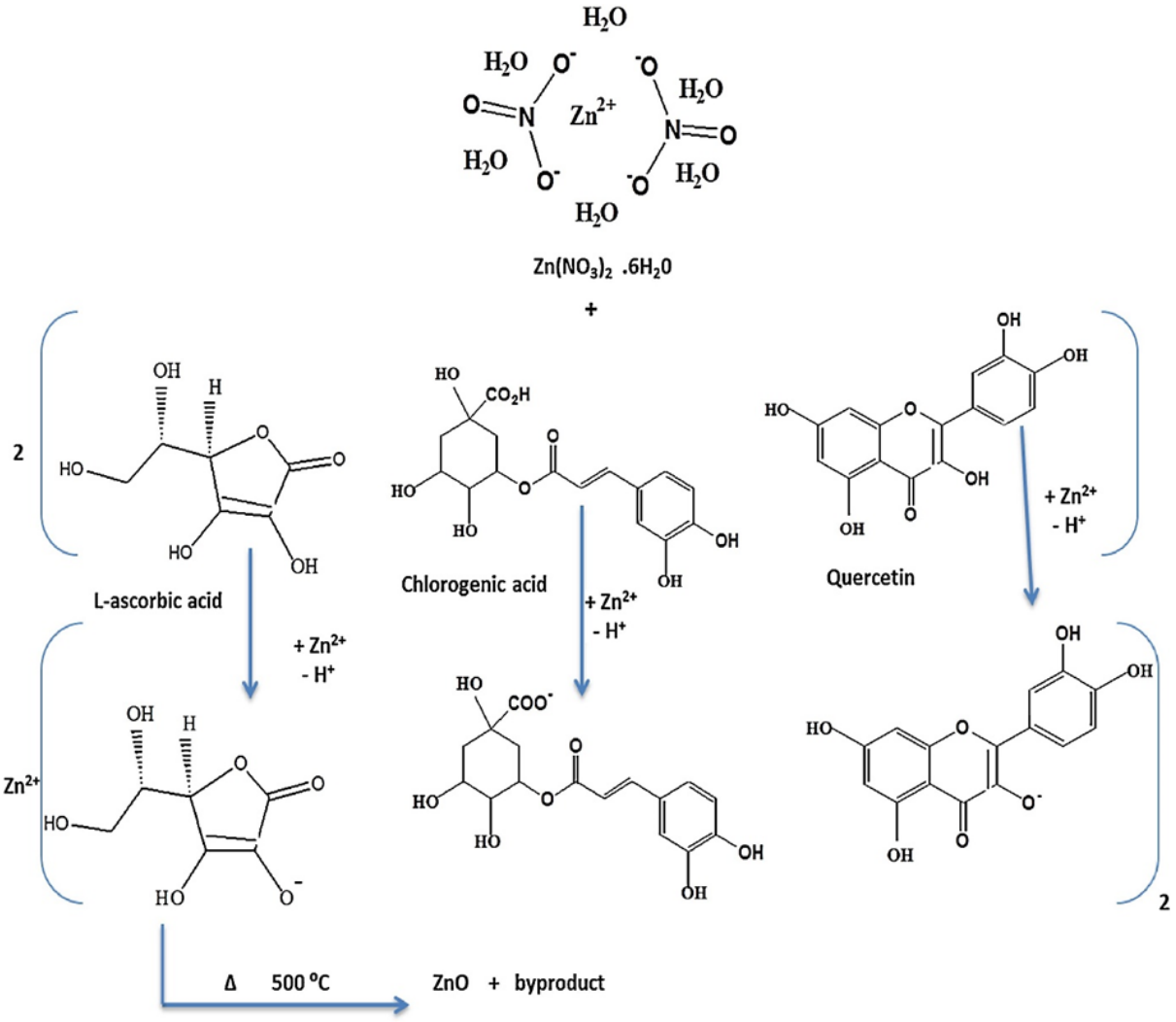

Figure 2.7: Mechanism of green synthesis of metal oxide nanostructures using plant [161].

The *Camelia sinensis* leaf extract was used to reduce cupric acetate to CuO nanoparticles. The TEM demonstrated a spherical shape morphology with a particle size range of 25-32 nm [162]. Madan *et al*., [163] used zinc nitrate and *Neem* leaves extract, varying the concentration of an extract from 2 to 20 millilitres. From the experiment, 2 millilitres gave rise to small branches like a mushroom shape. The obtained ZnO nanoparticles had a bullet shape at the 4 millilitres concentration with the size range 10-30. An increase in concentration to 6 millilitres ZnO resulted in the nanobuds shape. Nanobuds further transformed into cones and plates with an increase in plant extract. According to this study, morphology depended on the concentration of an extract as it was confirmed by SEM. In another study, zinc acetate

was used as metal precursor and *catharanthus roseus* extract as a reducing, capping and stabilizing agent. The extract was allowed to interact with zinc ions, monitored using UV-vis spectroscopy at every hour. After 3 hours, a maximum peak was observed indicating the formation of ZnO nanoparticles [164]. Ganesan *et al*., [165] synthesised TiO_2 nanoparticles using *Ageratina atissima (L)* king and HE *Robines* leaf extract. $TiO(OH_4)$ was mixed with the aqueous extract for several hours at room temperature. The spherically shaped nanoparticles were formed with average particle sizes obtained from SEM found to be in the range 60-100 nm. Stan *et.al.*, [166] used different plant extracts to synthesise ZnO nanoparticles from zinc nitrate hexahydrate. *Allium satium* (garlic), *Allium cepa* (onion) and *Petroselinum crispum* extracts were able to reduce zinc ion to ZnO nanoparticles with the average size ranges from 14-70 nm. The outcome of TiO_2 and ZnO nanostructures generally determines the applications of the materials can be used in. Procedures from literature showed that the biosynthesis of nanostructures meets the criteria in many applications [167].

Table 2.5 Some of the biosynthesised CuO, TiO_2 and ZnO nanostructures using plant extracts.

Plant type	Precursor	Metal oxide	Shape	Size (nm)	References
Jatropha curcas	Titanium tetrachloride	TiO_2	Spherical	10-20 (FESEM)	[86]
Trigonella foenum	Titanium oxy sulphate	TiO_2	Spherical	20-90 (HRSEM)	[123]
Pongamia Pinnata	Zinc nitrate	ZnO	Spherical	100 (TEM)	[168]
Prosophis fracta	Zinc nitrate	ZnO	Spherical	26 (SEM)	[169]
Asparagus racemosus	Copper nitrate	CuO	Nanorods	11-12 (XRD)	[170]
Azordirachta Indica	Titanium dioxide	TiO_2	Spherical	15-45 (TEM)	[171]
Solanum nigrum	Zinc nitrate	ZnO	Quasi- spherical	29.79	[172]

				(TEM)	
Alianthus altissima	Copper acetate	CuO	Spherical	20 (TEM)	[173]
Cicer arietinum	Titanium tetrachloride	TiO_2	Spherical	14 (TEM)	[174]
Vigna unguiculate	Titanium dioxide	TiO_2	Oval	-	[175]
Psidium guajava	Dihydroxy(oxo)titanium	TiO_2	Spherical	32.58 (XRD)	[176]
Ceropegia candelabrum	Zinc nitrate	ZnO	-	12–35 (XRD)	[177]
Ulva fasciata	Zinc chloride	ZnO	Rods	70 (SEM)	[178]
Stevia	Zinc acetate	ZnO	Rectangular	10–90 (TEM)	[179]
Pterolobium hexapetalum	Copper sulphate	CuO	Spherical	10-50 (TEM)	[180]

Monsonia burkeana	Zinc chloride	ZnO	Semi spherical	<20 (TEM)	[181]
Bauhinia Tomentosa	Zinc sulfate	ZnO	-	22–94 (TEM)	[182]
Sutherlandia frutescens	Zinc nitrate	ZnO	Spherical	5–25 (TEM)	[183]
Alchornea cardifolia	Copper sulphate Zinc acetate	CuO ZnO	Nanosphere and nanoblocks Spherical	16.25 75.22	[184]

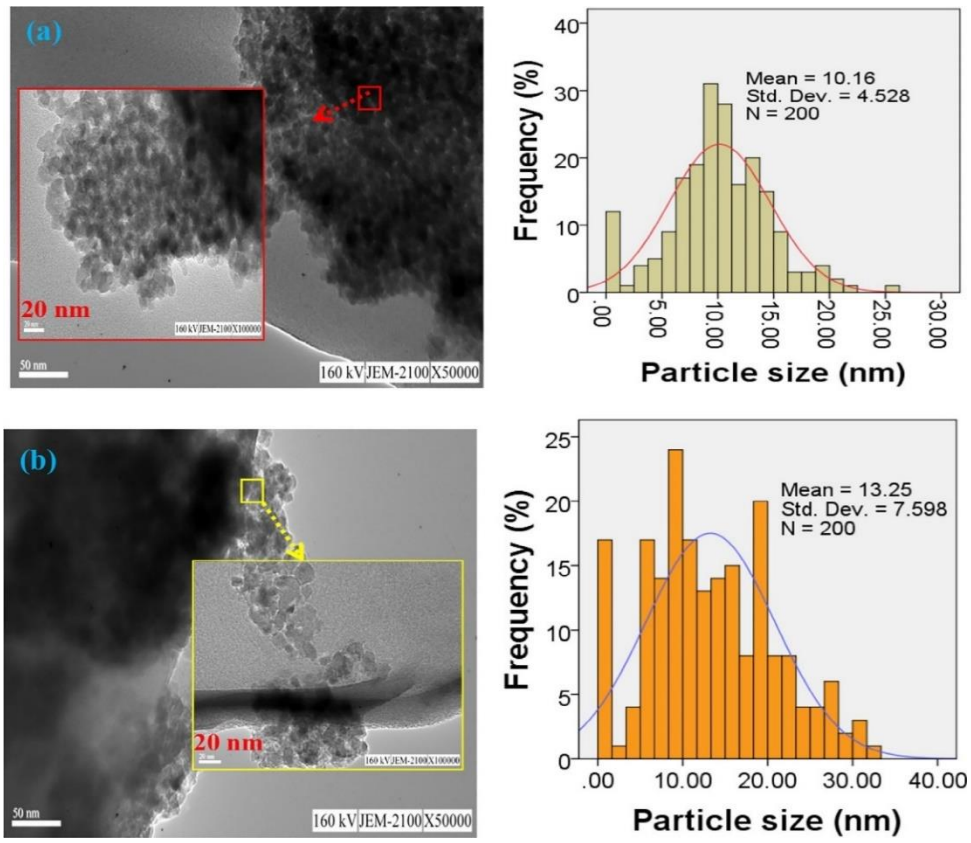

Figure 2.8: TEM images of the as-synthesised TiO_2 samples; TiO_2 synthesised with *Thyme Alcea* (a) *Alcea* (b), accompanied by their respective particle size distribution histograms [30].

2.4. Classification of Zinc oxide and Titanium dioxide nanostructures

The planet is full of mineralised inorganic materials. Since their deposition discovery, they have been intercepted in the world of nanotechnology. It is the world of technology that is capable of producing 1-100 nm materials such as ZnO and TiO_2 nanostructures. ZnO and TiO_2 nanostructures nowadays are technologically very important materials in many applications. This is due to their intrinsic properties investigated by the science community. Their properties include composition, structure, phases, crystallinity, morphology, size and optical, which now assists in their classification.

2.4.1. Zinc oxide (ZnO) nanostructures

ZnO is an n-type inorganic metal oxide semiconductor with a high binding energy of 60 meV [185]. It is also reported to have a wide band of 3.87 eV and 3.32 eV calculated

from tauc plot [186, 187]. In addition, it is a member of the group II-IV semiconductor family and with a covalence that lies between ionic and covalent semiconductors [188]. This material exhibits hexagonal wurtzite structure with closely parked sub lattices. Each of these lattices consists of one type of atoms displaced with respect to each other along the threshold C-axis [189]. These nanostructures can be in three dimensional structures namely, zero dimensional (0D), one dimensional (1D), two dimensional (2D) and three dimensional (3D) as shown in Figure 2.9. The dimension of nanostructures is related to the morphology with 1D denoted to nanowires, 2D and 3D belonging to either nanosheets, nanoflowers, nanoplates and nanoparticles [145, 190, 191, 192, 193, 194, 195]. These morphologies are utilized for various applications due to their properties which determines their performance in certain applications. The 3D nanoflowers are promising in the field of solar cells and gas sensors due to their large surface to volume ratio. Nanorods and nanoparticles are generally competing for photocatalysis applications. Nanorods have been observed to have a lower crystallinity and defects on the surface which may be due to hydroxyl groups bonding on the defects. Performance of photocatalyst generally depends on the specific surface area and the density of hydroxyl groups. Nanoparticles are easily suspended in a solution which increases the rate of interaction with contaminants. Furthermore, nanoparticles have a high surface area which enables them to adsorb more contaminants and makes them one of the best choices in photocatalysis [196].

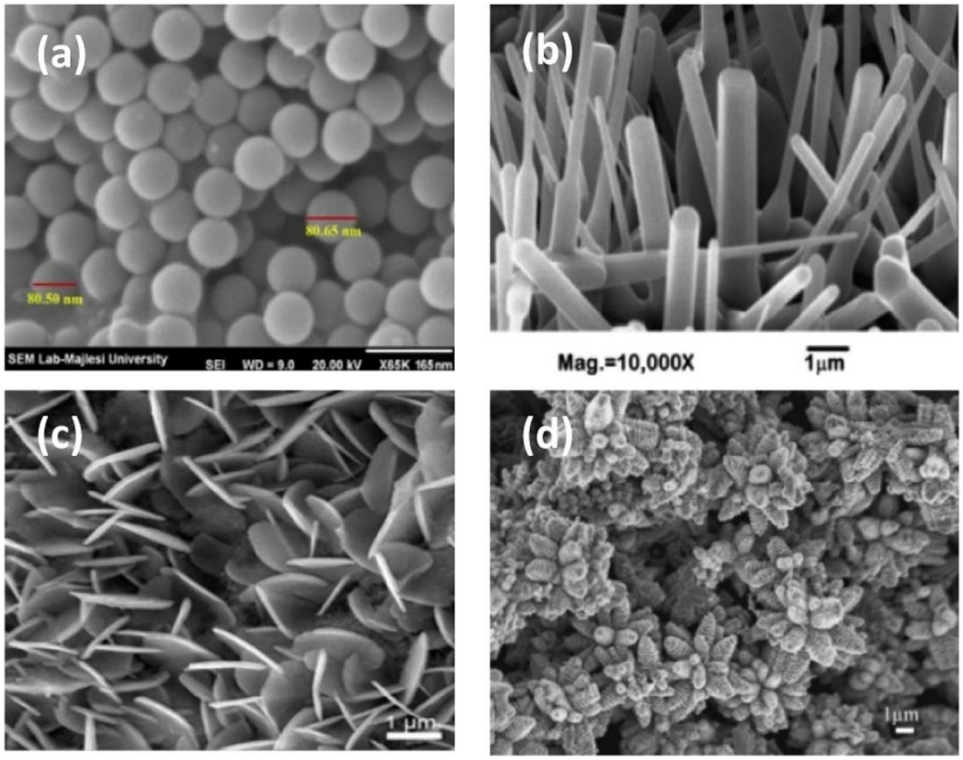

Figure 2.9: FESEM and SEM images for (a) 0D, (b) 1D, (c) 2D and (d) 3D Zinc oxides [145, 194, 195].

2.4.2. Titanium dioxide nanostructures

Titanium dioxide is a transition metal semiconductor material that has superior properties such as low toxicity, high stability and redox potential [197]. Due to these properties, this material has been applied in various technologies such as sensors, solar cells and environmental remediation. TiO_2 exists naturally in various polymorphs of rutile, anatase and brookite. The metastable anatase and brookite phases can irreversibly convert to stable rutile upon heating (>600 ^oC) [198]. The rutile and anatase phases are the most common polymorphs. They share similar physical and chemical properties but with slight differences in existence. In terms of band gap, both are around 3.2 eV and 3.00 eV respectively [199]. Anatase can be differentiated from rutile by the diffraction pattern. The anatase formation is confirmed by miller index (101) at around 25^o, while rutile is perceived at 27^o and is associated with crystallographic plane (110). Both phases exhibit a different behaviour in catalysis reactions particularly photocatalysis [200, 201, 202]. The most significant difference is the dissociation of adsorbed molecules on the surface. Rutile dissociates the adsorbed molecules easier than the anatase phase [203]. Figure 2.10. represents the

crystallographic structure of rutile and anatase phase. The polymorphs are commonly represented by distorted TiO_2 octahedron building blocks in the crystal structures. Rutile crystallographic structure is made up of corners which share the TiO_6 octahedra in a tetragonal cell whilst the anatase structure consists of edge shared TiO_2 in a tetragonal cell. In structure, the O_h symmetry of ideal octahedron is reduced to D_{2h} symmetry due to different in plane and out of plane Ti-O bond lengths and two other types of Ti-Ti in plane bond angles deviating from 90°. In anatase, there is an additional displacement of the oxygen ions from the in plane positioning, generating a local D_{2h} symmetry. When D_{2h} symmetry experiences a stronger distortion in brookite, it affects the bond lengths and bond angles, leading them to slightly differ from each other. This results into loss of local symmetry and C_1 symmetric TiO_6 units [204, 205]. However, with all the description of the common polymorphs, anatase is shown to be the most efficient photocatalyst. Anatase phase has superior properties such as high stability and redox properties. The TiO_2 phases of interest are determined by the temperature applied to the nanostructures during synthesis.

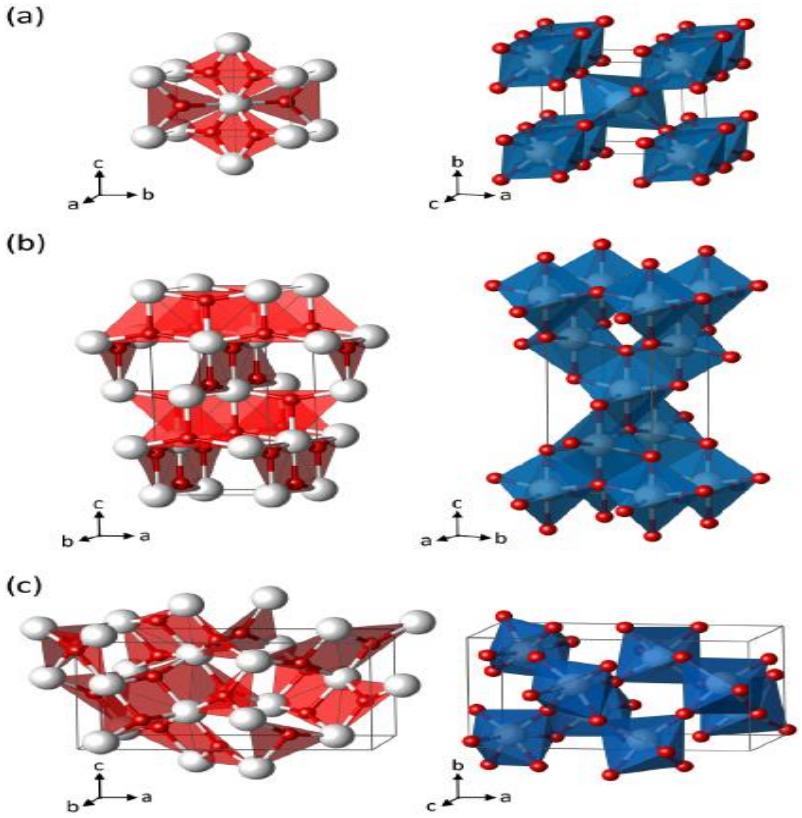

Figure 2.10: Crystallographic structures of (a) rutile, (b) anatase and (c) brookite with white representing Ti and red O. Planar Ti_3O building block representation (left) and TiO_6 polyhedra (right) [201].

This section provided some properties of nanostructures that makes them alternatives materials in many fields. For example, in section 2.1.1, TiO_2 and ZnO nanostructures were shown to be good photocatalysts for treatment of organic dyes in water. However, these nanostructures are more activated by UV irradiation rather than visible light. Thus, studies have developed strategies of modifying the nanostructures.

2.5 Modification of ZnO and TiO_2 nanostructures

The modification strategies pave a way in manipulating the materials properties such as band gap and surface area by combining the materials. The materials combination can be either materials with a lower band gap or materials with larger surface area.

2.5.1. Coupling of semiconductors with other semiconductors

ZnO and TiO_2 are known to exhibit excellent properties [206, 207]. Moreover, TiO_2 and ZnO nanostructures have emerged as promising candidates in photocatalysis for the degradation of organic dyes due to their unique characteristics such as redox property, band gap at UV spectral region and photocatalytic property [208]. However, they have a wide band gap activated by the ultraviolet region [209]. Combining ZnO and TiO_2 with lower band gap semiconductors can improve the activation to be within the visible light region. Semiconductor materials including CuO, Fe_2O_3 and SnO_2 have been coupled with ZnO or TiO_2 nanostructures [34, 210, 211]. Making new photocatalyst by coupling with other semiconductor is an important development. The excitation/transfer of electron within binary system is important in photocatalysts. Despite both having good photocatalytic properties, coupling nanostructures surpasses the photocatalytic activity of bare nanostructures. Coupling of semiconductors also involves a combination two semiconductors which can either be p-type and n-type or the same semiconductor [27, 212]. Already, coupling has been proven to eliminate the drawbacks of semiconductors. James *et al*., [212] synthesised SnO_2/TiO_2 to study the transfer of electrons from the core/shell to the other. According to the study, only one electron state was populated within SnO_2/TiO_2 films. The electrons were injected into TiO_2 in this composite due to SnO_2 having the most positive conduction band edge. Gnanasekaran *et al*., [213] prepared TiO_2@Fe_3O_4 photocatalyst that exhibited absorption in the visible region with 2.70 eV band gap. Further analysis was conducted, whereby PL revealed that Fe_3O_4 delayed the

electron-hole recombination process. The nanocomposite showed that it is efficient against colourless and colourful organic pollutants (MO, MB and Phenol). In another study, CuO was loaded on TiO_2 using sol-gel and dip-coating methods. The composite degraded more than 90% of MB using visible light at 430 nm illumination after 4 hours [214]. Luna *et al*., [215] coupled TiO_2 with narrow band gap CuO as a strategy to obtain visible light active photocatalyst. From literature, it is known that TiO_2 (P25) has a band gap of 3.10 eV. However, it was reduced with an increase in the content of CuO as Tabulated in Table 2.6:

Table 2.6 Band gap variation with CuO loading on TiO_2 [215].

Samples	**Band gap (eV)**
TiO_2	3.10
3 CuO-TiO_2	2.56
5 CuO-TiO_2	2.50
10 CuO-TiO_2	2.46
20 CuO-TiO_2	2.40
40 CuO-TiO_2	2.31
70 CuO-TiO_2	2.06

In another study, a similar strategy was used, in which 2, 4, 6 and 8 % of Ag was incorporated on TiO_2 mediated by *Azadirachta insica* leaves extract. The obtained results were 65, 84, 87 and 78 % of MB decolourisation after 120 minutes in 2, 4, 6 and 8 % loadings respectively. The optimum was found to be 6% loading of Ag. Authors suggested that a higher content of Ag overshadowed the active centre of TiO_2 and led to a decrease in photocatalytic degradation [216]. The photocatalytic properties of the CuO/ZnO were compared with the bare ZnO. The doped ZnO showed a higher photodegradation activity towards MB dye [217]. Bharathi *et al*., [218] employed 1, 3, 5, 10, and 15 % loading of CuO on ZnO to degrade MB under visible

irradiation. Photocatalytic degradation increased from 1 to 5 % loading and then decreased between 10 and 15 % loading. The results follow the same trend with Saeed *et al*., [215] as results are Tabulated in Table 2.7:

Table 2.7 Variation in loading of CuO with respect to photocatalytic degradation [218].

% CuO/ZnO	% Degradation	% CuO-TiO_2	% Degradation
1	91.44	2	65
3	93.05	4	84
5	96.56	6	87
10	93,19	8	78
15	93.18	-	-

It has been observed that coupling does reduce the recombination rate of electron-hole pair and increases the lifetime of the charge carriers. Normally, the material with a lager band gap is coupled with a lower band gap for improvement of charge separation. Based on the same principle more alternative materials with high surface area such as clay, zeolites, silica and carbon based materials address the drawbacks. These materials have been successfully used in the adsorption of dyes holding up to the advantage of synergic affect [219]. However, carbon based materials have been of interest as a support to ZnO and TiO_2 nanostructures due to their high surface area and strong affinity towards organic pollutants.

2.5.2. Coupling of semiconductors with carbon based materials

Carbon based nanomaterials have excellent properties, which have led to multiple applications. In water purification, they act as an adsorbent or a supporting material for semiconductor metal oxides. Carbon based materials can effectively be used as supporting material to make heterojunction photocatalysts with metal oxides nanostructures. Heterojunction photocatalysts combine different merits including charge separation, reducing electron-hole pair recombination and light adsorption

[219]. Natarajan *et al*, [220] synthesised MWCNT/TNT composite to enhance decomposition of RhB-6G under UV light. Photoluminescence analysis indicated that the decomposition of RhG-6G was enhanced by the ability of MWCNT to promote electron transfer process and reduce the electron-hole recombination rate. A facile one step hydrothermal method was used to synthesise a carbon quantum dots/TiO_2 based composite. Carbon quantum dots are known to have photocatalytic properties, as they can enhance the degradation of dyes by enriching light absorption and reducing the electron-hole recombination rate. In that experiment, carbon quantum dots were used to serve that purpose [221]. Tie *et al*, [222] studied the in-situ synthesised ZnO and carbon nanotubes (ZnCT) hybrid. The composite was then utilised as a photocatalyst for the decomposition of RhB dye. Their synthesis provided covalent bonding between ZnO and functionalised CNTs, leading to the extension of the light adsorption and creating an efficient pathway for acceleration of the electron transfer. Furthermore, reduced recombination rate of electron-hole pair and extended lifetime of electron-hole pair of ZnO NRs was confirmed by Thermoplastic Vulcanizate (TPV) and photocurrent measurements. The supported ZnO NRs (90%) showed a higher photocatalytic activity than a bare ZnO NRs (74%) under sunlight irradiation. In another study, carbon nanospheres were synthesised using the pyrolysis method from benzene at 1000 ^oC. Preparing the composite, ZnO was doped on the surface of CNSs using the facile chemical precipitation method. According to the study, ZnO/CNSs showed a higher photocatalytic degradation of 85.6% after 25 minutes of UV irradiation [223].

2.6. Carbon based materials

Carbon is one of the key elements found in the earth crust. Its relative abundance is estimated to be between 180 and 270 parts per million (ppm) [224]. Over the years, various forms of carbon have contributed to the livelihood of humans and technology. The catenation property of carbon created its way to chemistry and biology [225]. Naturally, carbon exists in two crystalline allotropic forms known as diamond and graphite [226, 227]. However, after the breakthrough of fullerene (Buckminsterfullerene) [228], the synthesis of carbon based materials expanded. The variety of forms of carbon identified are carbon nanotubes [229, 230], graphene [231], carbon nanospheres [232], carbon dots [233], carbon onions [234] and carbon nanofibers [229, 235]. The materials mentioned are grown by the diffusion of a carbon

substance through a metal catalyst. The outcome of the shape and size of carbon-based nanomaterials are channelled by the synthesis conditions [236, 237].

2.6.1. Carbon nanotubes

Ijima rediscovered carbon nanotubes in 1991 [3], since then, they brought revolutionary change into many fields. During the rediscovery, the arc-discharge method was one of the first methods used for studying the surface of graphite electrode. More methods are now employed to synthesise CNTs including laser ablation and chemical vapour deposition. CNTs show unique properties such as mechanical, electrical and thermal properties [238]. However, this material is a cylindrical form of graphene sheets. The CNTs are categorised into two, as multiple walled carbon nanotubes and single walled carbon nanotubes. Multi walled CNTs, can be regarded as coextensive stacked layers of graphene into rolled cylindrical form and single walled CNTs, can have single graphene layer in a cylindrical form [239] as indicated in Figure 2.14.

2.6.2. Carbon spheres

The discovery of CNTs brought the development of other carbon based materials such as carbon spheres. The carbon nanospheres have been used for drug delivery [240], energy storage [241] and adsorption [240, 242]. Owing to their attractive properties such as low density, cavity volume, high shell permeability and chemical stability [243]. Carbon spheres are formed by pairing pentagonal and heptagonal rings of circular graphitic layers. Carbon spheres are classified into two, hollow and solid spheres. Solid and hollow carbon spheres are usually synthesised by chemical vapour deposition (CVD) and the hydrothermal method [244, 245]. During CVD, gases and natural products are used as carbon sources [195, 196]. In the Figures (2.11, 2.12), the synthesis of hollow carbon spheres and TEM images are depicted. The phenol formaldehyde resins spheres were carbonized at 500 °C for 4 hours under nitrogen gas and solid carbon spheres were formed. It was further etched by thermal oxidation to form varying pore sizes of hollow carbon spheres at different times. The hallowing of solid spheres increased with the etching time in the interior of a sphere.

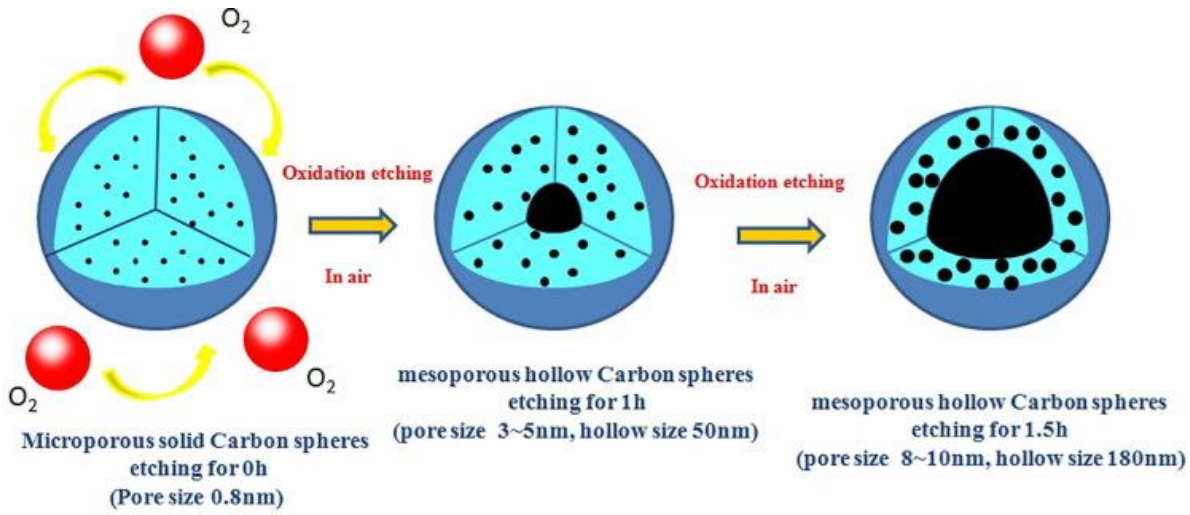

Figure 2.11: Mesoporous solid carbon spheres and illustration of the synthesis of the mesoporous hollow carbon spheres [246].

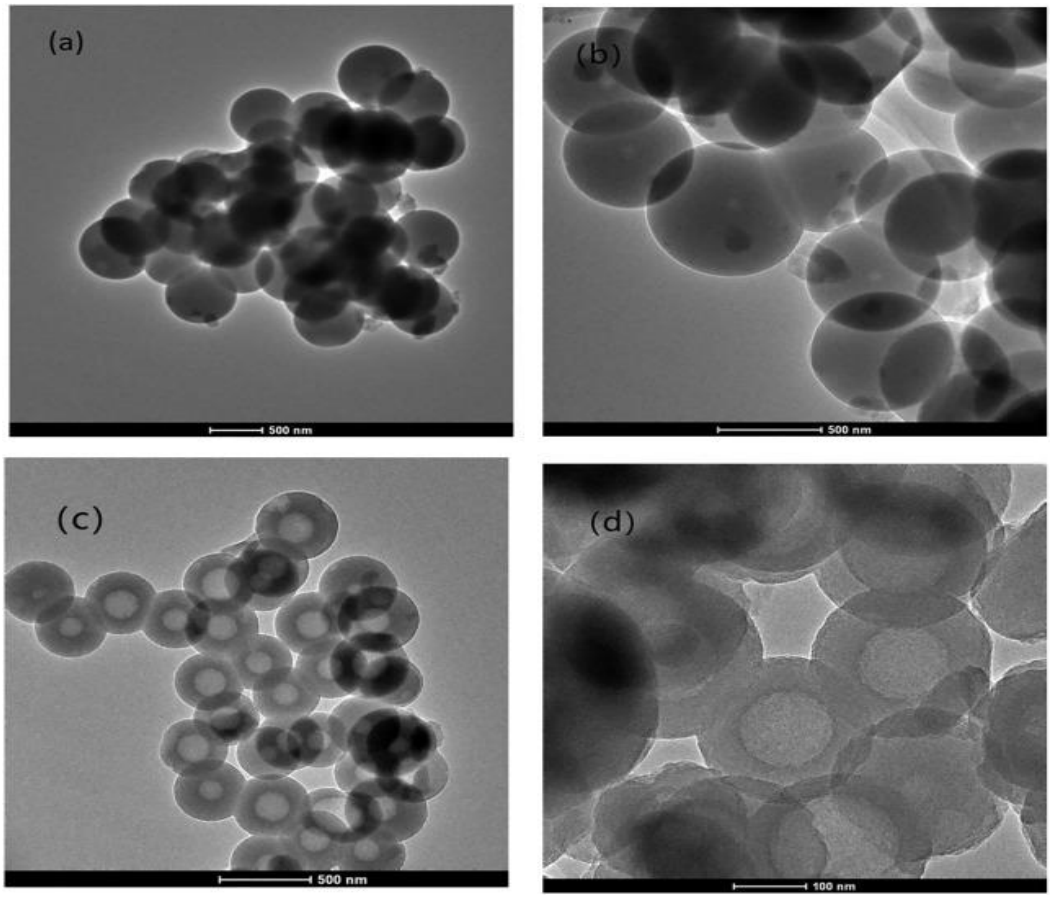

Figure 2.12: TEM images of mesoporous hollow carbon spheres etched at different times [246].

2.6.3. Carbon nanofibers

According to the reviews, CNTs and CNFs are similar but differ in the arrangement of graphite sheets [247, 248, 249, 250]. Possibly, the carbon layers can be used to differentiate the CNTs and CNFs. In the case of CNTs, graphene layers are rolled up into hollow cylindricals to form parallel to the fiber axis. The growth pattern of CNFs is termed as herringbone, cup-stacked, ribbon and platelet relative to graphene layers. In these structures, graphene layers are either packed at an angle or perpendicular with respect to the fiber [248, 250, 251]. In ribbon graphene, the layers are parallel to the growth axis [168]. As for the platelet the layers of graphene are perpendicular to the growth of the fibers [250, 252].

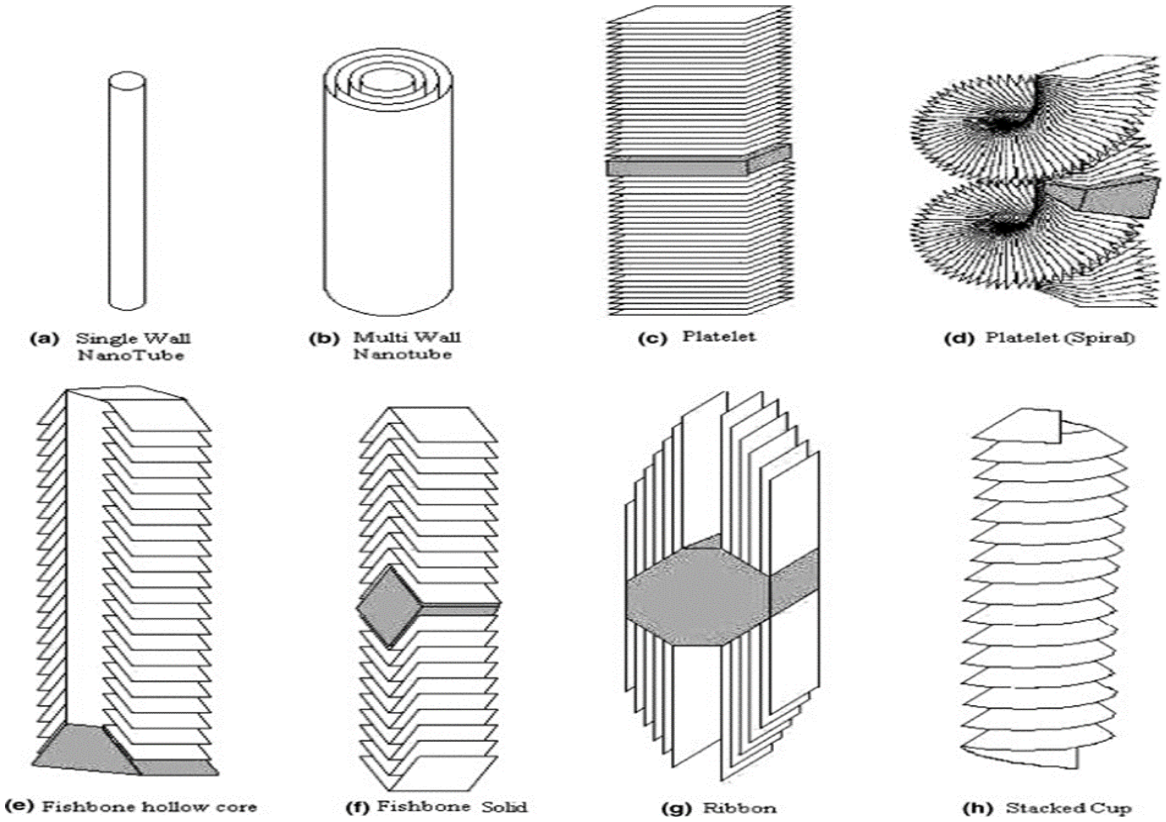

Figure 2. 13: Different structures of CNTs and CNFs [252]

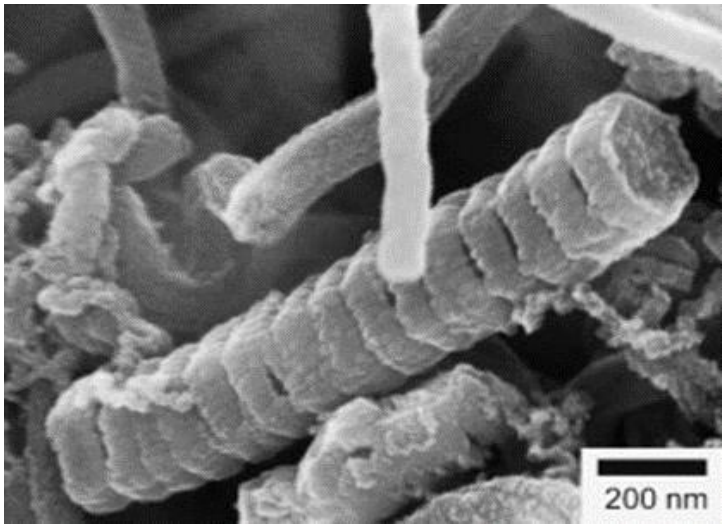

Figure 2.14: Typical image of platelet under SEM [252].

The CNF structures are generally synthesised using the chemical vapour deposition (CVD) and electron spun methods [253, 254]. However, the electrospinning method requires many steps such as spinning and carbonisation, thus CVD is the most preffered method. The principle of the method is that there is a decomposition of hydrocarbons supported by the catalyst. The method uses catalysts such as Ni, Co, Fe, coal fly ash [255, 256, 257, 258] and other waste materials. The metals chosen to synthesise CNFs are capable of forming metal carbide [259]. Nonetheless, the metal catalysts are regarded expensive, thus researchers have moved more towards the use of waste materials such as coal fly ash as a catalyst. Coal fly ash is a by-product produced when generating electricity with coal. Metals that are normally used as catalysts are part of the composition of coal fly ash. As the constituents, they are responsible for the growth of CNFs. Other components of coal fly ash are SiO_2 and Al_2O_3, with little traces of CaO, BaO and Mn [260]. The use of fly ash assists in the reduction of cost associated with the disposal of the material. Several studies have shown that coal fly ash can act as a catalyst to grow carbon nanofibers [258, 260, 261, 262]. The growth of CNFs structures involves two modes, tip growth and base growth. The mechanisms depend on the catalyst nano-size metal particles that are used to grow CNFs and also the catalyst-subtrate interaction [247]. The tip growth takes place due to the weak interaction between catalyst and substrate. In this mechanism the catalyst particles are pushed up from the substrate and are carried at the tips. In the base growth mechanism, the catalyst particles adhere strongly to the substrate surface and remain pinned during the growth process. The evidence for the growth

mechanisms is provided by the techniques employed to show the features of the material.

2.7. Characterisation techniques

In achieving the objectives of the study, characterisation plays a major role. After the synthesis of each of the materials, characterisation takes place to study thephysical and chemical properties of the formed materials.

2.7.1. Liquid chromatography-mass spectrometry (LC-MS)

LC-MS is an analytical technique that couples the features of liquid chromatography and mass spectrometer, used to explore the organic constituents in a sample. In this study, it identifies constituents that are present in the plant water extract. LC separates the components in a sample using a mobile phase and stationary phase. MS identifies the components by separating the charged compounds using their mass to charge ratio (m/z) [263, 264, 265].

2.7.2. UV-Vis spectroscopy

UV-Vis spectroscopy is a technique that is utilised to determine the optical properties of nanosized materials and monitoring of the degradation rate by measuring the concentration of the organic contaminants. In general, to determine the optical properties, the scan of 200 to 800 nm is used. These spectra consist of two regions, ultraviolet region ranging from 10 nm to 400 nm and the visible region ranging from 380 nm to 780 nm. In a study by Pugazhenthiran *et al*. [153], f the exciton peak of ZnO nanoparticles was found to be within ultraviolet region 375-380. Maximum wavelength of malachite dye was expected at around 617 nm [266] and methylene blue at 660 nm [267]. Knowing the exciton peak wavelength of a substance, the concentration of dye molecule is determined using the calibration curve of that dye molecule. The UV-Vis output is based on the Beers lambert law which states that absorbance of a solution is directly proportional to the concentration of the solution.

2.7.3. Fourier transform infrared spectroscopy (FT-IR)

FT-IR is an instrument that is used for qualitative analysis for the binding of functional groups. In material science, it is used to confirm binding of functional groups to the surface. In green chemistry, it can be used for confirmation of functional groups responsible for reduction of the metal salt. During the analysis, most of the functional

groups appear within the range 400-4000 cm^{-1}. For example, Sharmila *et al*., [123] analysed *Tecoma castanifolia* mediated ZnO nanoparticles using FTIR where groups attached to the surface were identified according to their stretching vibration mode. Some of the functional groups were identified as follows C—H at 2930, O—H at 3291 C—O at 1239 and Zn-O represented at 459 cm^{-1}.

2.7.4. X-ray powder diffraction (XRD)

X-ray powder diffraction is employed to determine the crystalline phase and average crystalline size. It also provides information about the unit cell dimensions, crystal structures and atomic space. The diffraction patterns of materials vary from one to another. JCPD data is normally used to confirm the patterns of certain materials if it corresponds with the standard data. For example, nanomaterials studied in this project can be identified by comparing with literature and the JCPD data. Formation of ZnO for example, can be confirmed by the planes corresponding to 2θ degrees that are similar to wurtzite structure.

2.7.5. Scanning Electron Microscopy (SEM) and Energy Dispersive X-Ray Spectroscopy (EDS)

SEM and EDS are instruments that are used to study the surface topography and composition of the materials. The mentioned techniques are interlinked together. SEM gives the output in an image format at different magnifications. The image is produced when the electrons interact with the sample in the beam to create many signals that project the obtained information from the sample on the cathode-ray tube screen [268]. Samples are normally coated with gold to protect the sensitive and ensure sufficient electrical conductivity for well displayed images. Some of the morphologies include nanobelts, nanofibers, nanoparticles, nanoflowers, nanotubes and nanorods [67, 270, 230, 235, 135, 137, 134]. The topographic surface of the material is known to depend on the precursor reagents and the method used to prepare the desired material. Qi *et al*., [269] used the hydrothermal method assisted by glass sheets to grow TiO_2 nanorods from the mixture of HCl, H_2O and $TiCl_4$, it was then heated at 450 ^oC in muffle furnace for 1 hour to form the products. In another study, Madan *et al*., [163] synthesised bullets, nanobuds, hexagonal shaped flakes in the form of cones, hexagonal nanoplates and closed pines which were cornfirmed by SEM images.

2.7.6. Transmission Electron Microscopy (TEM) and Selected Area Electron Diffraction (SAED)

TEM and SAED are employed to determine the morphology, crystallinity and average particle size of the materials. The mentioned techniques are interlinkedas TEM analyses the surface of a material at a nanometre scale and calculation of the particle size of the materials as shown in Figure 2.8. The size of the material plays an important role in their performance for each application it is intended to be used for. Synthesis conditions such as temperature and time can be one of the factors contributing to size and morphology.

2.7.7. Thermogravimetric analysis (TGA)

TGA is used to determine the thermal stability of the synthesised materials. Furthermore, it can assist in monitoring the overall purity of the materials. The technique uses the amount of weight loss in the sample as a function of temperature. The maxima temperature decomposition of the materials is estimated from the plot of the TGA curve. Depending on the constituents in the sample or the synthesis temperature, TGA spectra can show different phases relative to temperature change. In carbon based materials studies, TGA curve can be used to monitor the decomposition of the catalyst or thermal stability of the carbon nanomaterial or polyaromatic hydrocarbons from the carbon source [245, 262].

2.8. Conclusion

Up to now, contaminants in wastewater are a concern worldwide. Thus, they are widely studied in an attempt to remove them. Metal oxide nanostructures are promising materials that have been used to remove organic dyes and bacterial contaminants. However, more studies are conducted in an attempt to provide materials that are eco-friendly and synthesised with an expansion to apply them as antibacterial agents and photocatalysts. To date, green routes are effective in producing metal oxides nanostructures that provide an alternative solution to managing the concerns of water pollution. They are biosafe photo-oxidising species that impact dyes degradation and can inhibit microorganism's species. In terms of photocatalytic degradation of dyes, studies were done on supporting metal oxides such as TiO_2 and ZnO to improve their photocatalytic activity. This section showed that other semiconductors as well as carbon based materials can be used to improve the photocatalytic activity of the traditional semiconductors.

Chapter 3

Experimental and characterisation

3. Introduction

This chapter outlines the information on the synthesis of materials and description of characterisation techniques involved in the study. It describes qualitative analysis of *Monsonia burkeana (MB)* and green synthesis of metal oxides using *Monsonia burkeana*, synthesis of carbon nanofibers, carbon spheres and composites of metal oxides with carbon based materials. Lastly, treatment of bacteria with metal oxides and degradation of methylene blue is highlighted.

3.1. Materials

Zinc chloride ($ZnCl_2$), Titanium (IV) fluoride (TiF_4), copper nitrate hexahydrate ($Cu(NO_3)_2$ $6H_2O$), ethanol, sodium hydroxide (NaOH) were of analytical grade and purchased from Sigma Aldrich, RSA. *Monsonia burkeana* plant (121632) was collected from the University of Limpopo experimental farm, Turfloop. Coal fly ash was collected from Duhva power station. Bacterial strains, *Staphylococcus aureus*, *Pseudomonas aeruginosa, Enterococcus faecalis* and *Escherichia coli* were obtained from the Biochemistry, Microbiology and Biotechnology (BMBT) department at the University of Limpopo.

3.2. Preparation of *Monsonia burkeana* plant extracts

The *Monsonia burkeana* plant was collected, washed with distilled H_2O, dried for several days and crushed into a powder using a coffee grinder SCG-250 (China, Sunbeam). An amount of 10 g of cleaned and room temperature dried *MB* extract was immersed in 500 mL of boiled deionized water for about an hour at 80 °C. The mixture was cooled to room temperature while swirled by an orbital platform shaker (Lenton furnaces, 261) and filtered using a 0.45 µm Whatman membrane filters. The filtered extract was stored in the refrigerator at 4 °C for further use.

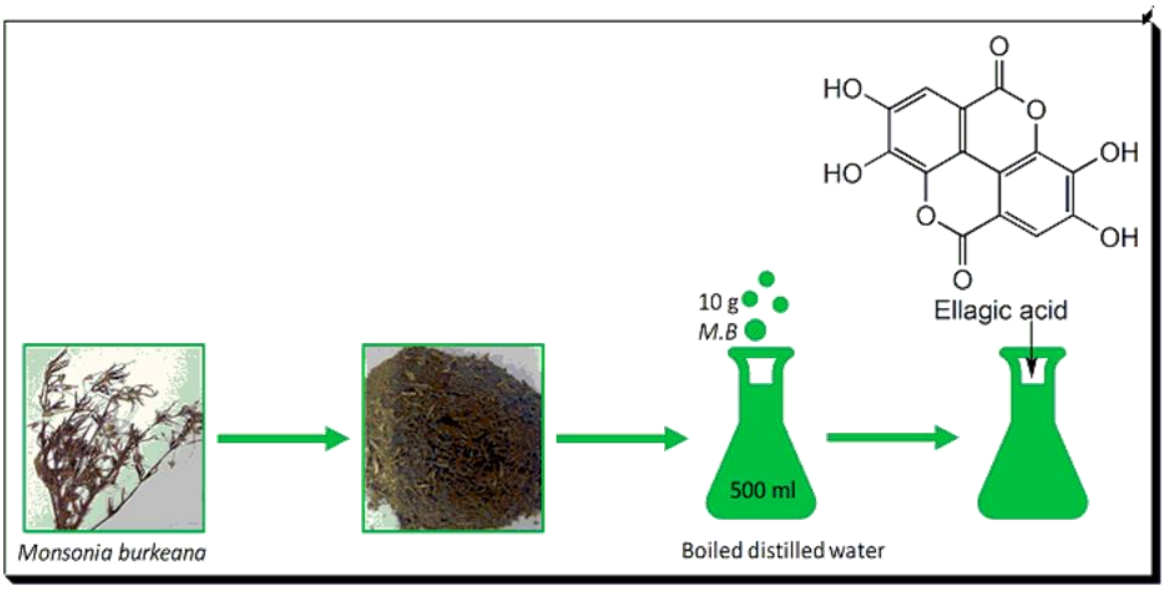

Figure 3.1: *Monsonia burkeana* plant extraction.

3.3. Preparation of ZnO nanoparticles using *Monsonia burkeana* extract

$ZnCl_2$ (3.4 g) salt was dissolved in 50 mL of *MB* plant extract and the mixture was heated for an hour. A thick dark brown coloured precipitate was formed, which indicates the formation of nanoparticles. The precipitates were poured onto the crucible and heated at 100 °C in an oven (Ecothem, labotec, SA) until the sample had dried and a powder was formed. Thereafter, the powder was washed several times with deionized water to remove any residue of the extract. The obtained powder was calcined in a muffle furnace (Snol, 8.21100LHM01 oven) at 700 °C for an hour.

3.4. Preparation of TiO_2 nanoparticles using *Monsonia burkeana* extract

Approximately, 3.4 g of TiF_4 was dissolved in 50 mL of *MB* plant extract and the mixture was heated for an hour. The precipitates were formed, which indicated the formation of TiO_2 nanoparticles. The precipitates were filtered, washed with distilled water and dried in an oven at 100 °C for a few hours. The filtered precipitates were calcined in a muffle furnace at 500 °C for an hour to form TiO_2 nanoparticles.

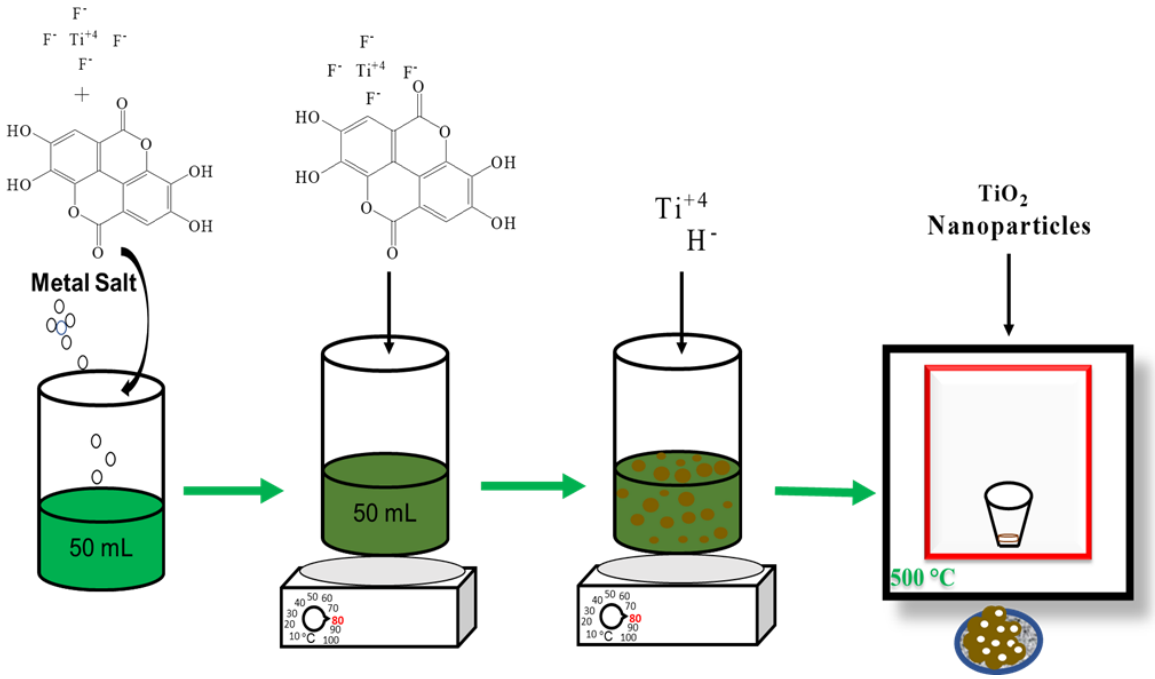

Figure 3.2: Synthesise of nanoparticles using *MB* plant extract.

3.5. Preparation of carbon nanofibers

Waste coal fly ash was obtained from the Electricity Supply Commission of South Africa (ESKOM) Duvha power station and was used as received. Carbon deposition was achieved by the chemical vapour decomposition of acetylene over the waste coal fly ash. In this reaction, coal fly ash was the catalyst, acetylene the carbon source and hydrogen were the carrier gas. In the synthesis run, 500 mg of as-received fly ash was uniformly spread in a small quartz boat and placed at the centre of a horizontal furnace. The fly ash was then heated at 10 ^{o}C/min in H_2 at 100 mL/min to 650 °C, where upon acetylene gas was introduced into the reaction zone at 100 mL/min for 45 min. After 45 min of reaction time, the flow of acetylene was terminated, and the reactor was cooled under H_2 to ambient temperature. The carbonated material was collected and functionalised using nitric acid (HNO_3) (55%) for 2 hours at 54 °C [269]. Thereafter, the CNFs were washed with distilled water until they reached a pH between 5-7.

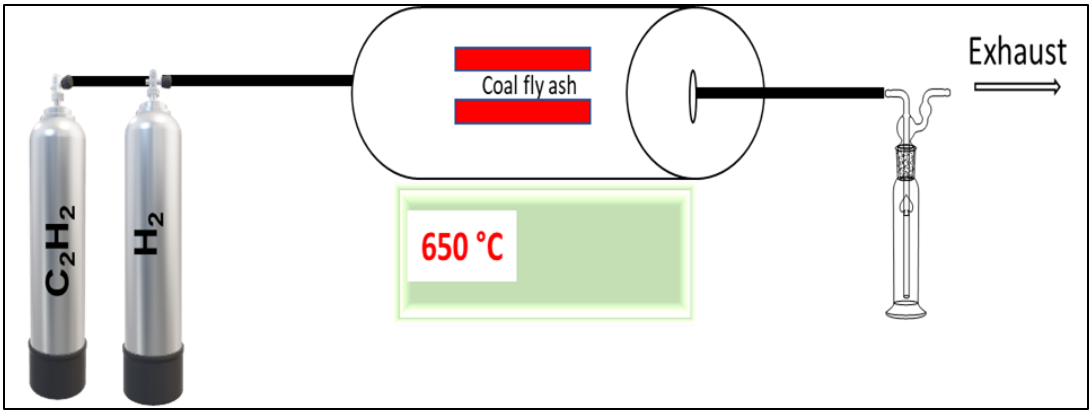

Figure 3.3: Horizontal chemical vapour deposition for synthesise of carbon nanofibers.

3.6. Preparation of carbon spheres

Carbon spheres were prepared using the vertically aligned tubular quartz tube. Acetylene was used as the carbon source and argon as the carrier gas. In this reaction, the reactor was heated to 900 °C. Then acetylene, was introduced into the system at 300 mL/min^{-1} for 45 min and argon at 200 mL/min^{-1}. After the reaction time, the acetylene was terminated, and the reactor was allowed to cool to room temperature in the presence of argon [245]. The carbonaceous material was collected using a round bottom flask. The collected carbonaceous materials were purified by Soxhlet extraction to remove aromatic components and dried overnight at 90 °C. They were then treated with HNO_3 acid 55% for 17 hours at 100 °C and washed until the pH reached 5-7 and dried in an oven for overnight at 90 °C.

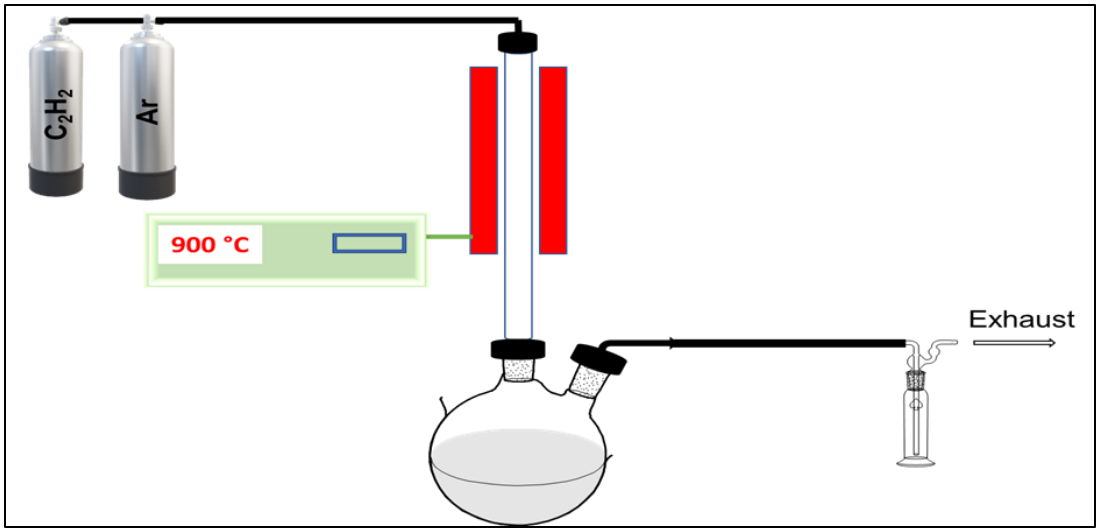

Figure 3.4: Vertical chemical vapour deposition for synthesise of carbon solid spheres.

3.7. Preparation of TiO_2/CNFs and TiO_2/CSs binary composites

Carbon based materials (carbon nanofibers and carbon spheres) (1 g) were dispersed in 20 mL of deionised water and sonicated (Bandelin sonorex sonicator) for 15 minutes at room temperature. Separately, 0.05, 0.1 and 0.2 g (5, 10 and 20 %) of TiF_4 was dissolved in 50 mL of *MB* extract and heated to form the precipitates. Then, each carbon-based material was mixed separately with 0.05, 0.1 and 0.2 g (5, 10 and 20 %) of TiF_4 *MB* extract solutions and sonicated for an hour at 80 °C to promote interaction. The resulting solutions were filtered with cellulose nitrate filter 0.45 µm, washed and the obtained powder were dried in an oven for a few hours. Thereafter, the materials were poured in a crucible and calcined in a muffle furnace at 500 °C for 2 hrs to form TiO_2/CNFs and TiO_2/CSs composites.

3.8. Preparation of CuO/TiO_2/CNFs and CuO/TiO_2/CSs ternary composites

Carbon based materials (1 g) were dispersed in 20 mL of deionised water and sonicated for 15 min. Separately, TiF_4 was dissolved in a 50 mL of *MB* extract and 0.02, 0.06 and 0.1 g (2, 6 and 10 %) of $Cu(NO_3)_2.6H_2O$ were also dissolved individually in *MB* extract. Then, the carbon based materials were mixed with $Cu(NO_3)_2.6H_2O$ and TiF_4 *MB* extract solution instantaneously and sonicated for an hour at 80 °C. The resulting solutions were filtered with cellulose nitrate filter, 0.45 µm and then the obtained powders were dried in an oven. Thereafter, the materials were poured in a crucible and calcined in a muffle furnace at 500 °C for 2 hrs to form CuO/TiO_2/CNFs and CuO/TiO_2/CSs composites.

3.9. Characterizations techniques

The synthesised nanomaterials were analysed to confirm their formation, chemical and physical properties. The samples were characterised using Liquid Chromatography-mass Spectrometry (LC-MS), Scanning Electron Microscopy (SEM), Transmission Electron Microscopy (TEM), X-ray Diffraction (XRD), Fourier Transform Infrared Spectroscopy (FTIR) and Ultraviolet-Visible spectroscopy (UV-Vis).

3.9.1. Liquid chromatography-mass spectrometry (LC-MS)

The possible chemical constituents of *Monsonia burkeana* extract were determined using waters synats G2 quadrupole time-of-flight (QTOF) mass spectrometer (MS) connected to a water acquity ultra-performance liquid chromatography (UPLC-MS) (Waters, Milford, MA, USA) analysis. Electrospray ionization was used in negative

mode with a cone voltage of 15 V, desolvation temperature of 275 °C, desolvation gas at 650 L/h, and the rest of the MS settings were optimized for best resolution and sensitivity. Data was acquired by scanning from m/z 150 to 1500 m/z in resolution mode as well as in MSE mode. In MSE mode, two channels of MS data were acquired, one at a low collision energy (4 V) and the second using a collision energy ramp (40−100 V) to obtain fragmentation data as well. Leucine enkephalin was used as lock mass (reference mass) for accurate mass determination and the instrument was calibrated with sodium formate. Separation was achieved on a Waters HSS T3, 2.1 × 100 mm, 1.7 µm column. An injection volume of 2 µL was used and the mobile phase consisted of 0.1% formic acid (solvent A) and acetonitrile containing 0.1% formic acid as solvent B. The gradient started at 100% solvent A for 1 min and changed to 28% B over 22 min in a linear way. It then went to 40% B over 50 s and a wash step of 1.5 min at 100% B, followed by re-equilibration to initial conditions for 4 min. The flow rate was 0.3 mL/min and the column temperature was maintained at 55 °C.

3.9.2. Ultraviolet-visible spectroscopy

The optical properties and concentration monitor were determined using Varian UV1009M258 UV-Visible spectrophotometer (Agilent technologies, Santa Clara, USA). The ZnO nanostructures were dissolved in 10% of HNO_3 acid solution and TiO_2 nanoparticles dispersed in distilled water using the sonication technique. To analyse, a 3 ml cuvette with 1 cm path length was inserted in a cuvette holder inside UV-vis instrument and the light was allowed to pass through the sample. A UV-Vis absorption spectrum was used to determine the metal oxide formation with the wavelength scan range from 200 to 800 nm. Monitoring of the organic dye was performed using a calibration curve obtained at 660 nm.

3.9.3. Fourier transform infrared spectroscopy (FTIR)

FTIR was used to confirm the functional groups, which are present in the plant extract and the synthesised materials. The FTIR analysis were taken on spectrum II Perkin Elmer (Boston, MA) FTIR spectrophotometer powdered. Before analysing the samples, the background was ran first to obtain the spectrum trail with a 4 cm^{-1} resolution and using a minimum of 32 scans. The spectra were recorded within the wavelength range of 400 to 4000 cm^{-1} and operated in reflectance mode.

3.9.4. Scanning electron microscopy (SEM)

SEM and EDS were used to analyse the morphology and composition of the synthesised nanomaterials respectively. A spatula tip amount of the samples were air dispersed on the carbon tape, they were coated with gold and mounted for analysis. An Auriga electron microscope instrument (Carl Zeiss Microscopy, Germany) equipped with a field emission gun operated at an acceleration of 200 kV voltage was used to analyse the morphology (for TiO_2 nanoparticles). A Quanta 200 FEG ESEM (FEI, Hillsboro, OR, USA) scanning electron microscope instrument equipped with a field emission gun accelerating at 200 kV voltage was used to analyse the morphology (for ZnO nanoparticles).

3.9.5. Transmission electron microscopy (TEM)

Morphology, particle size distribution and crystallinity were conducted using TEM and SAED respectively. The samples were dissolved in 5 µL of ethanol, then sonicated and each solution was deposited on the carbon coated copper grid. The copper grid was allowed to dry at room temperature for about 30 min. In these analyses, a Technai, G_2 F20 X-Twin MAT, (Eindhoven, Netherlands) electron microscope at an accelerating voltage of 200 kV with 48 µA emission current at an angle of illumination 15 ° was used. A JEOL JEM-2100 electron microscope (Japan) operated at an accelerating voltage of 200 kV recorded the TEM images.

3.9.6. X-ray diffraction (XRD)

The crystallinity and phase identification were determined using the XRD technique. XRD measurements were conducted on a Philips PW 1830 phaser (Amsterdam, Netherlands), using a Cu Kα radiation source as X-ray (ƛ=1.5405 Å) at room temperature. A voltage of 40 kV and a current of 40 Am were used respectively.

3.9.7. Thermal gravimetric analysis (TGA)

TGA was used to establish the thermal stability and phase transition of the nanoparticles. The thermal stability of each sample was determined with the use of a Perkin Elmer Pyris 1 TGA system. For TGA, each sample was heated to 900 °C at a rate of 10 °C/min under air (20 mL/min). The mass of each sample was kept constant (ca. 10 mg) to reduce any effects in the variability of samples.

3.10. Simulated wastewater treatment using batch photocatalysis experiment.

The activity of the photocatalyst was demonstrated by photodegradation of methylene blue (MB) under ultraviolet light (300W Ultra-Vitalux, OSRAM, USA). Photocatalytic degradation of MB solution at various pH, concentration, dosage and time was monitored using a UV-Vis spectrophotometer. The concentration measurements were done with the maximum absorption wavelength of MB at 660 nm. The calibration curve was constructed and used to estimate the photocatalytic degradation of MB solution.

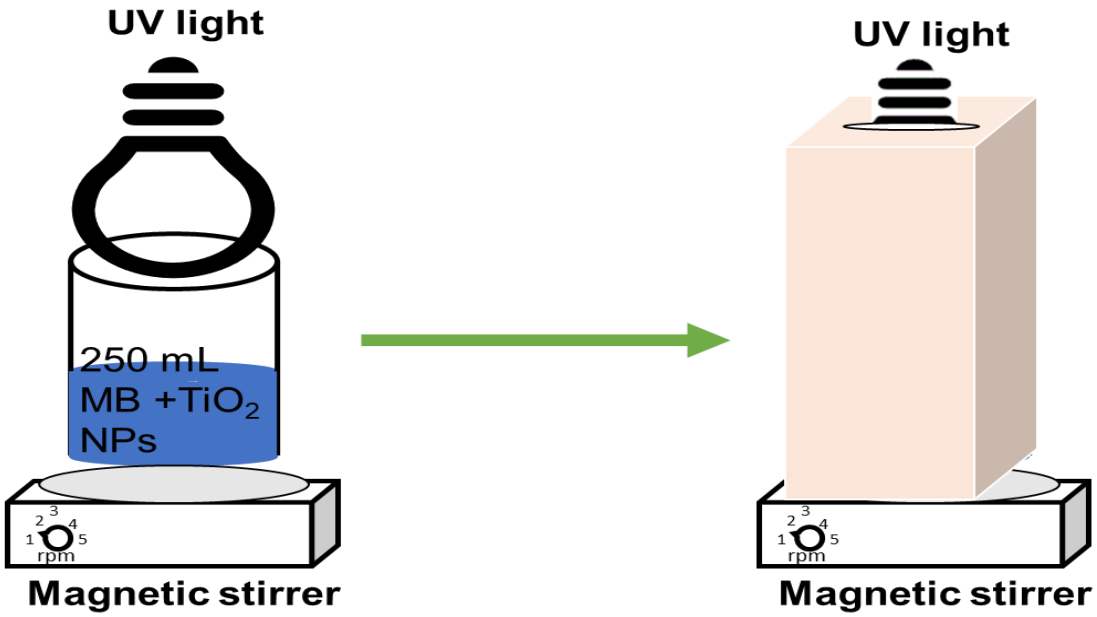

Figure 3.5: Photocatalysis set up.

3.10.1. Photocatalytic activity of the prepared nanoparticles using *Monsonia burkeana* plant extract

To test the photocatalytic activity of the nanoparticles, a 250 mL MB solution with an initial concentration of 20 mg/L was prepared in a 250 mL volumetric flask. An amount of 20 mg of the photocatalysts was introduced into the solution to initiate degradation of MB. Prior to UV irradiation, the solution containing the photocatalysts was stirred continuously for about an hour in the dark to reach an adsorption-desorption equilibrium so that the degradation efficiency can be influenced by photodegradation. After reaching the equilibrium, the system was subjected to UV irradiation using 300 W LED as a light source. The distance between the light source and solution surface was kept constant at about 5 cm throughout the photocatalytic experiments. The sample was irradiated for a certain amount of time with temperature regulated between

65-70 °C by exchanging water in a bowl and analysis for the degree of degradation was taken at 30 min intervals for 2 hours. The method was used to investigate the metal oxides (TiO_2 and ZnO) for their photocatalytic activity using variables such as pH (4-10) of the solution, contact time (30 to 120 min) between the photocatalyst and pollutant, concentration (10 to 40 ppm) of the pollutant in solution, dosage (20 to 80 mg) of the photocatalyst investigated to obtain the optimum conditions. Reaction kinetics calculations were also conducted to try and identify which model the material fits in.

3.10.2. Reusability of prepared nanoparticles using *Monsonia burkeana* plant extract.

Reusability studies were conducted to determine the effectiveness and strength of the metal oxide nanostructures. The metal oxide nanostructures were recovered after completion of photocatalytic degradation process and washed with ethanol to remove the residues on the surface. Reusability was done over 4 consecutive cycles with the following conditions pH 10, concentration 20 ppm, dosage 60 mg and time 120 min.

3.10.3. Photocatalytic activity of binary composite of carbon based materials (CSs and CNFs) with *Monsonia burkeana* plant extract derivative TiO_2 and ternary composite with *Monsonia burkeana* derivative CuO.

To evaluate the photocatalytic activity of the binary and ternary composites, the optimum conditions used were pH(10), concentration (20 ppm) and dosage (60 mg). The photocatalytic activity of different percentages of TiO_2 loading 5, 10 and 20 % on CSs and CNFs as well as for 2, 6 and 10% CuO loading on 20%-TiO_2/CSs and 20%-TiO_2/CNFs were examined over a period of 3 hrs in 30 min intervals. An amount of 60 mg of the binary and ternary composites was used to degrade 250 mL methylene blue solution of 20 mg/mL at a pH of 10.

3.11. Antibacterial activity of nanoparticles prepared using *Monsonia burkeana* plant extract against model pollutants

The nutrient broth was prepared following the manufacturer's instructions. The prepared broth was poured into four Erlenmeyer flasks and in each of the flasks, one colony of *E. coli, S. aureus, P. aeruginosa and E. faecalis* were inoculated and the growth of the bacteria was conducted. The flasks were incubated at 37 °C for 24 hours to allow for growth of the bacteria. After the growth, the bacterial culture was

centrifuged, and the pellets were obtained. Sterilised tap water in the four Erlenmeyer flasks were seeded with bacterial culture (pellet). Each flask was then seeded with a different bacterial strain and the spread plate technique was used to enumerate the number of bacteria of the seeded water. The seeded water was then dispensed into 5 sterilised flasks for each of the bacterial cultures. The water was then treated with different concentrations (0.005 µg/mL, 0.010 µg/ml, 0.020 µg/mL and 0.050 µg/mL) of the nanoparticles. The treated water was then incubated at 37 °C for 24 hours. Following incubation, the spread plate technique was used to enumerate the bacteria after treatment.

3.12. Analysis and treatment of bacteria from real water

Treatment and analysis of tap, sewage, pond and river water was conducted to test for the presence of bacterial strains (*E. coli, Enterobacteriaceae)* and total population of microorganisms (*aerobic count*). For the preparation, aliquots of 10 mL of each water type was diluted with peptone water (broth) and 100 mL of sterile distilled water. From the mixture, 1 mL of the mixture was added to the dehydrated media before treatment. For the inoculation, treatment was performed using two concentrations, (0.005 mg/mL and 0.05 mg/mL) and incubated at 37 °C for 24 hours (*E. coli, Enterobacteriaceae)* and 48 hours for aerobic count and total coliform. The sample information was loaded onto the tempo reader system and the mixtures were loaded onto the count cards and incubated for 24 hours at 37 °C for (*E. coli, Enterobacteriaceae*) and *Aerobic. count* for 48 hours, respectively. The results were then read using the tempo reader.

3.13. Summary

This chapter outlined five main technologies in the study namely green synthesis, green synthesised composites, characterisation techniques, photocatalysis and antibacterial. Green chemistry was used to prepare ZnO and TiO_2 nanoparticles. CNFs and CSs were prepared using horizontal and vertical chemical vapour deposition, respectively. Green synthesised metal oxides composite with carbonmbased materials were also prepared. LC-MS and FTIR were used to analyse the components found in *Monsonia burkeana* water extract. FTIR and UV- vis was used to study the optical properties of the metal oxide nanoparticles. Further, to confirm the formation of the metal oxide nanoparticles by vibration band and absorption of wavelength, respectively. SEM, EDS, TEM and SAED were probed to analyse morphology, composition, particle size and crystallinity, respectively. XRD was used to analyse the phase purity of the synthesised materials. TGA was used to analyse the thermal stability. The evaluation of antibacterial and photocatalyst properties of ZnO and TiO_2 nanoparticles were conducted. Binary and ternary composites were tested for photocatalytic activity. Chapter 4 and chapter 5 details the interpretation of the output analysis in the study.

Chapter 4

Biosynthesis of zinc oxide and titanium dioxide nanoparticles using *Monsonia burkeana* for wastewater treatment

---

4. Introduction

Over the decades, titanium dioxide (TiO_2) and zinc oxide (ZnO) nanostructures have gained popularity in environmental remediation via photocatalysis. Both TiO_2 and ZnO are the most extensively studied semiconductors, explored for the degradation of organic dyes and antimicrobial purposes. This is due to them being cost effective, low-toxicity, high stability, chemically and biologically inert [274, 275]. These semiconductors have been shown to offer excellent optical properties, electronic, photocatalytic activity and antibacterial activity, however, that also depends on the size, crystallinity and morphology [276, 277, 278, 279, 280, 281, 282]. In this chapter, the use of a plant extract which consists of constituents that act as reducing, capping and stabilising agents was investigated. The synthesis of ZnO and TiO_2 using *Monsonia burkeana* plant extract was conducted. Their photocatalytic and antibacterial activity against dyes and bacteria, respectively was investigated.

4.1. Qualitative analysis of *Monsonia burkeana* extract

Qualitative analysis of *Monsonia burkena* extract was conducted through LC-MS which assisted in the determination of the molecular weight of fragments in the extract. According to the LC-MS analysis, only three possible compounds were found in water *Monsonia burkeana* plant extract as demonstrated in Table 4.1.

Table 4.1 Compounds found in *Monsonia burkeana* water extract using LC-MS.

Retention time	Molecular formula	Molecular weight	Compound name	Group name	Biological activity
6-10	$C_{34}H_{23}O_{22}$	783.06	Granatin	Tannin	Antioxidants and anticancer [283]
16-18	$C_{26}H_{27}O_{16}$	595.13	quercetin 3-O-ß-xylopyranosyl-(1,2)O-ß-galactopyranoside	flavonol glycoside	Not reported
18-20	$C_{14}H_5O_8$	301.10	Ellagic acid	Phenolic	Antioxidants, anti-inflammatory and antibacterial activity [284, 285]

Table 4.1 summarises the results obtained by LC-MS and the reported biological activity of possible compounds and are additionally structurally represented in Figure 4.1. The LC-MS analysis identified the presence of tannins, flavanol glycoside and phenolic constituents. The mass to charge ratio (m/z) obtained from the coupled LC-MS data was used to come up with the possible organic structures that are drawn in Figure 4.1. The *Monsonia burkeana* extract is reported to contain the highest content of total phenolic, tannins and total antioxidants activity [11]. These constituents are known to be biologically active which can assist in the treatment of various pollutants. To further confirm the use of this plant and the possible phytochemical constituents, FTIR was done.

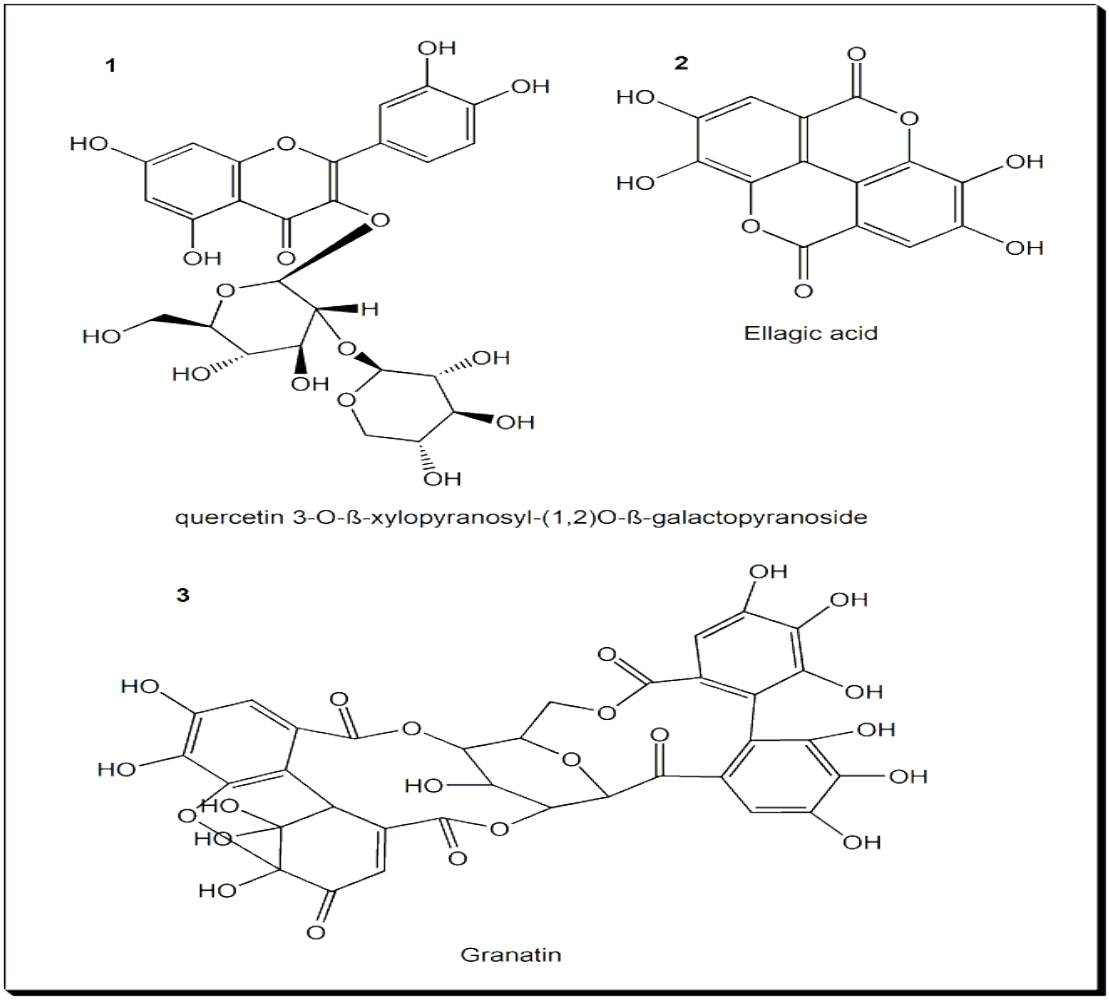

Figure 4.1: Chemical compound found in *Monsonia burkeana*.

4.2. Spectroscopic analysis

FTIR analysis was conducted to examine the constituents that influenced the formation of ZnO and TiO_2 nanoparticles. The FTIR was used to identify groups in *Monsonia burkeana* plant extract, ZnO and TiO_2 nanostructures.

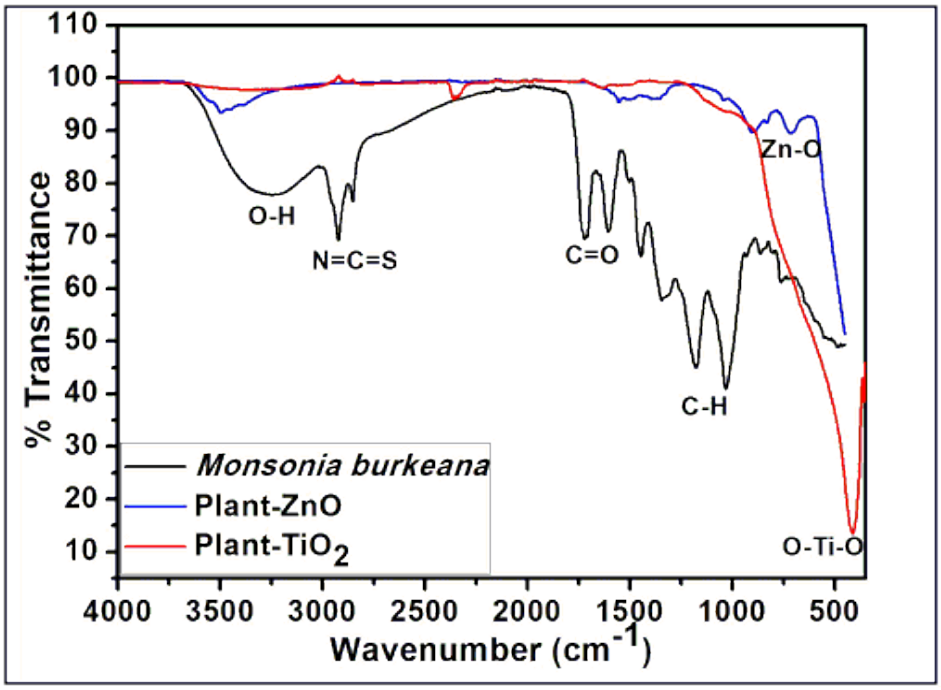

Figure 4.2: FTIR of *Monsonia burkeana*, ZnO and TiO_2 nanoparticles.

The FTIR analysis of the *Monsonia burkeana* plant extract, TiO_2 and ZnO plant nanoparticles revealed that there was a presence of functional groups ascribed to both the extract and the nanoparticles. In Figure. 4.2, the *Monsonia burkeana* extract showed vibrational stretching's at 3000-3500, 2750-2875, 1500-1750 and 1000-1250 cm^{-1} spectral regions. The broad peak at 3000–3500 cm^{-1} could be assigned to the following possible groups, OH, NH_2, HO−C═O, H_3CO and C–H aromatic stretching vibration of different bioactive compounds. The vibrational stretching at 2750–2875 cm^{-1} corresponds to the presence of bioactive thiamine N═C═S stretching vibrations that were identified, while the spectral region at 1500–1750 cm^{-1} was due to C═O and C═N bonds. In addition, the stretching vibration located at 1000 –1250 cm^{-1} showed an absorption region consisting of OH, NH, C−H and C═C aromatic compounds and C—O phenol compounds. It is believed that the ZnO and TiO_2 vibrations stretching appears below 1000 cm^{-1} at the fingerprint region. The phytochemicals in the *Monsonia burkeana* served as stabilizers and capping agents. The FTIR spectrum of *Monsonia burkeana* derived ZnO, showed there was a small peak at around 500 cm^{-1} which indicates ZnO vibrations [14] and TiO_2 was indicated at 497 cm^{-1}. In addition, other peaks on the spectral region of OH, NH_2, HO−C═O, H_3CO may be due to compounds from the plant extract. These functional groups within

the compound can enhance the biological properties of ZnO derived from the plant extract. The TiO_2 spectrum showed less distinct functional groups present. This indicates that during the calcination process, some of the functional groups were removed or denatured from the TiO_2, thus, could not be identified.

In an effort to understand how the interaction between the metal salt coupled with various biological compounds contained in the plant extracts interacts, several authors [286, 287] have shown the possible mechanisms of formation. In this study, Zn is used to illustrate the interaction. During the synthesis, $ZnCl_2$ served as an oxidant while the plant extract phytochemicals acted as a reducing agent. The *Monsonia burkeana* plant extract is known to contain mostly phenolic acids, flavonoids, polyphenols and tannins compounds [16]. In solution, the Zn^{2+} ions from the $ZnCl_2$ precursor dissociated and attached to the polyphenols from the plant extract, thus being reduced to ZnO. After the chelation of the metals to the ligands, a complex was formed (Zn^{2+}-polyphenols) [161]. This phenomenon was also confirmed by the FTIR (Figure 4.2) as shown, where some of the phytochemicals found in the plant were found in the ZnO plant, thus enhancing the ZnO properties. Furthermore, on evaluation of formation of metal oxides nanoparticles, it is important to analyse aqueous solution of nanoparticles with UV-vis spectrophotometer.

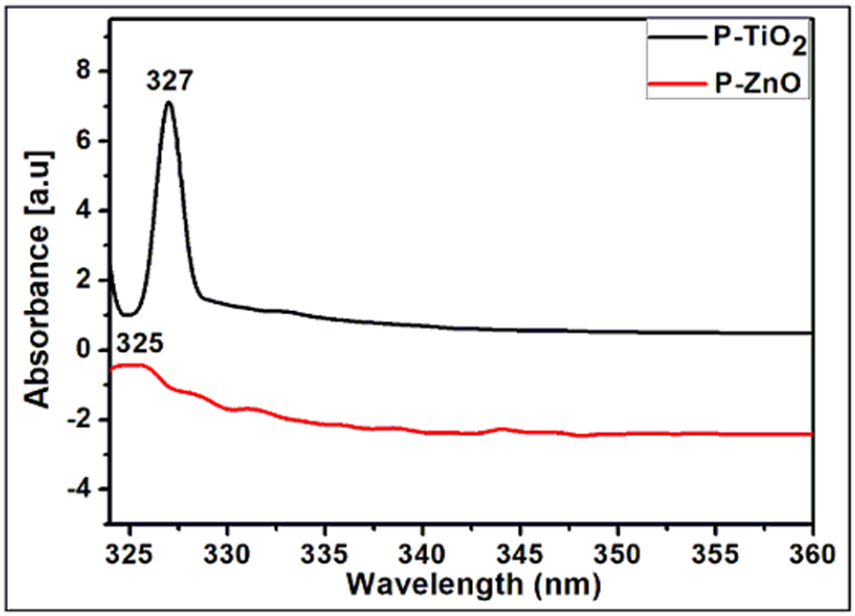

Figure 4.3: UV-vis spectra and tauc plot of ZnO and TiO_2 nanoparticles.

UV-vis spectroscopy was used to understand the optical properties and formation of the ZnO and TiO_2 nanoparticles. The spectrum demonstrated exciton absorption peak profile of the characterised ZnO and TiO_2 nanoparticles. Both ZnO and TiO_2 nanoparticles samples appeared at the ultraviolet region. TiO_2 nanoparticles exhibited a strong UV absorption at the wavelength of 327 nm and ZnO nanoparticles had an excitation peak exhibited at 325 nm. The indicated absorption bands were at a lower wavelength than in most of the reported materials (370 to 388 nm) [90, 98]. This may be attributed to the agglomeration and settling of nanoparticles [165]. In addition, tauc plot (Figure S2(a, b)) was constructed to determine the band gap of ZnO and TiO_2 nanoparticles. The following equation was used for tauc 's plot:

$$(\boldsymbol{ahv}) = \boldsymbol{A}(\boldsymbol{hv} - \boldsymbol{Eg})^{\boldsymbol{n}} \qquad \textbf{(1)}$$

Where h, v, α and Eg are planks constant, frequency, absorption coefficient and band gap, respectively. A is the proportionality constant and n for direct transition. Tauc plot is $(\alpha hv)^2$ a function of photon energy with respect to photon energy (hv), extrapolating on the plot, a band gap was estimated as 3.54 eV (ZnO) and 3.53 eV (TiO_2) which is larger than some values indicated in literature [288, 289, 20, 21]. This could be attributed to the smaller crystal size of the prepared ZnO and TiO_2 nanoparticles. Peng *et al*., [290] studied the size quantazition effect on the band gap and observed that smaller crystal size is linked to a larger band gap.

4.3. Morphological analysis

The morphological and structural features of the prepared ZnO and TiO_2 nanoparticles using *Monsonia burkeana* plant water extract were performed using TEM and SEM. In addition, the composition and crystallinity were determined by EDX and SAED respectively.

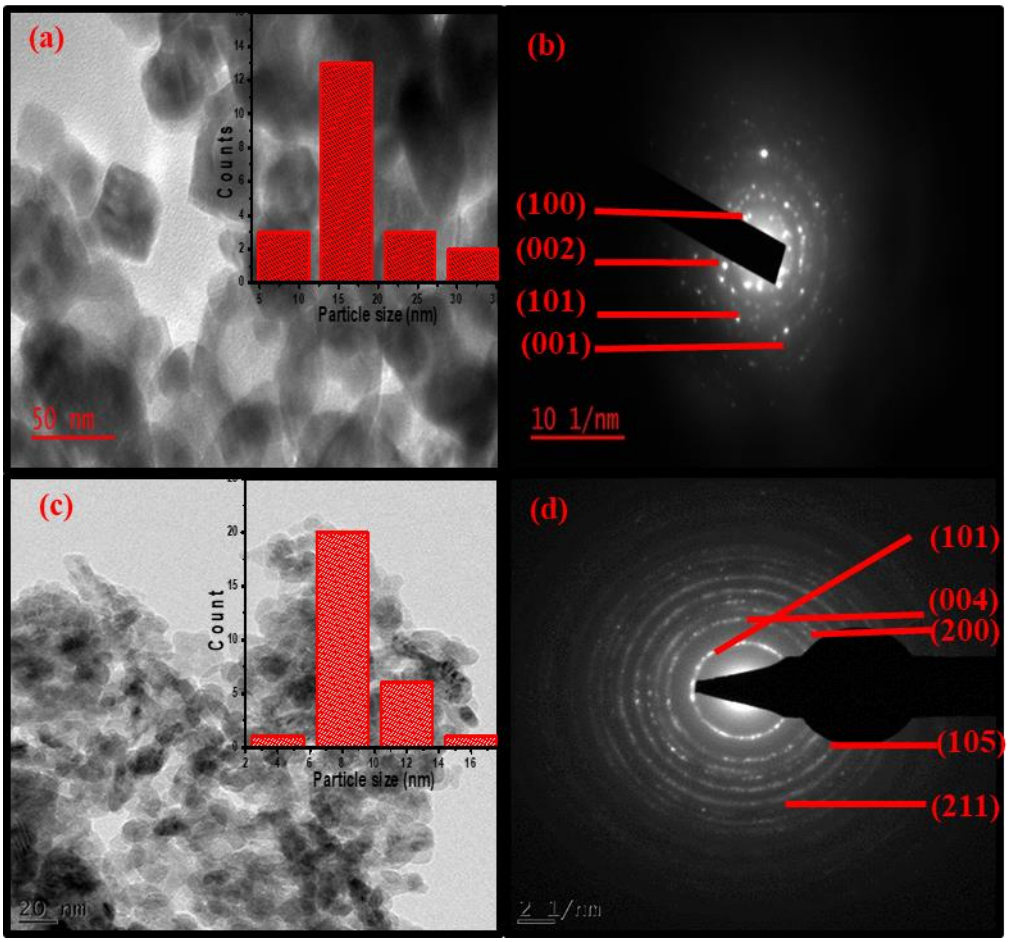

Figure 4.4: (a) TEM image and particle size distribution of ZnO nanoparticles (b) SAED of ZnO nanoparticles (c) TEM image and particle size distribution TiO_2 nanoparticles (d) SAED of TiO_2 nanoparticles.

Figure 4.4c represents TiO_2 nanoparticles showing a spherical shape and agglomeration since they are small sized particles whereas, Figure 4.4a shows ZnO nanoparticles with spherical shape as well as a large hexagonal shape and less agglomeration which might be due to the large size. Furthermore, TEM assisted in the determination of average particle size distribution. The particle size of ZnO nanoparticles showed a broad distribution from 5 to 35 nm, similarly TiO_2 nanoparticles had a broad size distribution ranging from 2 to 18 nm. The particle size distribution displayed the major series of particles size between 10 and 20 nm for ZnO nanoparticles, whereas TiO_2 nanoparticles had a dominating average particle size between 6 and 10 nm. The variation in size was observed because during the reduction of metal precursor by phytochemicals, the metal nanoparticles formed at

different times. According to the measured average particle size (inversely proportional to the surface area) it can be deduced that TiO_2 nanoparticles might have a higher surface area than ZnO nanoparticles. This reduced particle size could assist in the performance of these materials for antibacterial and photocatalytic activity. For SAED in Figure 4.3(b, d), the rings of ZnO and TiO_2 nanoparticles were visible. They showed that the nanoparticles were crystalline with some of the ZnO and TiO_2 diffraction rings corresponding to the peaks that were identified in Figure 4.6(a, b) via XRD. The deduced patterns for ZnO nanoparticles and TiO_2 nanoparticles are as follows (100), (002), (101) and (001) and (101), (004), (200), (105) and (211) respectively. The evidence of these nanoparticles was further analysed by SEM as shown in Figure 4.5.

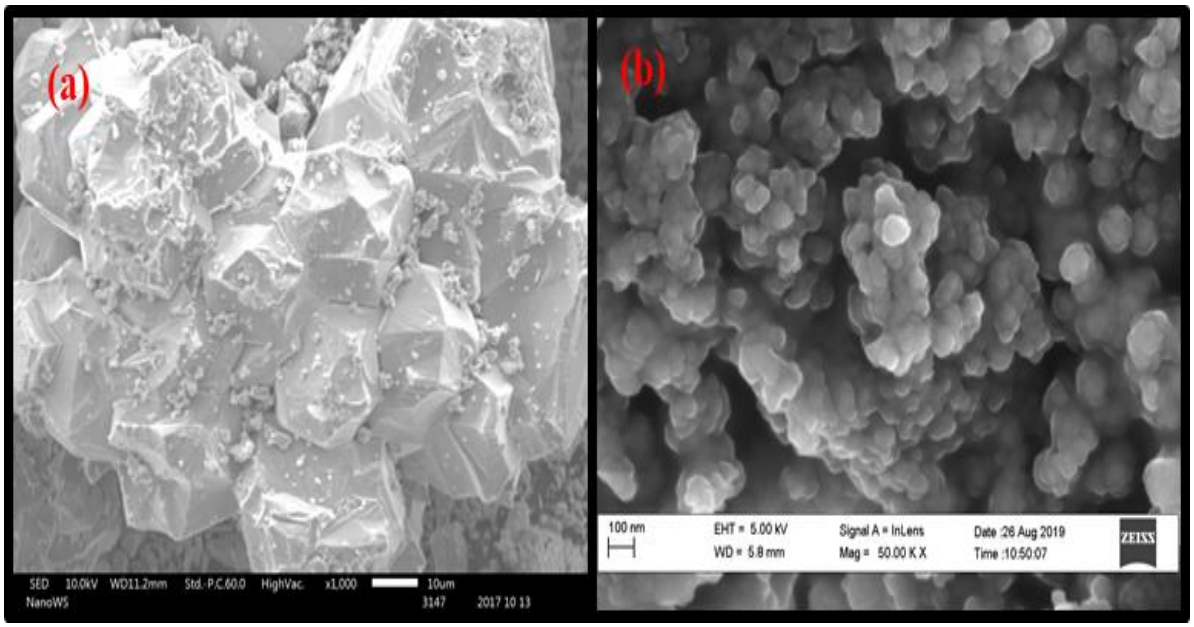

Figure 4.5: (a) SEM image of ZnO, (b) TiO_2 nanoparticles, of (c) ZnO, (d) TiO_2 nanoparticles.

The obtained SEM images of ZnO and TiO_2 nanoparticles showed differing features, as was shown even in TEM. The ZnO nanoparticles (Figure 4.5(a)), exhibited a hexagonal wurtzite structure, which is a characteristic of a ZnO structure. The surface study conducted on the TiO_2 nanoparticles showed a spherical shape and smooth surface. To further confirm the formation of these materials, their crystallinity, phase identification and structure were analysed.

4.4. Structural analysis

XRD was used to confirm the formation of green synthesised ZnO and TiO_2 nanoparticles prepared using *Monsonia burkeana* water extract.

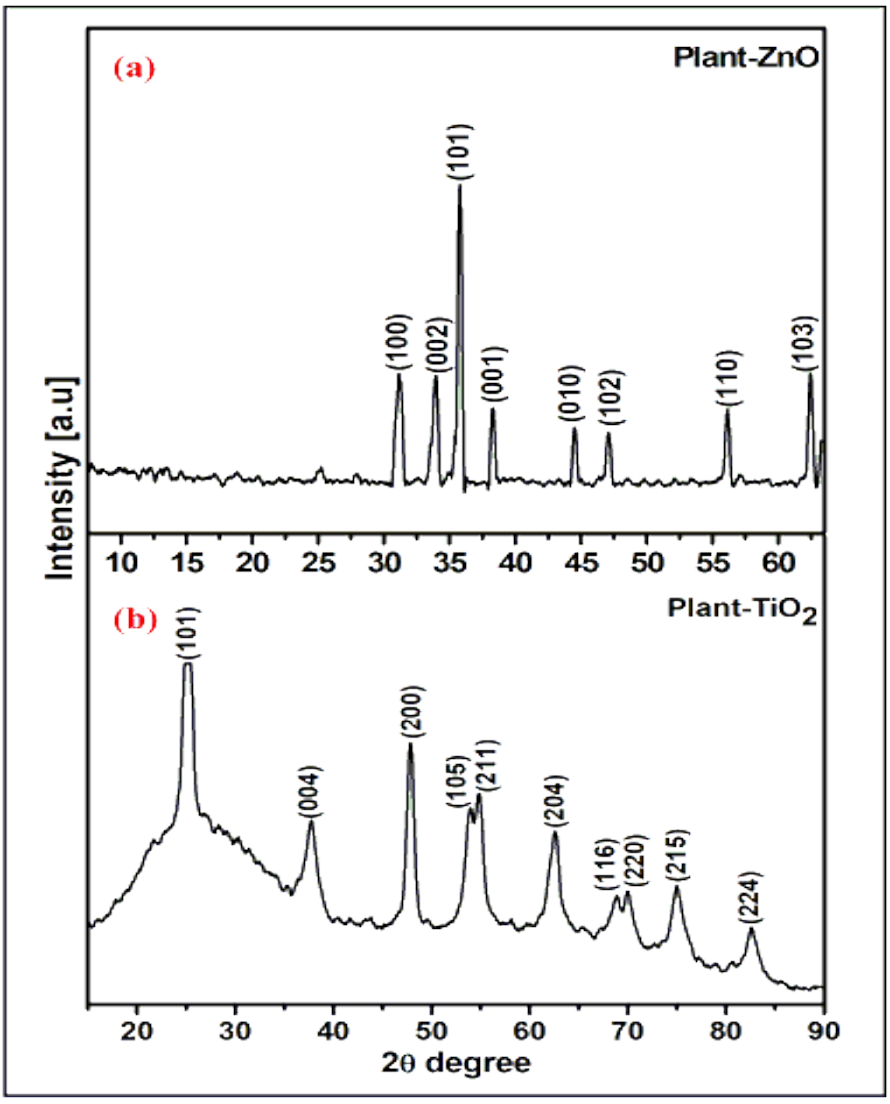

Figure 4.6: XRD of green synthesised (a) ZnO and (b) TiO_2 nanoparticles.

The XRD patterns of ZnO and TiO_2 nanoparticles are shown in Figure 4.6(a, b) respectively. In Figure 4.6a, the crystalline peaks positioned at 2θ of 31.3, 34.5, 36.30, 39.3, 44.4, 47.5, 56.1 and 62.8 ^{o} correspond to the indexes (100), (002), (101), (001), (010), (102), (110) and (103) cornfirmed using JCP2-36-1451. These diffraction peaks are typical of a hexagonal wurtzite structure and confirm the formation of ZnO

nanoparticles. This diffraction pattern corresponds to the reported ZnO nanoparticles that confirm that indeed ZnO was formed by *Monsonia burkeana* water extract. TiO_2 consists of three polymorphs which differ due to the synthesis temperature. In this study, TiO_2 was synthesised, then calcined at 500 °C. The characteristics of diffraction peaks of the sample indicates the material was crystalline with diffraction angles 25.3, 37.6, 47.9, 53.9, 54,1, 62.4, 68.3, 69.5, 75.0 and 82.5 ° corresponding to the following planes (101), (004), (200), (105), (211), (204), (116), (220), (215) and (224) which validates the TiO_2 anatase phase, confirmed using JCP 2-21-1272 standard. The diffraction angle perceived at 25.5° was associated with the (101) crystallographic plane of TiO_2 anatase only. The crystallite size for ZnO and TiO_2 nanoparticles were estimated using the Scherer equation:

$$\boldsymbol{D = \frac{0.9l}{\beta cos\theta}}, \qquad \textbf{(2)}$$

Where, D is the mean diameter of nanoparticles, 0.9 is a constant crystalline shape factor, l is the wavelength of X-ray radiation source, β is the angular full width at half maximum peaks recorded at diffraction angle 2θ and θ is the bragg's diffraction angle. Scherrer crystallite size for ZnO and TiO_2 was found to be 18.6 nm and 8.93 respectively. These results corroborate with the calculated sizes obtained from TEM (Figure 4.4 (a, c)) as the sizes obtained fall within the calculated particle size distribution. The diffraction peak for TiO_2 at 25.5 ° was also broad, which could have contributed to the small crystalline size.

4.5. Thermal stability analysis

Thermogravimetric analysis was carried out to evaluate the thermal stability of the green synthesised ZnO and TiO_2 nanoparticles. Figure 4.7 (a-b) shows a thermalstability and derivative profiles of green synthesised ZnO and TiO_2

nanoparticles.

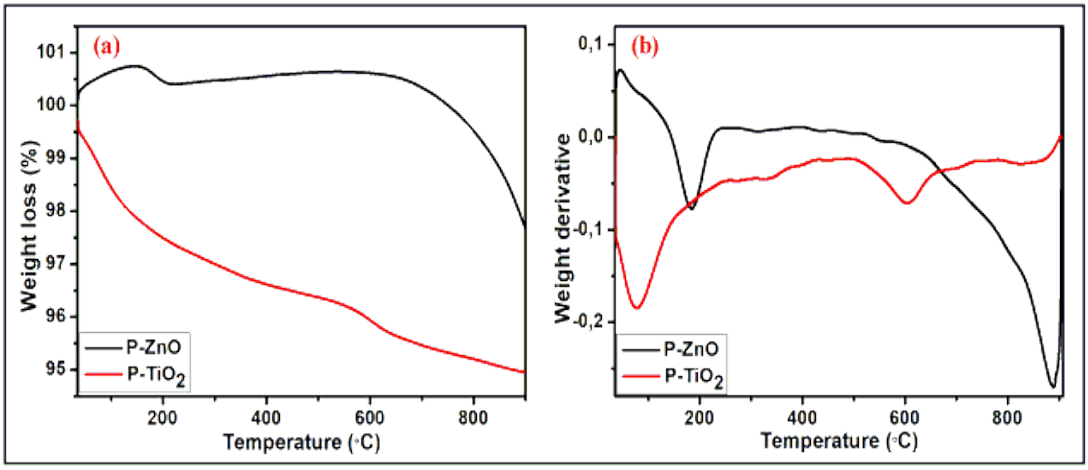

Figure 4.7: (a) Thermalgravetric analysis and (b) Direvitive of ZnO and TiO_2 nanoparticles.

Figure 4.7a shows that at around 150 °C for both the nanoparticles, the TGA curves showed a first phase of weight loss which could be due to water molecules from the plant extract. Moreover, TiO_2 nanoparticles showed a rapid but minimal weight loss of 5% in the temperature range 35 °C ≤ T ≤ 900 °C. The thermogram shows that ZnO nanoparticles were more thermally stable as compared to TiO_2 nanoparticles. However, ZnO shows a weight gain above 100% which could be attributed to the oxidation of nanoparticles surface due to impurities. Figure 4.7b shows a derivative of ZnO and TiO_2 nanoparticles with two phases at 200 °C and 890 °C and 80 °C and 600 °C, respectively. The derivative peaks are broad indicating that the nanoparticles are not pure. This could be attributed to the moieties of *Monsonia burkeana* extract absorbed on the nanoparticles surface.

4.6. Photocatalytic activity of green synthesised ZnO and TiO_2 nanoparticles.

The photocatalytic activity performance of green synthesised ZnO and TiO_2 nanoparticles was evaluated with methylene blue dye solution under UV irradiation. The 250 ml solution with catalyst was allowed to reach an adsorption-desorption equilibrium over 60 min in the dark. Since the methylene blue was absorbed on the surface of the catalyst. It was therefore, covered with the dark box to ensure only light had an effect on the degradation. The percentage of degradation was calculated using the following equation:

$$C = \frac{C_o - C}{C_o} \times 100\% \qquad (3)$$

Where C_o is the desired initial concentration and C is the concentration at irradiation time. To obtain the optimal conditions of MB degradation using these newly green synthesised materials, various parameters were tested.

4.5.1. The study of pH

Solution pH plays an important role in photocatalytic degradation of organic dyes. The photocatalytic efficiency is controlled by the surface charge and production of hydroxyl radicals. To get a desired pH, pH was adjusted using 0.1 M NaOH and 0.1 M HCl.

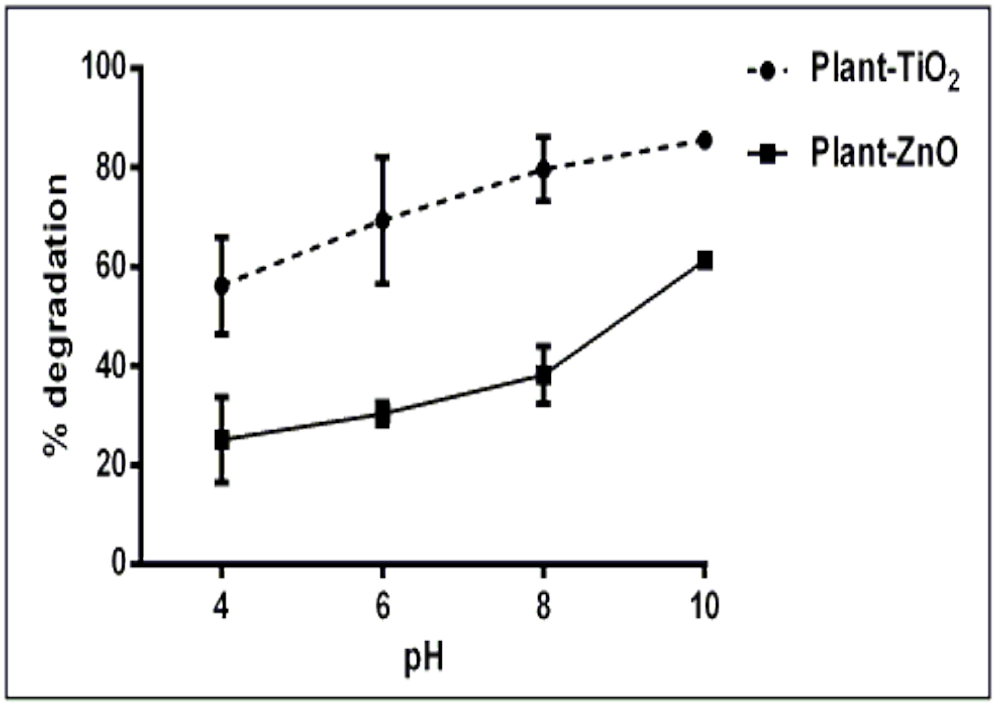

Figure 4.8: Study of pH solution of methylene blue.

In these batch experiments, the pH was varied from 4 to 10 with an interval of 2 represented in Figure 4.8. It can be observed that the percentage of degradation increased with an increase in pH, indicating that the degradation favours basic conditions [291]. At the pH of 10, TiO_2 and ZnO nanoparticles had the highest percentage degradation of MB with 85.5% and 61.3%, respectively. This observation could be related to the surface charge [292, 293]. Effective adsorption capacity is known to be dependent on electrostatic attraction force between two substances. The

solution pH affected the surface charge of ZnO and TiO_2 nanoparticles. ZnO and TiO_2 nanoparticles become negatively charged with an increase in pH. The negatively charged nanostructures and positively charged methylene blue dye [85] resulted in electrostatic attraction forces which intensified the adsorption [294]. Therefore, enhancing the photocatalytic degradation of methylene blue. At lower pH levels, ZnO degraded 25.2% whereas TiO_2 degraded 56.2%, since there were more positive surface charges of the catalyst which could have caused a repulsion because of unlike charges, leading to a weak adsorption.

4.6.2. The study of dosage

Pre-adsorption of methylene blue on a photocatalyst is a key step in photocatalysis to obtain an efficient photocatalytic degradation. However, adsorption is related to the availability of active sites on the surface of ZnO and TiO_2 nanoparticles. The effect of ZnO and TiO_2 nanoparticles dosage were studied from 20 to 80 mg, using intervals of 20 mg in 250 mL using modelled methylene blue pollutant solution at pH 10. The results are shown in Figure 4.8.

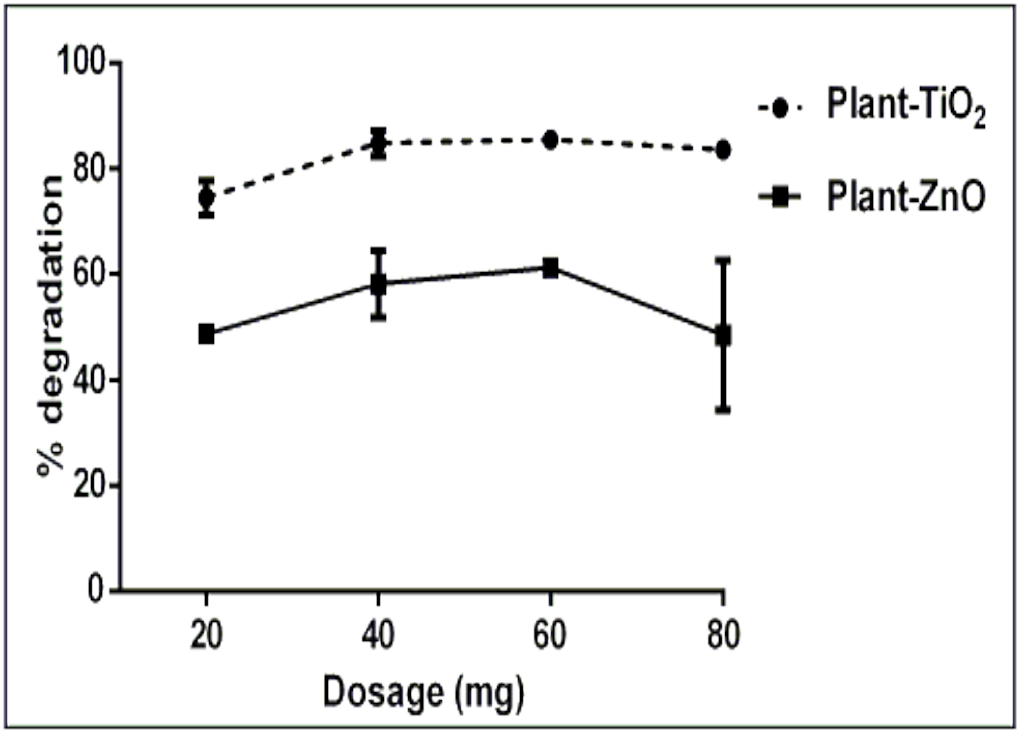

Figure 4.9: Study of mass of photocatalysts.

Figure 4.9 shows that the percentage degradation increased from 20 to 60 mg and decreased at 80 mg for both the nanostructures. Increasing the dosage of nanoparticles caused turbidity in the solution which could have resulted in the scattering of light [295]. Scattering of light leads to less light absorbed by the nanoparticles limiting the photocatalytic degradation performance. For ZnO nanoparticles, the decrease in percentage degradation was significant compared to TiO_2 nanoparticles due to the large sized nanoparticles which caused suspension in the solution. Theoretically, under these conditions, at 80 mg of photocatalyst, these materials are expected to have a higher percentage of degradation. In addition, an increase in dosage brings in more available active sites to accommodate more of the methylene blue. However, the most effective dosage was obtained at 60 mg for both ZnO and TiO_2 nanoparticles degrading 85.5% and 64.3% of methylene blue solution, respectively. To further study the concentration of the methylene blue solution optimum dosage and pH were used.

4.6.3. The study of dye concentration

The amount of pollutant in water tends to influence the behaviour of light that is supposed to activate electron-pair and generation of radicals on the ZnO and TiO_2 nanoparticles [295]. The effect of initial concentration of methylene blue on photocatalytic degradation is shown in Figure 4.10.

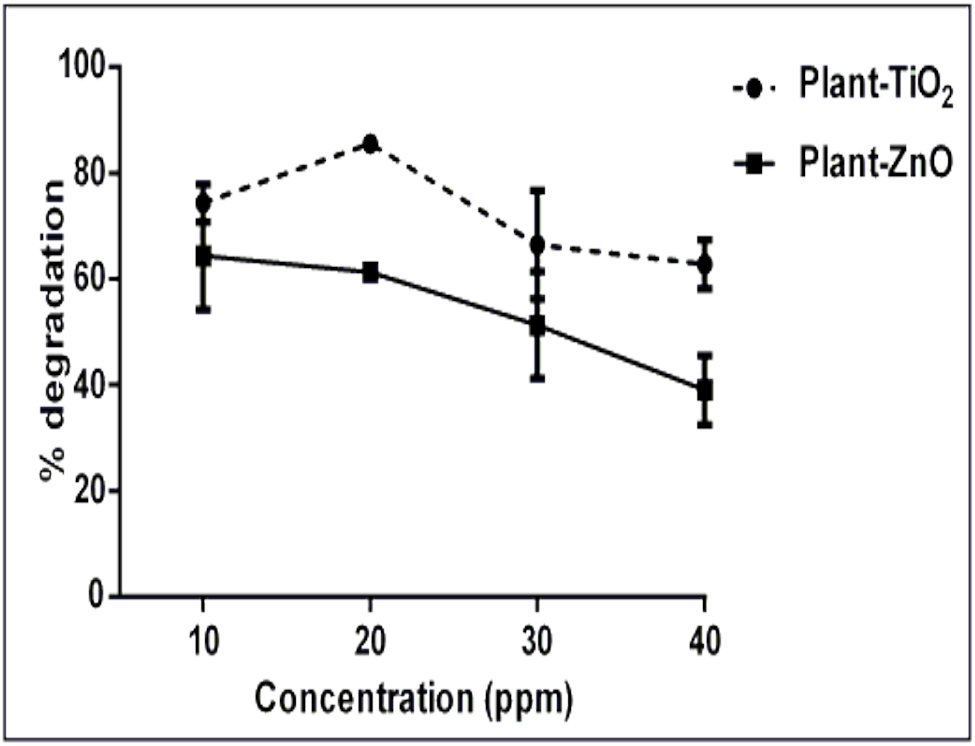

Figure 4.10: Study of concentration of methylene blue.

The effect of concentration was investigated using an optimum dosage of 60 mg and pH of 10 in 250 mL for 120 min. The concentration was varied using 10 ppm intervals having 10, 20, 30 and 40 ppm. At higher concentrations, 30 and 40 ppm showed significant low percentage degradation for both nanostructures compared to 10 and 20 ppm. The reason could be that at higher concentrations of 30 and 40 ppm dye, the light that is illuminated was restricted as too much of the dye resulted in the inability of the light to penetrate, thus resulting in the inability of the interaction with the photocatalyst. In addition, this could result from constant dosage (60 mg) used, that generates the same number of hydroxyl radicals throughout the variation of concentration. Thus, the number of hydroxyl radicals that attack the dye cannot withstand the number of MB molecules with an increase in concentration. Hence, photocatalytic degradation decreased. In comparison, the percentage of degradation decreased from 85.5% to 62.8% for TiO_2 nanoparticles whereas, percentage of degradation for ZnO nanoparticles decreased from 64.3% to 39.0% with an increase in concentration. It was observed that percentage of degradation is influenced by the concentration of MB solution.

4.6.4. The study of irradiation time

The droughts of water affect the industrial production and domestic productivity. Hence, wastewater treatment must be efficient within acceptable period. This has led to the investigation of contact time between photocatalyst and MB solution. The pH(10), dosage (60 mg), and concentration (20 ppm) were used. Time was varied by a 30 minute interval for 180 minutes.

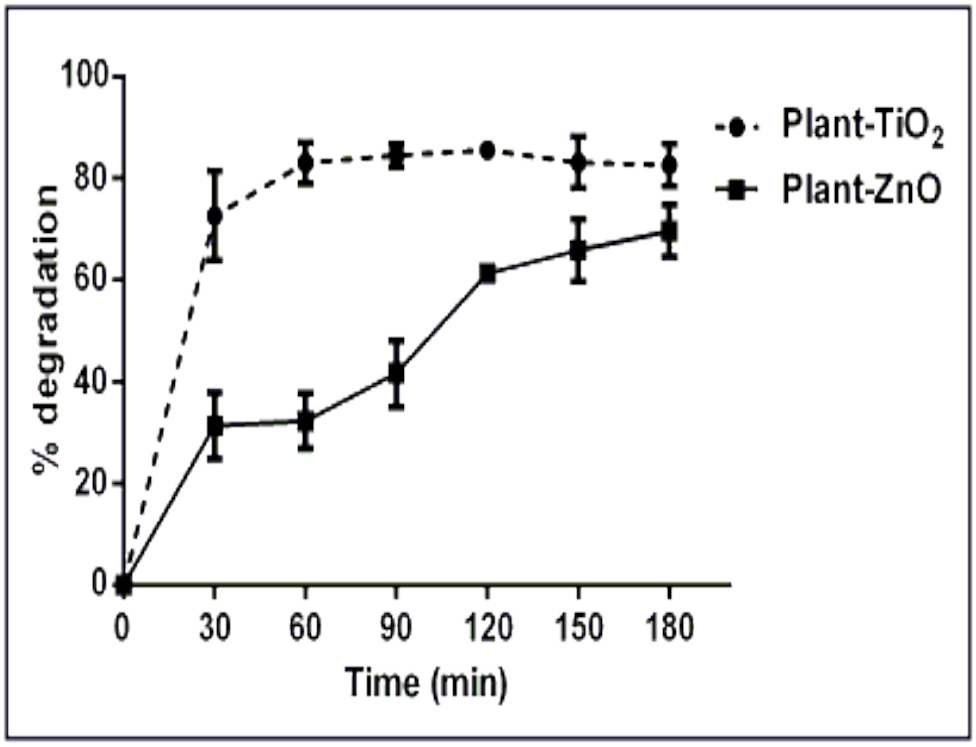

Figure 4.11: The effect of time on the photodegradation of MB using TiO_2 and ZnO nanoparticles.

Figure 4.11 indicates the photocatalytic degradation of MB using green synthesised TiO_2 and ZnO nanoparticles with respect to time. Both the materials are comparable between 0 to 120 minutes, i.e. at 120 minutes the amounts degraded were 85,5% and 61.3% for TiO_2 and ZnO nanoparticles, respectively. The percentage of degradation increased with an increase in exposure time to UV irradiation for all the metal oxides. This observation can be attributed to the large number of hydroxyl radicals generated with time. However, TiO_2 nanoparticles had a higher absorption capacity which could be attributed to the small size obtained from TEM analysis. The absorption took longer for ZnO nanoparticles, resulting in slower degradation. Moreover, TiO_2 nanoparticles

after 120 minutes slightly decreased. The decrease in percentage of degradation for TiO_2 nanoparticles could be due to a decrease in availability of active sites. However, the TiO_2 and ZnO nanoparticles still had a high percentage of degradation at 180 minutes, 82.7% and 71.5%, respectively.

4.6.5. The study of kinetics of methylene blue

The photocatalytic behaviour of ZnO and TiO_2 nanoparticles was further analysed by conducting pseudo-first order kinetics in Figure 4.12. Since most of the photocatalytic degradation of organic pollutants using semiconductors nanoparticles follows Langmuir-Hinshelwood kinetics [295, 296, 297]. The Langmuir-Hinshelwood mechanism at lower concentration was used to express the photocatalytic reaction on the surface of ZnO and TiO_2 nanoparticles, the equation is as follows:

$$\ln\left(\frac{C_o}{C_t}\right) = kt \qquad (4)$$

Where C_0 and C_t represents the concentration of methylene blue before degradation (C_0) and at different times during photocatalytic degradation (C_t) respectively. K is the pseudo first order rate constant. Figure 4.12 describes the linear relationship of ln (C_o/C_t) versus irradiation time for methylene blue. The kinetics in this section were studied using only the time variable.

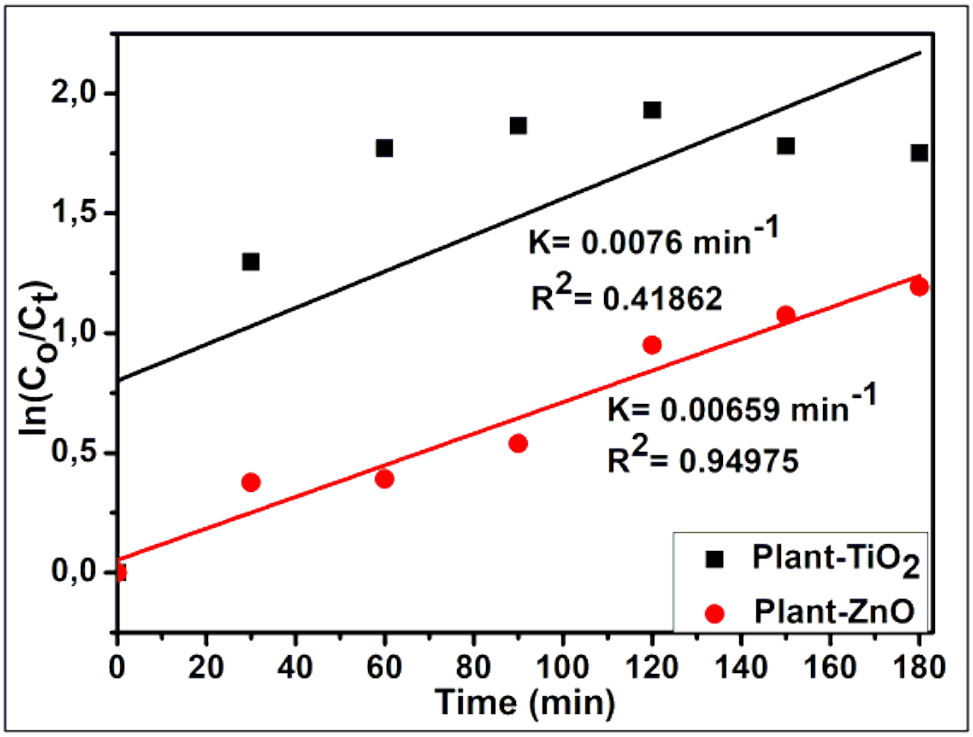

Figure 4.12: Study of 1st order kinetics of ZnO and TiO_2 nanoparticles.

The plot of $\ln(C_o/C_t)$ vs t assisted in determining the reaction constant from the slope as 0.00659 min^{-1} for ZnO nanoparticles. Also, the R^2 value indicated a slightly good correlation to the pseudo first order reaction kinetics found as 0.94975 min^{-1}, though 0.99 is more preffered. This suggests that the photocatalytic degradation of MB by ZnO nanoparticles fits Langmuir-Hinshelwood kinetic model. The first order reaction rate constant for TiO_2 nanoparticles was found to be 0.0076 min^{-1} with R^2 value of 0.41862. The R^2 value did not indicate a good correlation of Langmuir-Hinshelwood kinetic model. This observation could be due to the multiple processes taking place during photocatalytic degradation. The degradation can take place in methylene blue solution or at the surface of the photocatalysts with the adsorbed methylene blue.

4.6.6. Reusability of photocatalyst

The reusability evaluation of the photocatalyst is important because it can decrease the production cost of nanomaterials. ZnO and TiO_2 photocatalyst were tested for the degradation of methylene blue, both photocatalysts showed photoactivity. Therefore, their reusability efficiency was put into test. The experiments were conducted under

optimized conditions over 4 cycles. After completion of photocatalytic reaction, the photocatalysts were recovered by filtration and washed with ethanol to remove organic molecules absorbed on the surface. The same procedure was followed after every completed cycle.

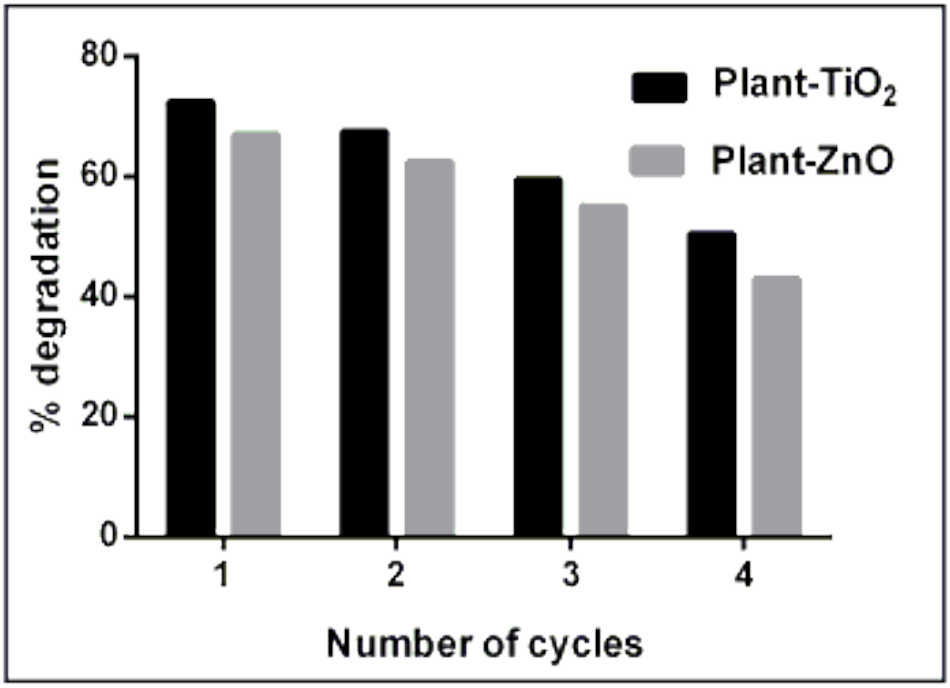

Figure 4.13: Reusability of TiO_2 and ZnO nanoparticles.

Figure 4.13 represents the reusability in 4 successive cycles. As shown in the Figure, photocatalytic degradation percentage decreased from cycle 1 onwards for both nanoparticles. This indicates that these photocatalysts lost their photocatalytic efficiency immediately. These could be attributed to, the partial loss of photocatalyst during recovering step and the blockage of active sites. Also, the active sites blocked by the organic molecules adsorbed on the photocatalyst surface which could not be removed during washing step [298]. This led to less active sites available to accommodate more of the methylene blue. To further test the ability of these photocatalysts against other pollutants, their antibacterial activity was tested.

4.7. Antibacterial activity of ZnO and TiO_2 against model pollutants

Green synthesised TiO_2 and ZnO nanoparticles were tested for their antibacterial activity against the following strains (two gram negative [-] and two gram positive [+]) *E. coli* [-], *S. aureus* [+], *E. faecalis* [+] and *P. aeruginosa* [-].

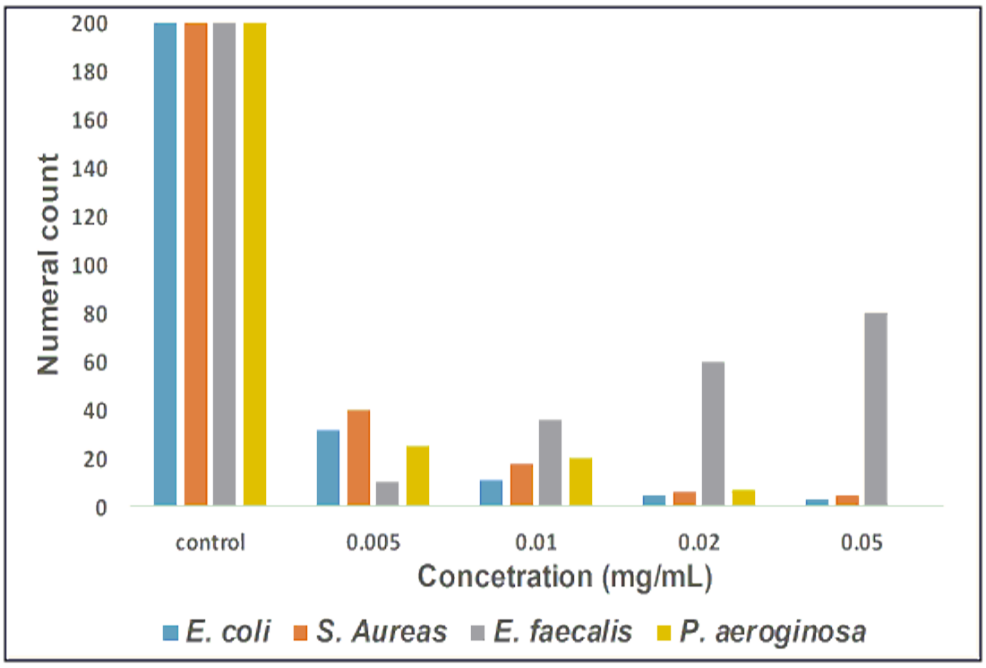

Figure 4.14: Antibacterial activity of ZnO nanoparticles.

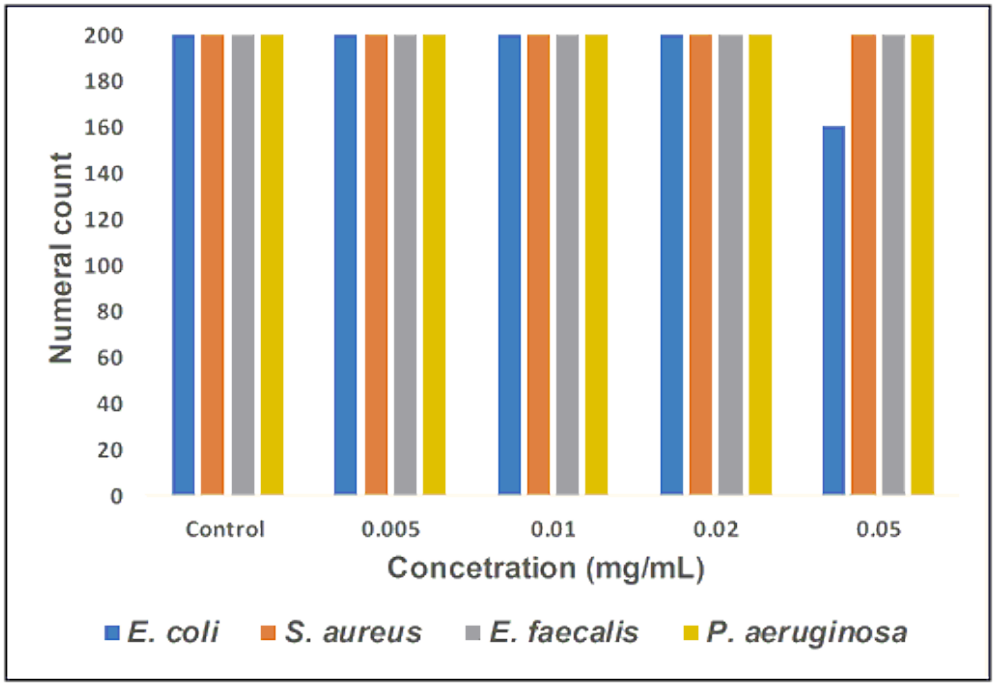

Figure 4.15: Antibacterial activity of TiO_2 nanoparticles.

The antibacterial activity of green synthesised ZnO and TiO_2 nanoparticles was conducted by varying the concentration of the nanoparticles. From Figure 4.15, it shows that green synthesised TiO_2 nanoparticles were inactive against a majority of these model strains. At a higher concentration of 0.05 mg/mL, the nanoparticles were active against *E. coli* strain. For the two-gram positive bacterial strains, TiO_2 nanoparticles were inactive, which might be due to the thick layer of these strains. Gram negative strains generally have a thin cell wall, but the nanoparticles could not cover the cell wall or absorption towards bacteria surface was insufficient to restrict the bacteria from growing. This trend had been observed by Ashajyoti [299] as well, where nanoparticle treatments were found to have selective activity between the gram negative and gram-positive strains. For ZnO nanoparticles though, we suspect the enhanced bactericidal effect against all the strains could be due to the functionalised ZnO nanoparticles, also consisting of Reactive Oxygen Species (ROS). As stated before, nanoscale materials tend to undergo an electrostatic interaction with bacterial strain and due to this, the reactive oxygen species will be generated thus destroying the bacterial cells. Additionally, factors such as particles size and morphology also play a role in determining the antibacterial potential of a material. It has been shown that when the nanoparticle sizes decrease, the microbial interaction between the cell membrane and the Zn^{2+} released from the ZnO nanoparticle becomes strong, thus increasing the antibacterial activity. In this study, the dominance of the smaller particle sizes from ZnO nanoparticles that have been derived from plants, played a role. However, in the case of TiO_2 nanoparticles, it did not inhibit the growth of most of these strains even though it is smaller in size than ZnO nanoparticles which could be due to insufficient biological active groups on the surface. ZnO nanoparticles appears to be more active across all the bacteria strains than TiO_2 nanoparticles. This could be related to the surface of the green synthesised ZnO nanoparticles that has other elements C, N, H and O which can contribute to the inhibition of bacteria. This implies that in this batch modelled bacteria pollutant experiment, the size of the nanoparticles did not play much of a role. However, TiO_2 nanoparticles did show promising activity against gram negative bacteria strains (Figure 4.15. active against *E. coli*), labelling the material as a potential antibacterial agent in real water samples.

4.8. Analysis and treatment of various water samples for microorganisms

Water pollution caused by microorganisms are a concern throughout the world because of the diseases associated with them. Antibacterial agents are developed to address the standard quality of water for living organisms. This section gives an analysis of the water samples collected from four various reservoirs or sources. Water from tap, sewage, pond and river were tested for the presence of population of bacteria strains, total coliform, *Enterobacteriaceae* and *E. coli*.

Table 4.2 Analysis of water samples using tempo reader.

Microorganisms	**Tap**	**Sewage**	**Pond**	**River**
Aerobic count	>490000	>490000	>490000	>490000
Total coliform	360	710	490	250
Enterobacteriaceae	5700	1500	160000	1200
E. coli	0	50	10	0

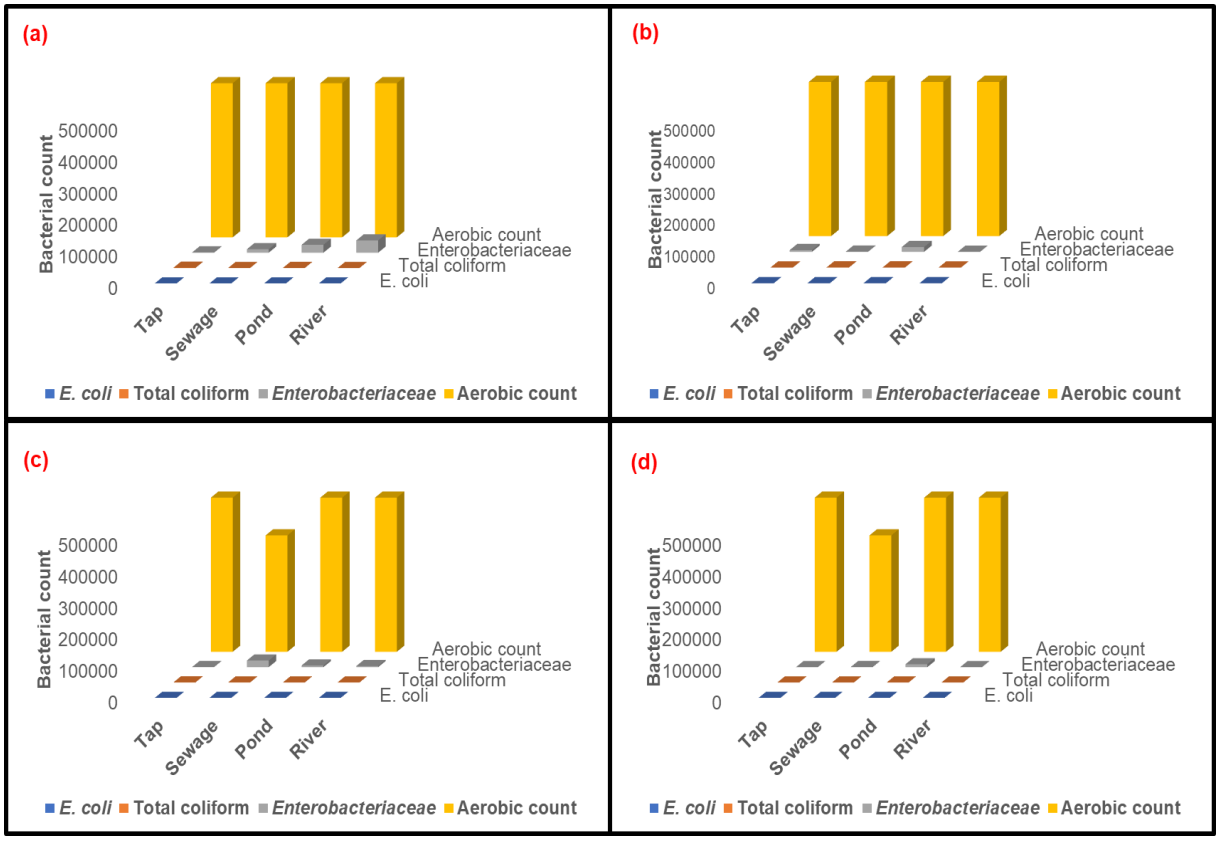

Figure 4.16: a) ZnO and b) TiO_2 nanoparticles treatment at a concentration of 0.005mg/ml as well as using c) ZnO and d) TiO_2 0.05 mg/ml treatment.

Their presence was estimated by a tempo reader as follows, population of bacteria were greater than 490000 colonies in all water samples, sewage water had a higher number of coliform bacteria, pond had more of *Enterobacteriaceae* bacteria and whereas tap and river had no existence of *E. coli*. However, in sewage and pond, *E. coli* was minimal. All microorganisms detected could have resulted from the distribution channels of water, faeces from humans or animals and runoff water from agricultural activities [81]. In providing an alternative solution, treatment of water samples was conducted using ZnO and TiO_2 nanoparticles. Figure 4.16 (a-d) presents the treatment at various nanoparticle concentrations, 0,005 mg/mL and 0.05 mg/mL, respectively. The nanoparticles inhibited all the *E. coli* colonies in sewage and pond water. *Enterobacteriaceae* was reduced to 950 and 25000 in tap and pond by ZnO nanoparticles. ZnO nanoparticles further inhibited the growth of some of the coliform colonies in sewage (260) and river (30) samples. Total coliform in tap and river water samples proliferated with treatment at lower and higher concentration, respectively. These were also noted with *Enterobacteriaceae* strains in sewage sample for both concentrations and also in river sample at a higher concentration (0.05 mg/mL). This could be due to the phytochemical's functional groups or minerals such as Ca and Na, present on the surface of ZnO nanoparticles. The bacteria fed on them promoting proliferation of bacterial cells. In addition, strains such as *Salmonella enterica* have been reported to overcome sequestration of zinc. The bacteria exist in human and animal organism intestines that is released through faeces [300]. Zn could be a tolerant metal towards other strains related to *Salmonella* in the water samples, leading to an increase in number of strains in sewage, tap and river water samples. TiO_2 nanoparticles significantly supressed the survival or spreading of bacteria in all water samples for both concentrations. This could be attributed to narrow and small size distribution of TiO_2 nanoparticles and some functional groups available on the surface. In addition, it could imply that the adsorption of TiO_2 nanoparticles towards bacteria surface was effective, leading to inactivity of bacteria. In these water samples, TiO_2 nanoparticles was a prominent material against all tested microorganisms than ZnO nanoparticles.

4.9. Conclusion

LC-MS showed tannin, flavonoids and phenol as compounds that were present in *Monsonia burkeana* water extract, further correlated with FTIR for functional groups such as OH, C−H, C═O, C−O and C═C. The synthesise of TiO_2 and ZnO nanoparticles was achieved by the green chemistry approach using *Monsonia burkeana* plant extract. The materials were confirmed by XRD, UV-vis and FTIR. XRD patterns, Figure 4.5a showed a wurtzite structure of ZnO nanoparticles and Figure 4.5b showed anatase phase of TiO_2 nanoparticles. The crystalline size was estimated as 8.3 nm and 18.6 nm using the Scherer equation falling within the range determined from TEM. The TEM images showed that TiO_2 and ZnO nanoparticles had a dominating size between 5 to 10 nm and 10 to 20 nm, respectively. SEM revealed that TiO_2 had a spherical shape whereas ZnO had a hexagonal shape. The photocatalytic activity at optimum conditions were established. ZnO and TiO_2 photocatalyst have been tested in degradation of methylene blue, both photocatalyst were shown to be efficient. However, TiO_2 nanoparticles was observed to be more efficient than ZnO nanoparticles. The results show that the green synthesis route using *Monsonia burkeana* extract had enhanced the antibacterial activity of the ZnO nanoparticles. In Section 4.7, TiO_2 was reported to be active against *E. coli* for batch modelled pollutants. This could imply that TiO_2 nanoparticles are more active against gram negative bacterial strains. Hence, in water samples it was more potent against *Enterobacteriaceae* strains. Since they have a thin cell wall, small sized materials with some biomolecules on the surface could penetrate easily to distract the bacteria strain.

Chapter 5

Synthesis of carbon based materials decorated with green synthesised TiO_2 nanoparticles

---

5. Introduction

Although, chapter 4 illustrated TiO_2 as a prominent photocatalyst compared to ZnO nanoparticles. However, TiO_2 nanoparticles still needed to be improved for its photocatalytic activity. This chapter explores the deposition of TiO_2 nanoparticles on the carbon nanofibers (CNFs) and carbon sphere (CSs). The CNFs and CSs were used as supporting materials in the formation of a photocatalyst composite with TiO_2 nanoparticles. CSs has an sp^2 hybridization of the carbon-carbon bonds with a cylindrical spherical form of graphene whereas CNFs are a tubular form of graphene [246, 173]. They have been used as catalysts support for the metals or metal oxides due to their high surface area, diverse morphologies and synergic effect [222]. Hence, they are beneficial as supports to the photocatalyst in photocatalytic degradation of organic dyes. In addition, a low band gap material CuO was also loaded, to check if the recombination rate will be reduced, thus improving the photocatalytic degradation of the dye. In the present effort, the green derived CuO/TiO_2 nanoparticles deposited on the carbon based materials were tested for their photocatalytic activity against MB dye. The samples prepared in this chapter are presented in Table 5.1.

Table 5.1 List of the composite's samples.

Samples no	Name
1	Carbon spheres (CSs)
2	Carbon nanofibers (CNFs)
3	5%-TiO_2/CSs
4	10%-TiO_2/CSs
5	20%-TiO_2/CSs
6	5%-TiO_2/CNFs
7	10%-TiO_2/CNFs
8	20%-TiO_2/CNFs
9	2%-CuO/TiO_2/CSs
10	6%-CuO/TiO_2/CSs
11	10%-CuO/TiO_2/CSs
12	2%-CuO/TiO_2/CNFs
13	6%-CuO/TiO_2/CNFs
14	10%-CuO/TiO_2/CNFs

5.1. Morphological analysis

The morphological analysis of binary composites (TiO_2/CSs and TiO_2/CNFs) and ternary composites (CuO/TiO_2/CSs and CuO/TiO_2/CNFs) synthesised using *Monsonia burkeana* water extract as a medium of reaction were examined by SEM. The composite samples were compared with each other and TiO_2 analysed in chapter 4. Figure 4.5b showed a spherical shape and a smooth surface of TiO_2 nanoparticles. Figure 5.1 and Figure 5.2 shows the morphologies of the synthesised composite samples.

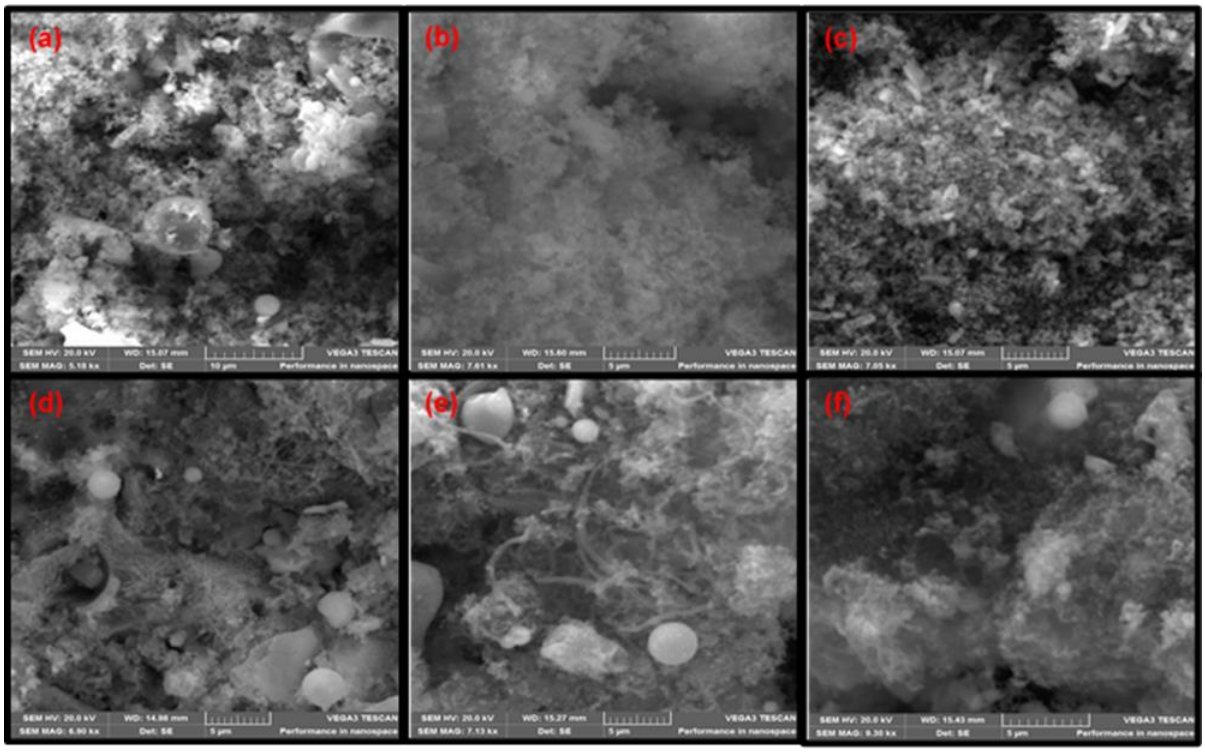

Figure 5.1: SEM images of (a) 5%-TiO_2/CSs (b) 10%-TiO_2/CSs (c) 20%-TiO_2/CSs (d) 5%-TiO_2/CNFs (e) 10%-TiO_2/CNFs (f) 20%-TiO_2/CNFs.

Figure 5.1a representing 5%-TiO_2/CSs consists of a spherical shaped material. Figure 5.1(b, c) representing 10% and 20%-TiO_2/CSs, shows a rough surface which could be due to spherically shaped TiO_2 and CSs overshadowing each other. In the TiO_2/CNFs composite samples (Fig 5.1(d-f)) spherically shaped materials and fibers were observed. Since the fibers were made from coal fly ash which consists of various other elements which are spherical in nature, it shows that the material was not fully converted to fibers and that there was still some unburnt ash, hence the dominanat spherical shape. Figure S3(a-f) shows the elemental composition of all binary composite samples. The titanium (Ti), oxygen (O) and carbon (C) presence were validated in all the materials. The EDS spectrum of TiO_2/CSs composite samples showed elemental peaks of silicon (Si), potassium (K), phosphorus (P), aluminium (Al), sulfur (S) and calcium (Ca) were identified. Moreover, the 5%-TiO_2/CSs and 10%-TiO_2/CSs samples had elements such as sodium (Na), magnesium (Mg), iron (Fe) and chlorine (Cl) which were also identified. These additional elemental peaks could be from the *Monsonia burkeana* water extract moieties absorbed on the surface of the TiO_2/CSs. Also, they could be from the unburnt coal fly ash, as this Duvha ash had

been shown in previous studies to consists some of these elements [260]. Some of these elements were also identified in TiO_2/CNFs samples. However, the EDS of 10%-TiO_2/CNFs and 20%-TiO_2/CNFs showed fewer elements were absorbed from *Monsonia burkeana* moieties.

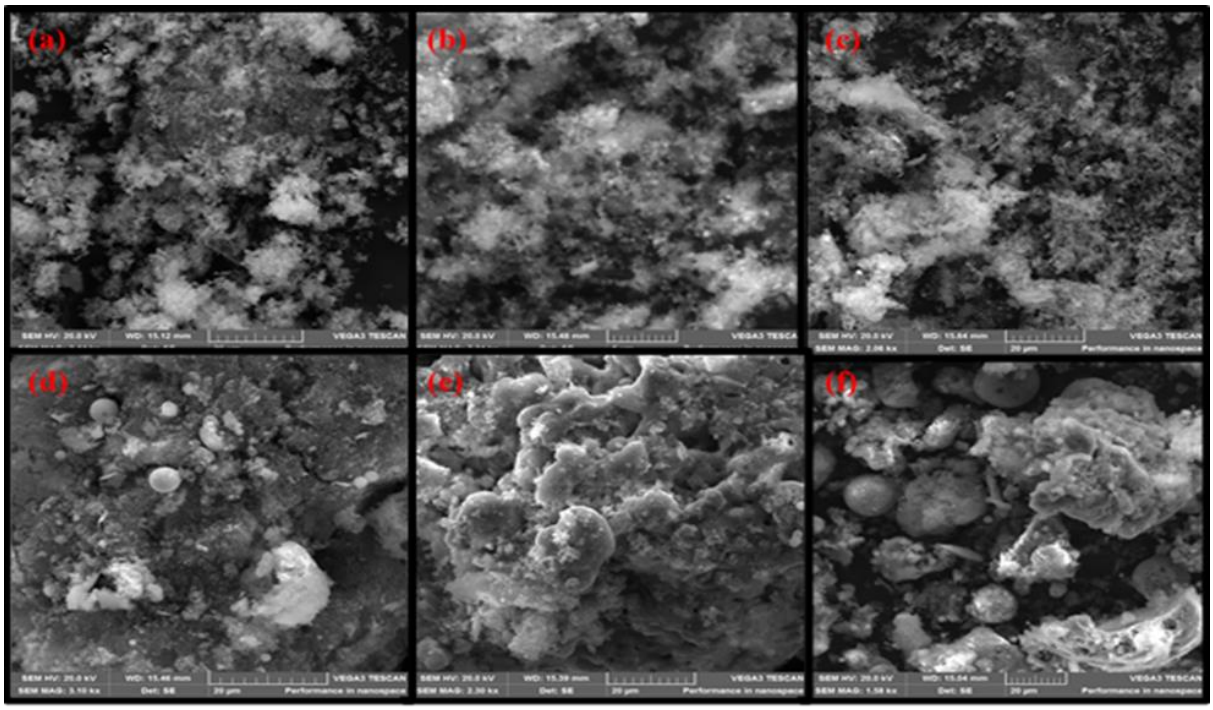

Figure 5.2: SEM images of (a) 2%-CuO/TiO_2/CSs (b) 6%-CuO/TiO_2/CSs (c) 10%-CuO/TiO_2/CSs (d) 2%-CuO/TiO_2/CNFs e) 6%-CuO/TiO_2/CNFs and f) 10%-CuO/TiO_2/CNFs.

Figure 5.2 displays the SEM images of ternary composite samples of 2%-CuO/TiO_2/CSs, 6%-CuO/TiO_2/CSs, 10%-CuO/TiO_2/CSs, 2%-CuO/TiO_2/CNFs, 6%-CuO/TiO_2/CNFs and 10%-CuO/TiO_2/CNFs. The addition of CuO on the TiO_2/CSs and TiO_2/CNFs composites did not change the morphology of the composites. This could be due to the minimal loading on the composites, thus the effect was not observed. Instead, more spherically agglomerated material was observed. Figure S4(a-f) validated the presence of elements from TiO_2/CSs and TiO_2/CNFs in CuO/TiO_2/CSs and CuO/TiO_2/CNFs composites samples. In addition, the EDS spectrum shows a copper peak in all composite samples. It confirms that CuO was successfully incorporated.

5.2. Spectroscopic analysis

The crystal phase composition in the binary composites (TiO_2/CSs and TiO_2/CNFs) and ternary composites (CuO/TiO_2/CSs and CuO/TiO_2/CNFs) were traced by XRD analysis. Binary composites crystal phases are indicated in Figure 5.3(a, b), whereas with the ternary composites, the main crystal features to be traced are CuO as indicated in Figure 5.3(c, d). In the ternary composites, the TiO_2 anatase planes are assigned with an A whereas rutile phase assigned R. In all composites the doted lines indicate the crystal phases that were identified.

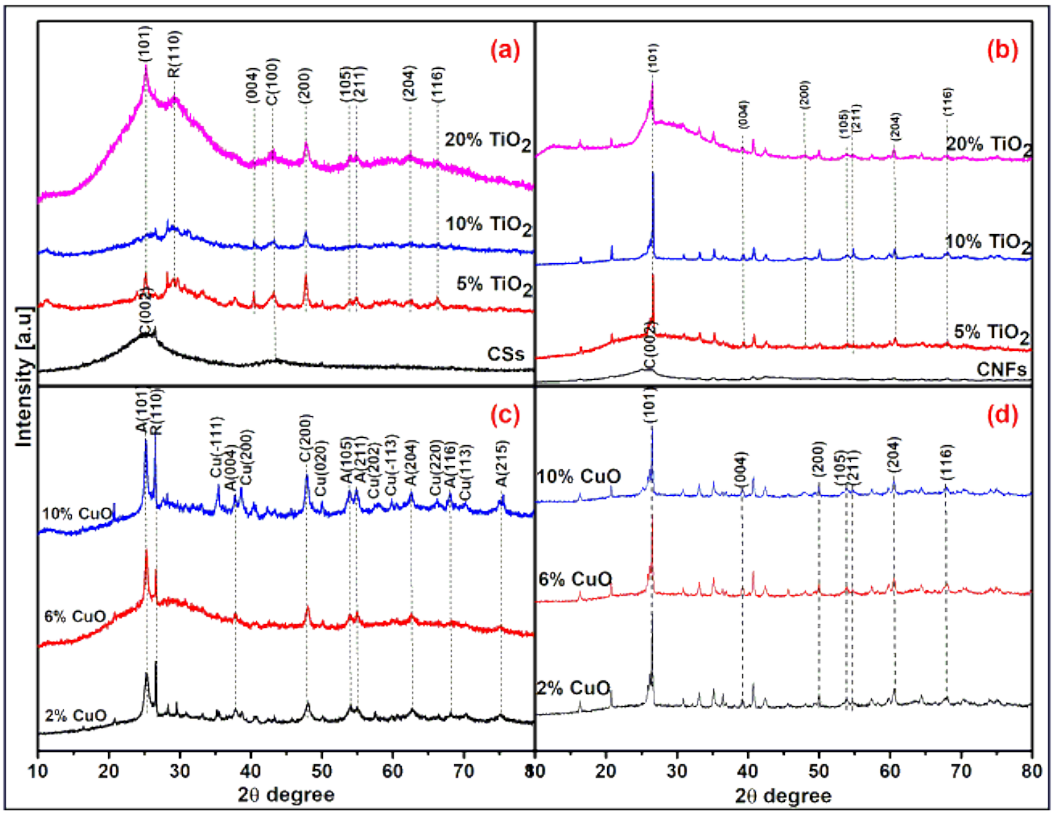

Figure 5.3: XRD of (a) TiO_2/CSs, (b) TiO_2/CNFs, (c) CuO/20-TiO_2/CSs and (d) CuO/20-TiO_2/CNFs.

In Figure 5.3(a, b), a typical x-ray pattern labelled CSs and CNFs shows an amorphous carbon peak corresponding to (002) at around 25.3° and CSs shows another peak corresponding to (100) at around 40.1°. The peaks of TiO_2 corresponding to planes (101), (004), (200), (105), (211), (204) and (116) at around the following diffraction angles 25.3, 37.6, 47.9, 53.9, 54,1, 62.4 and 68.3° are visible in both CSs and CNFs

composite. However, in the CSs composite, the rutile peak corresponding (110) is traced indicating the polymorphs mixture. The XRD pattern obtained in chapter 4 for TiO_2, anatase diffraction peak was slightly amorphous (Figure 4.6b) resulting in difficulty to differentiate with amorphous carbon in the composite. As indicated in Figure 5.3(a, b), we were able to identify the carbon peak at around 25.3°, same position with anatase phase. However, carbon has a relatively lower scattering intensity compared to TiO_2. Other possible reasons could be the overlap of the carbon peak with anatase at 25.3°. Considering the mentioned reasons, the peak was indexed to anatase TiO_2 indicated in x-ray patterns (Figure 5.3(a, b)) of 5, 10 and 20 % loading composites. In the ternary composites of 2%, 6% and 10% CuO/TiO_2/CSs (Figure 5.3c), the same peaks of TiO_2 peaks in 20% TiO_2/CSs (Figure 5.3a) were observed. In addition, CuO small peaks corresponding to planes (-111), (200), (020), (202), (-113), (220) and (113) at diffraction angles 35.3, 38.9, 50.0, 58.0, 59.9, 66.2 and 70.3° were respectively obseved. The peaks were not intense which could be due to small amounts of Cu loading precursor used to prepare the ternary composites. In a case of TiO_2 diffraction peaks, the peaks were more intense in a CuO/TiO_2/CSs composite than in 20%-TiO_2/CSs. Figure 5.3d showed the TiO_2 crystal phases with the other untraceable crystal phases which could be from coal fly ash composition. The same challenge was encountered in Figure 5.3(b). The crystal size of all the composite samples were obtained from the diffraction peak at around 25° using scherer equation designated from equation 2 in chapter 2. The crystal sizes for CSs, 5%-TiO_2/CSs, 10%-TiO_2/CSs, 20%-TiO_2/CSs, 2%-CuO/TiO_2/CSs, 6%-CuO/TiO_2/CSs and 10%-CuO/TiO_2/CSs were obtained as follows 2.32, 16.5, 3.51, 0.79, 4.09, 0.75 and 3.53 nm, respectively. For CNFs, 5%-TiO_2/CNFs, 10%-TiO_2/CNFs, 20%-TiO_2/CNFs, 2%-CuO/TiO_2/CNFs, 6%-CuO/TiO_2/CNFs and 10%-CuO/TiO_2/CNFs crystal sizes of 1.46, 0.68, 14.2, 0.75, 13.4, 13.1 and 12.0 nm, respectively were obtained. The addition of CuO decreased the crystalline size of 20%-TiO_2/CSs and 20%-TiO_2/CNFs composites. Therefore, the crystallinity of the composites increased as shown by shaper and narrow peaks.

5.2. Surface analysis

The composites formation and surface nature analysis were performed by FTIR. Figure 5.4(a, b) shows a binary composite of TiO_2/CSs and TiO_2/CNFs, respectively,

whereas Figure 5.4(c, d) shows a ternary composite of CuO/TiO_2/CSs and CuO/TiO_2/CNFs, respectively.

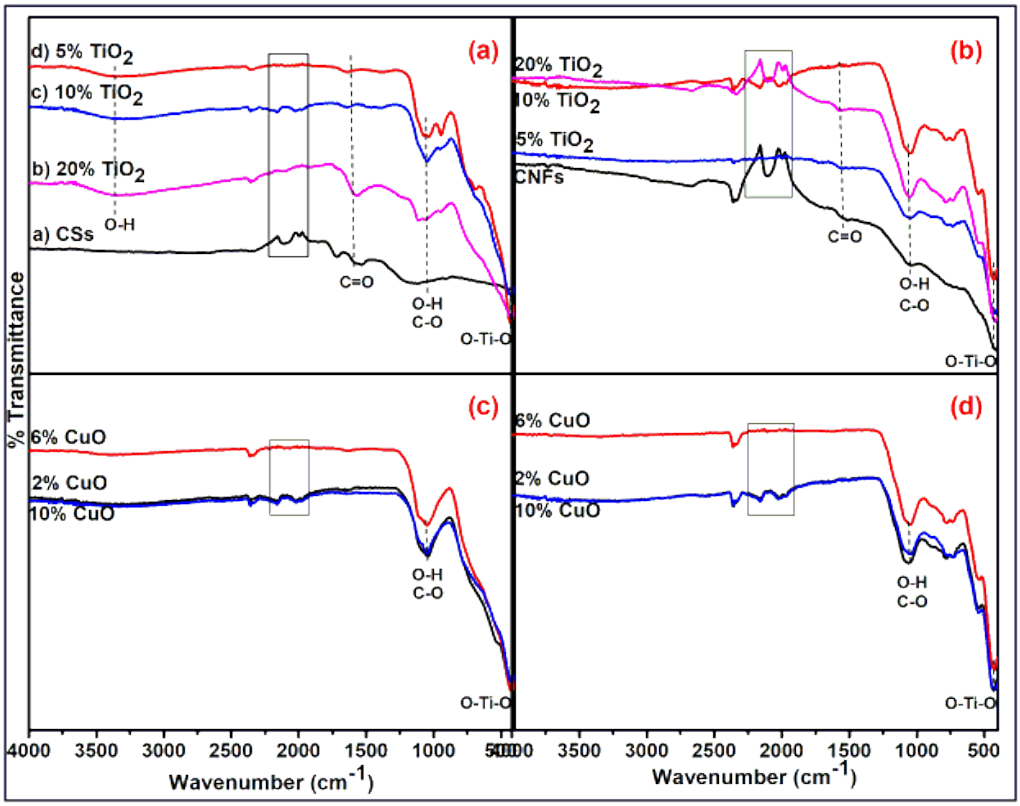

Figure 5.4: FTIR of (a) TiO_2/CSs, (b) TiO_2/CNFs, (c) CuO/TiO_2/CSs and (d) CuO/TiO_2/CNFs.

The treated CNFs and CSs show a similar vibration band of carboxylic groups (COOH) assigned at 1058 cm^{-1} and 1615 cm^{-1} in Figure 5.4(a, b) labelled CSs and CNFs. The OH group vibration from the carboxylic group, became stronger in the composite spectra, which could be due to the addition of OH from *Monsonia burkeana* or it indicates the presence of C-O from the phenols. At around 3400 cm^{-1} in Figure 5.4a, a band attributed to OH from *Monsonia burkeana* plant extract was identified. All the spectra in Figure 5.4 display a peak that can be associated with graphitic carbon [301] highlighted by the box. In all composite samples, the spectra of O-Ti-O vibration was assigned at 497 cm^{-1} confirming the presence of TiO_2 nanoparticles. However, in all the ternary composites of CuO/TiO_2 with carbon based materials there is no significant trace of CuO vibration peak in all the spectra, which could be due to the minimal

percentage of loading. The FTIR spectra had no significant change which may indicate that there is no interlink between Ti-O and carbon since it is a physically synthesised composite. These can affect negatively on the photocatalytic activity of the composites, since the photocatalytic performance of the composite depends on the synergistic effect of the materials wthin the composite.

5.3. Thermal stability analysis

Thermogravimetric analysis was conducted to evaluate thermal stability of the synthesised carbon based materials and their composites. Thermal stabilities and derivative profiles are displayed in Figure 5.5(a-h).

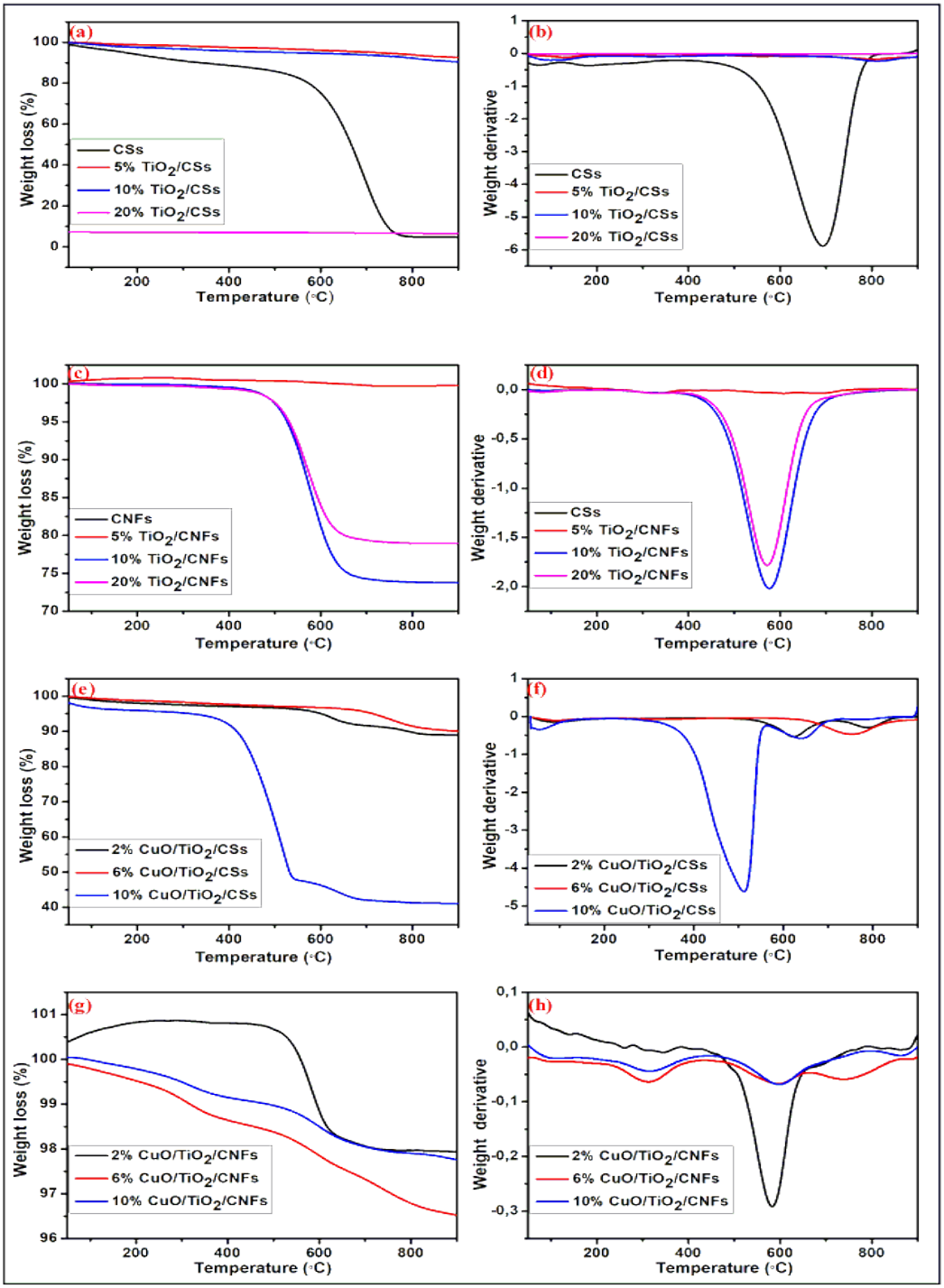

Figure 5.5: TGA and corresponding derivatives (a, b) CSs and 5%, 10%, 20% TiO_2/CSs (c, d) CNFs and 5%, 10%, 20% TiO_2/CNFs, (e, f) 2%, 6% and 10% CuO/TiO_2/CNFs and (g, h) 2%, 6% and 10% CuO/TiO_2/CSs.

In Figure 5.3a, there was a slight decomposition of carbon spheres between 100 °C and 350 °C which could be attributed to OH molecules from the washing process.

Then the second phase of decomposition at around 550 °C occurred gradually, a similar trend was observed by other studies [302, 303]. In contrast, the composites of 5%-TiO_2/CSs and 10%-TiO_2/CSs were thermally stable throughout the applied temperatures. However, 20%-TiO_2/CSs decomposed from the initial temperature with a 80% onset weight loss. This indicate that the higher amount TiO_2 affected the stability of the CS as was highlited by Pasini *et al*., [304]. In addition, this could also be attributed to the percolating network in the composite that can act as thermal conducting material. Figure 5.3b, showed a broad derivative peak indicating that the CSs have some impurities. The 5%-TiO_2/CSs, 10%-TiO_2/CSs and 20%-TiO_2/CSs composites show derivative without phases. Figure 5.3c, shows CNFs and 5%-TiO_2/CNFs were stable over a wide range of temperatures. The decomposition of 10%-TiO_2/CNFs and 20%-TiO_2/CNFs accured between 500 °C and 650 °C with weight losses of 20% and 25%, respectively. The derivative plot of CNFs and 5%-TiO_2/CNFs shows that the structure of the carbon was still intact. The derivative plots of 10%-TiO_2/CNFs and 20%-TiO_2/CNFs show that the composites are impure. The composite of 2%-CuO/TiO_2/CSs and 6%-CuO/TiO_2/CSs showed a slight decomposition at 850 °C whereas 10%-CuO/TiO_2/CSs decomposed at 400 °C, meaning that a higher CuO loading, reduced the thermal stability of the quaternary composite. The derivative peaks of 2%-CuO/TiO_2/CSs, 6%-CuO/TiO_2/CSs and 10%-CuO/TiO_2/CSs was broad, meaning that there could be some impurities and indicating some form of amorphificity [305]. In Figure 5.5g, an onset of decomposition of 6%-CuO/TiO_2/CNFs and 10%-CuO/TiO_2/CNFs was observed at 100 °C whereas 2%-CuO/TiO_2/CNFs decomposed at 500 °C. Their derivative peaks were broad showing that the composite is impure. The broad derivatives peaks could be due to the elements absorbed on the surface of the composites as indicated in Figure S3 and S4.

5.4. Photocatalytic activity of binary and ternary composites.

The photocatalytic activity of the composites was evaluated using the optimum conditions obtained from chapter 4 for plant TiO_2. Figure 5.6 presents the photocatalytic degradation performance of composites with respect to time, over 3 hrs. The methylene blue (MB) with the nanocomposite photocatalysts was allowed to reach an adsorption-desorption equilibrium over 60 min in the dark as indicated by 0 min on the plot.

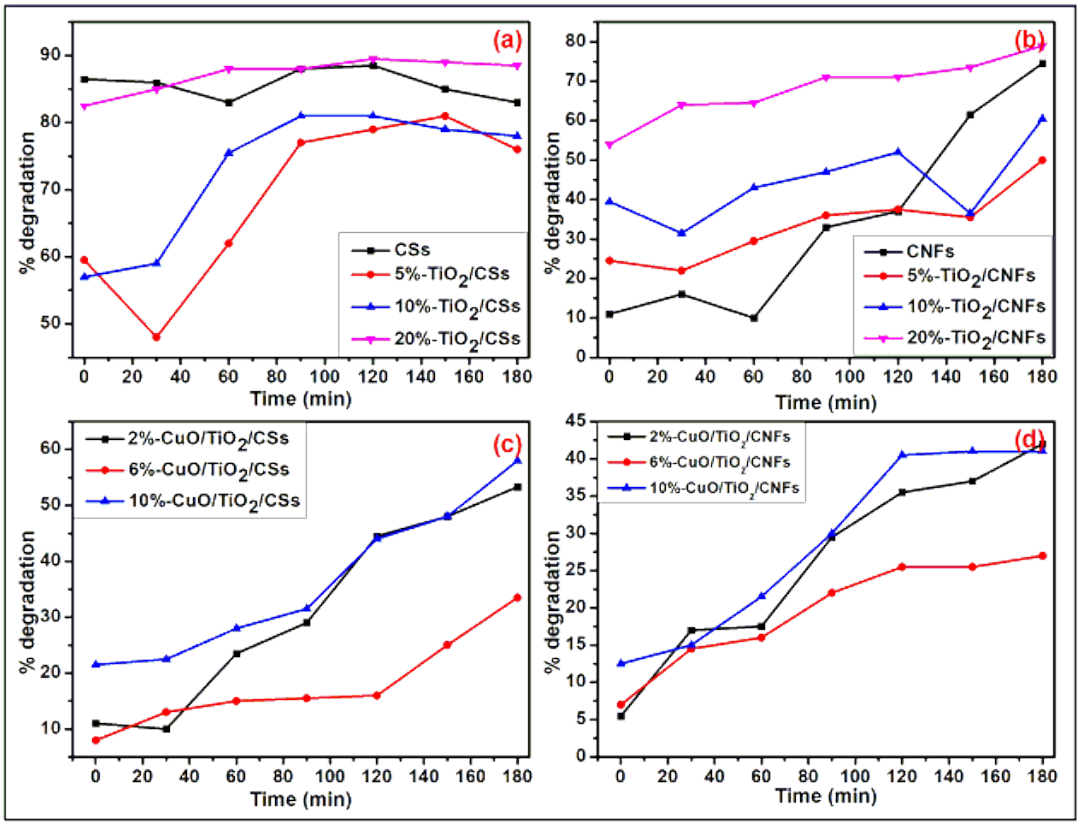

Figure 5.6: Photocatalytic activity of (a) TiO_2/CSs, (b) TiO_2/CNFs, (c) CuO/TiO_2/CSs and (d) CuO/TiO_2/CNFs.

In Figure 5.6(a, b), the percentage degradation is fluctuating with time due to desorption-absorption of methylene blue on the surface. In this section, various loading percentages of 5, 10 and 20 % of TiO_2 on CSs and CNFs, respectively, were investigated (Fig 5.6(a, b)). From this analysis, the 20%-TiO_2/CSs had a higher percentage of degradation with an 89.5% degradation of MB pollutant. Furthermore, it improved the TiO_2 degradation capacity by 4% at 120 min which could be due to the amorphous structure and the small particle particle size as indicated in Figure 5.1a (20%-TiO_2/CSs). The raw CSs showed a better photocatalytic activity with 88.5% than 5%-TiO_2/CSs and 10%-TiO_2/CSs which degraded 79% and 81% of MB dye, respectively. This could be attributed to the unburnt spherical materials from the ash which have a high adsorption and photocatalytic capacity. For the TiO_2/CNFs composite, 20% loading had a higher percentage of degradation of 71.0% which was significantly higher than 10% and 5% loadings that degraded 52.0% and 37.5% of MB,

respectively. Nonetheless, it did not improve the TiO_2 nanoparticles efficiency. The data plotted shows that 20%-TiO_2/carbon-based composite was more efficient compared to 5 and 10 % loadings. Therefore, 20%-TiO_2/carbon-based composite was further loaded with various percentage loadings of CuO nanoparticles. The addition of CuO nanoparticles did not improve the efficiency of the composite interms of degradation of MB for all the carbon based materials. This could be attributed to the amorphous form of carbon from the unburnt ash and the synthesis method used for the composite. The following is a representation of the decreasing order the photocatalytic efficiency in Figure 5.6(a, b) 20%-TiO_2/CSs > 10%-TiO_2/CSs > 5%-TiO_2/CSs > 20%-TiO_2/CNFs > 10%-TiO_2/CNFs > 5%-TiO_2/CNFs > CNFs rated at 120 min. In Figure 5.6(c, d) 2%-CuO/TiO_2/CSs ≥ 10%-CuO/TiO_2/CSs > 10%-CuO/TiO_2/CNFs > 2%-CuO/TiO_2/CNFs > 6%-CuO/TiO_2/CSs > 6%-CuO/TiO_2/CNFs. Overall, the composite samples lack superior photocatalytic activity compared to TiO_2 nanoparticles which could be due to gastification of carbon based materials at elevated temperature, leading to mass loss. The Langmuir-Hinshelwood kinetics, equation 4 in chapter 4 was used to construct a first-order reaction plot of the composite samples in Figure 5.7. The plot was used to calculate the R^2 and constant rate tabulated in Table 5.2. The R^2 value for the samples CSs, CNFs, 5%-TiO_2/CSs, 10%-TiO_2/CSs, 20%-TiO_2/CSs, 10%-TiO_2/CNFs, 5%-TiO_2/CNFs, 10%-CuO/TiO_2/CNFs and 6%-CuO/TiO_2/CSs indicate no good correlation with Langmuir-Hinshelwood kinetics model whereas 20%-TiO_2/CNFs, 2%-CuO/TiO_2/CSs, 2%-CuO/TiO_2/CNFs and 6%-CuO/TiO_2/CNFs show a good correlation. The photocatalytic behaviour of the composite samples was negatively affected by desorption during the degradation of MB. This could be due to the elements such such as S, P and Cl absorbed on the surface as shown in Figure S(5.1, 5.2). Impurities such as sulphate, phosphate and chloride block the active sites of nanocomposite photocatalyst leading to photocatalytic deactivation [306, 307].

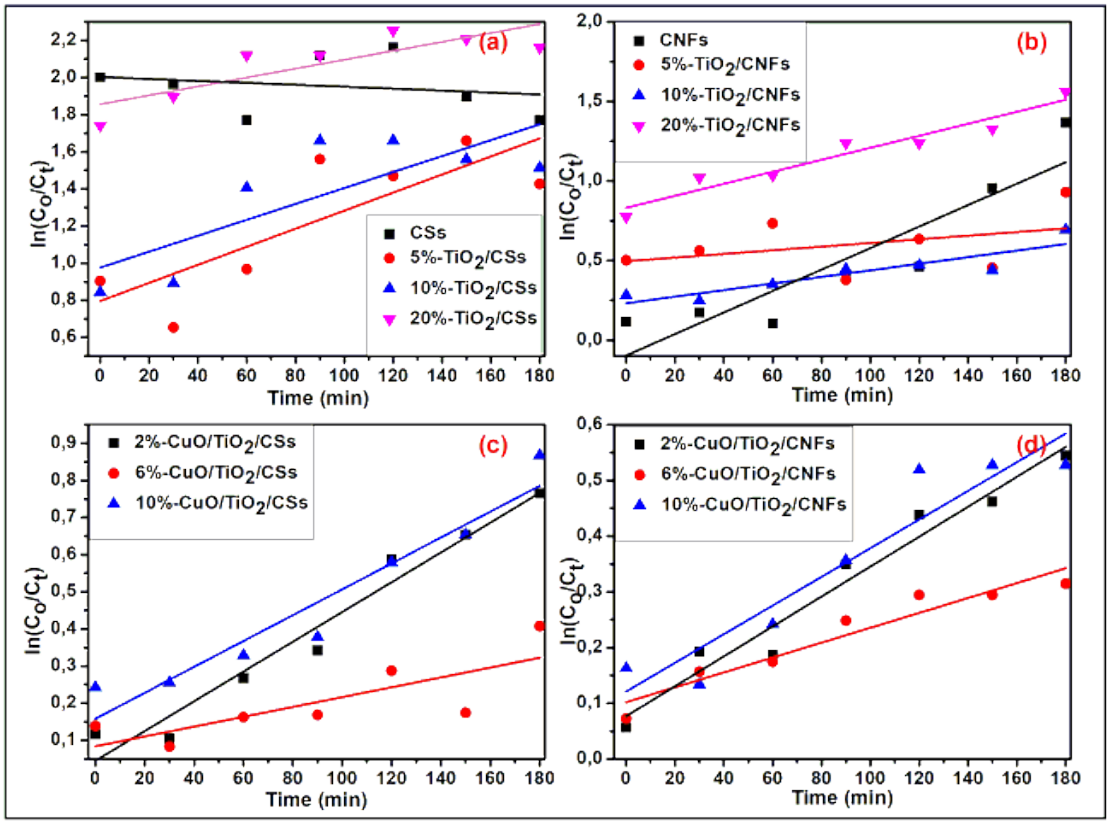

Figure 5.7: Kinetics of (a) TiO_2/CSs, (b) TiO_2/CNFs, (c) CuO/TiO_2/CSs and (d) CuO/TiO_2/CNFs.

Table 5.2 Rate constants of the various materials synthesised in this study

Catalyst	R^2	Rate constant *K* (min^{-1})
Carbon spheres (CSs)	-0.14242	-0.000522
Carbon nanofibers (CNFs)	0.79973	0.00675
5%-TiO_2/CSs	0.5965	0.00486
10%-TiO_2/CSs	0.55925	0.00429
20%-TiO_2/CSs	0.65541	0.0024
5%-TiO_2/CNFs	-0.00915	0.00115
10%-TiO_2/CNFs	0.7808	0.00207
20%-TiO_2/CNFs	0.92651	0.00377
2%-CuO/TiO_2/CSs	0.95156	0.00401

6%-CuO/TiO_2/CSs	0.54586	0.00133
10%-CuO/TiO_2/CSs	0.90992	0.00348
2%-CuO/TiO_2/CNFs	0.95326	0.00269
6%-CuO/TiO_2/CNFs	0.90897	0.00134
10%-CuO/TiO_2/CNFs	0.7928	0.00257

5.4. Conclusion

The composites of carbon based materials (CSs and CNFs) with *Monsonsia burkeana* derivative TiO_2 and CuO were prepared. The metal oxides (CuO/TiO_2) were successfully deposited on the carbon spheres and carbon nanofibers as depicted on the XRD spectra. The percentage of degradation against Methylene blue was slightly improved by 4% upon loading the 20% TiO_2 on the carbon spheres which could have been due to the interaction between the spheres and TiO_2. In ternary composites, CuO planes were observed in the composites of carbon spheres only as shown by XRD. 20%-TiO_2/CSs showed a higher photocatalytic activity at 120 minutes with 89.5% degradation of MB solution.

CHAPTER 6

Conclusion and Recommendation

The green route was successfully used to synthesise TiO_2 and ZnO nanoparticles using *Monsonia Burkeana* plant extract. In chapter 4, LC-MS and FTIR confirmed the possible compounds and functional groups in *Monsonia burkeana* extract that participated in the metal oxide formation. In addition, FTIR further confirmed the formation of metal oxides with their surface nature. It showed that the functional groups were responsible for the reduction of metal ion to form metal oxide nanoparticles. In support, UV-vis absorption spectra exhibited absorbance peaks at 325 nm and 327 nm for ZnO and TiO_2 nanoparticles, respectively. ZnO nanoparticles had mixed particle shapes depicted as spherical and hexagonal shapes obtained from the SEM image. SEM images showed spherical shape for TiO_2 nanoparticles. The TEM images showed TiO_2 and ZnO nanoparticles had a dominating size between 5 to 10 nm and 10 to 20 nm, correlating to XRD crystalline size, respectively. Moreover, XRD showed a diffraction pattern corresponding to the wurtzite structure of ZnO nanoparticles and it was crystalline, whereas the TiO_2 diffraction pattern showed an amorphous anatase peak at 27.2 ° diffraction pattern angle which could have contributed to its advantage in photocatalytic degradation of MB. The TiO_2 nanoparticles were a better photocatalyst for MB degradation than ZnO after 120 minutes. The study revealed that the antibacterial activity is controlled by various elements. In simulated water with bacteria, gram-negative strains were more sensitive against ZnO nanoparticles. However, in real water samples, ZnO nanoparticles did not give positive results. On the other hand, TiO_2 nanoparticles were only active against gram-negative *E. coli* while in real water samples provided positive results.

In terms of photocatalysis, TiO_2 was shown to be a better photocatalyst. However, as with information provided in the literature review (Chapter 2) which mentioned the disadvantages of TiO_2 nanostructures, measures we taken in an attempt to improve TiO_2 photocatalytic activity in chapter 5. The 5, 10 and 20 % of TiO_2 were loaded on carbon based materials (CSs and CNFs). Furthermore, 20%-TiO_2/carbon based materials (CSs and CNFs) were modified by loading of 2, 6 and 10 % of CuO. The formation of the composites was confirmed by XRD. XRD confirmed crystal phase

composition of TiO_2 in the composite TiO_2/CSs and TiO_2/CNFs for all the loadings. Also, confirmed that CuO were incorporated on 20%-TiO_2/CSs for all loading percentages. Except in the 20%-TiO_2/CNFs composite, we were unable to trace the CuO crystal phase. This could be due to the very low loadings of CuO, also it is worth noting that XRD is a bulk technique thus minimal loadings can be hard to trace. However, EDS in Figure S5.1 and S5.2, the Cu element was valiated in all the composites. The composites were tested for photocatalytic activity using methylene blue solution. 20%-TiO_2/CSs had a higher photocatalytic activity amongst all the loading's percentages including CuO. This implies that CuO did not the improve the degradation of MB dye. In comparison, 20%-TiO_2/CSs at 120 minutes degraded 89.5%, showing that it improved TiO_2 by 4% degradation of MB solution. Except for the 20%-TiO_2/CSs none of the composites had a better degradation than the plant TiO_2 with 85.5% degradation. The method of composite formation could have also played a role in their limited activity. Many methods such as hydrothermal and sol-gel have been employed to prepare carbon-based material composite with TiO_2. As reviewed by Bazli *et al*., [308] and Gao *et al*., [309] the resulting composites can be non-uniform, heterogenous and have mass loss. This could have contributed to the less photocatalytic degradation of the composite prepared than bare plant TiO_2 nanoparticles. The carbon based materials composite photocatalytic activity can be improved by optimizing the temperatures of calcination, since carbon experiences gasification at higher temperatures.

Since the green synthesis using the plant extract mechanism is an emerging method, the effect of variables is still underexplored. Thus, further investigation on the metal precursor concentration and concentration of *Monsonia burkeana* as well as other variables could influence on the nanoparticles yield and morphology. The green synthesis of ZnO and TiO_2 nanoparticles showed remarkable photocatalytic and antibacterial properties. These nanoparticles showed that they have a potential in the field of wastewater treatment. To provide a clear indication of photocatalytic degradation process, more analysis can be done by monitoring dye solution degraded using mass spectrometer as another technique.

CHAPTER 7

References

1. Grey, D., Garrick, D., Blackmore, D., Kelman, J., Muller, M. and Sadoff, C., 2013. Water security in one blue planet: twenty-first century policy challenges for science. *Philosophical Transactions of the Royal Society A: Mathematical, Physical and Engineering Sciences*, *371*, pp.20120406.

2. Edokpayi, J.N., Odiyo, J.O., Popoola, E.O. and Msagati, T.A., 2018. Evaluation of microbiological and physicochemical parameters of alternative source of drinking water: a case study of nzhelele river, South Africa. *The open microbiology journal*, *12*, pp.18.

3. Iijima, S., 1991. Helical microtubules of graphitic carbon. *nature*, *354*, pp.56.

4. Liu, X., Wang, M., Zhang, S. and Pan, B., 2013. Application potential of carbon nanotubes in water treatment: a review. *Journal of Environmental Sciences*, *25*, pp.1263-1280.

5. Nadeem, M., Tungmunnithum, D., Hano, C., Abbasi, B.H., Hashmi, S.S., Ahmad, W. and Zahir, A., 2018. The current trends in the green syntheses of titanium oxide nanoparticles and their applications. *Green Chemistry Letters and Reviews*, *11*, pp.492-502.

6. Elumalai, K., Velmurugan, S., Ravi, S., Kathiravan, V. and Raj, G.A., 2015. Bio-approach: Plant mediated synthesis of ZnO nanoparticles and their catalytic reduction of methylene blue and antimicrobial activity. *Advanced Powder Technology*, *26*, pp.1639-1651.

7. Ahmad, R., Mohsin, M., Ahmad, T. and Sardar, M., 2015. Alpha amylase assisted synthesis of TiO_2 nanoparticles: structural characterization and application as antibacterial agents. *Journal of hazardous materials*, *283*, pp.171-177.

8. Ovais, M., Khalil, A., Ayaz, M., Ahmad, I., Nethi, S. and Mukherjee, S., 2018. Biosynthesis of metal nanoparticles via microbial enzymes: a mechanistic approach. *International journal of molecular sciences*, *19*, pp.4100.

9. Jayaseelan, C., Rahuman, A.A., Kirthi, A.V., Marimuthu, S., Santhoshkumar, T., Bagavan, A., Gaurav, K., Karthik, L. and Rao, K.B., 2012. Novel microbial route to synthesize ZnO nanoparticles using Aeromonas hydrophila and their activity against pathogenic bacteria and fungi. *Spectrochimica Acta Part A: Molecular and Biomolecular Spectroscopy*, *90*, pp.78-84.

10. Natarajan, T.S., Natarajan, K., Bajaj, H.C. and Tayade, R.J., 2013. Study on identification of leather industry wastewater constituents and its photocatalytic treatment. *International Journal of Environmental Science and Technology*, *10*, pp.855-864.

11. Tshivhandekano, I., Ntushelo, K., Ngezimana, W., Tshikalange, T.E. and Mudau, F.N., 2014. Chemical compositions and antimicrobial activities of Athrixia phylicoides DC.(bush tea), Monsonia burkeana (special tea) and synergistic effects of both combined herbal teas. *Asian Pacific journal of tropical medicine*, *7*, pp.448-453.

12. He, L.Y., Liu, Y.S., Su, H.C., Zhao, J.L., Liu, S.S., Chen, J., Liu, W.R. and Ying, G.G., 2014. Dissemination of antibiotic resistance genes in representative broiler feedlots environments: identification of indicator ARGs and correlations with environmental variables. *Environmental science & technology*, *48*, pp.13120-13129.

13. Scott, T.M., Rose, J.B., Jenkins, T.M., Farrah, S.R. and Lukasik, J., 2002. Microbial source tracking: current methodology and future directions. *Applied and environmental microbiology*, *68*, pp.5796-5803.

14. Rawat, D., Mishra, V. and Sharma, R.S., 2016. Detoxification of azo dyes in the context of environmental processes. *Chemosphere*, *155*, pp.591-605.

15. Li, W., Mu, B. and Yang, Y., 2019. Feasibility of industrial-scale treatment of dye wastewater via bio-adsorption technology. *Bioresource technology*, *277*, pp.157-170.

17. Natarajan, S., Bajaj, H.C. and Tayade, R.J., 2018. Recent advances based on the synergetic effect of adsorption for removal of dyes from waste water using photocatalytic process. *Journal of Environmental Sciences*, *65*, pp.201-222.

18. Määttänen, M., Asikainen, S., Kamppuri, T., Ilen, E., Niinimäki, K., Tanttu, M. and Harlin, A., 2019. Colour management in circular economy: decolourization of cotton waste. *Research Journal of Textile and Apparel*. 23, pp.134-152.

19. World Health Organization, 2011. Guidelines for Drinking-water Quality. *World Health Organization, 4,* pp.19-257.

20. Ahmad, A., Rafatullah, M., Sulaiman, O., Ibrahim, M.H. and Hashim, R., 2009. Scavenging behaviour of meranti sawdust in the removal of methylene blue from aqueous solution. *Journal of hazardous materials*, *170*, pp.357-365.

21. Edokpayi, J.N., Rogawski, E.T., Kahler, D.M., Hill, C.L., Reynolds, C., Nyathi, E., Smith, J.A., Odiyo, J.O., Samie, A., Bessong, P. and Dillingham, R., 2018. Challenges to sustainable safe drinking water: a case study of water quality and use across seasons in rural communities in Limpopo province, South Africa. *Water*, *10*, p.159.

22. Holmes, S. Department of Water Affairs and Forestry. Field Guide. CSIR Environmental Services. 1996. South African Water Quality Guidelines *8*, pp. 226-243.

23. Moropeng, R.C., Budeli, P., Mpenyana-Monyatsi, L. and Momba, M.N.B., 2018. Dramatic reduction in diarrhoeal diseases through implementation of cost-effective household drinking water treatment systems in Makwane Village, Limpopo Province, South Africa. *International journal of environmental research and public health*, *15*, pp.410.

24. Lee, K.M., Lai, C.W., Ngai, K.S. and Juan, J.C., 2016. Recent developments of zinc oxide based photocatalyst in water treatment technology: a review. *Water research*, *88*, pp.428-448.

25. Matafonova, G. and Batoev, V., 2018. Recent advances in application of UV light-emitting diodes for degrading organic pollutants in water through advanced oxidation processes: A review. *Water research*, *132*, pp.177-189.

26. Ahmad, D., Sohail, M., Hussain, F., Siddiqui, H. and Yasir, M., 2019. Synthesis of Cuprous Oxide Nano Cubes and Platelets Using Both Electrodes of Copper. *Mehran University Research Journal of Engineering and Technology*, *38*, pp.415-420.

27. Huang, L., Peng, F., Yu, H. and Wang, H., 2009. Preparation of cuprous oxides with different sizes and their behaviors of adsorption, visible-light driven photocatalysis and photocorrosion. *Solid State Sciences*, *11*, pp.129-138.

28. Honarmand, M., Golmohammadi, M. and Naeimi, A., 2019. Biosynthesis of tin oxide (SnO_2) nanoparticles using jujube fruit for photocatalytic degradation of organic dyes. *Advanced Powder Technology*, *30*, pp.1551-1557.

29. Vidya, C., Prabha, M.C. and Raj, M.A., 2016. Green mediated synthesis of zinc oxide nanoparticles for the photocatalytic degradation of Rose Bengal dye. *Environmental Nanotechnology, Monitoring & Management*, *6*, pp.134-138.

30. Arabi, N., Kianvash, A., Hajalilou, A., Abouzari-Lotf, E. and Abbasi-Chianeh, V., 2018. A facile and green synthetic approach toward fabrication of *Alcea-and Thyme-stabilized TiO_2 nanoparticles for photocatalytic applications. Arabian Journal of Chemistry*, 13, pp. 2132-2141.

31. Suresh, D., Nethravathi, P.C., Rajanaika, H., Nagabhushana, H. and Sharma, S.C., 2015. Green synthesis of multifunctional zinc oxide (ZnO) nanoparticles using *Cassia fistula* plant extract and their photodegradative, antioxidant and antibacterial activities. *Materials Science in Semiconductor Processing*, *31*, pp.446-454.

32. Peighambardoust, N.S., Asl, S.K., Mohammadpour, R. and Asl, S.K., 2018. Band-gap narrowing and electrochemical properties in N-doped and reduced anodic TiO_2 nanotube arrays. *Electrochimica Acta*, *270*, pp.245-255.

33. Chin, S., Park, E., Kim, M. and Jurng, J., 2010. Photocatalytic degradation of methylene blue with TiO_2 nanoparticles prepared by a thermal decomposition process. *Powder Technology*, *201*, pp.171-176.

34. Zhu, L., Li, H., Liu, Z., Xia, P., Xie, Y. and Xiong, D., 2018. Synthesis of the 0D/3D CuO/ZnO heterojunction with enhanced photocatalytic activity. *The Journal of Physical Chemistry C*, *122*, pp.9531-9539.

35. Mamphiswana, N.D., Mashela, P.W. and Mdee, L.K., 2010. Distribution of total phenolics and antioxidant activity in fruit, leaf, stem and root of *Monsonia burkeana. African Journal of Agricultural Research*, *5*, pp.2570-2575.

36. Mamphiswana, N.D., Mashela, P.W. and Mdee, L.K., 2011. Accumulative capabilities of essential nutrient elements in organs *of Monsonia burkeana*. *African Journal of Biotechnology*, *10*, pp.16833-16848.

37. Mathivha, L.P., Thibane, V.S. and Mudau, F.N., 2019. Anti-diabetic and anti-proliferative activities of herbal teas, *Athrixia phylicoides DC* and *Monsonia burkeana* Planch. ex Harv, indigenous to South Africa. *British Food Journal*, *121*, pp.964-974.

38. Yadav, R., Kumar, V., Saxena, V., Singh, P. and Singh, V.K., 2019. Two-step synthesis of reduced graphene oxide with columnar-shaped ZnO composites and their photocatalytic performance with natural dye. *Journal of the Australian Ceramic Society*, *55*, pp.837-848.

39. Cendrowski, K., Jedrzejczak, M., Peruzynska, M., Dybus, A., Drozdzik, M. and Mijowska, E., 2014. Preliminary study towards photoactivity enhancement using a biocompatible titanium dioxide/carbon nanotubes composite. *Journal of Alloys and Compounds*, *605*, pp.173-178.

40. Coville, N.J., Mhlanga, S.D., Nxumalo, E.N. and Shaikjee, A., 2011. A review of shaped carbon nanomaterials. *South African Journal of Science*, *107*, pp.01-15.

41. Basak, T., Basak, T. and Shukla, A., 2018. Electron correlation effects and two-photon absorption in diamond-shaped graphene quantum dots. *Physical Review B*, *98*, pp.035401.

42. Liu, Y., He, L., Mustapha, A., Li, H., Hu, Z.Q. and Lin, M., 2009. Antibacterial activities of zinc oxide nanoparticles against Escherichia coli O157: H7. *Journal of applied microbiology*, *107*, pp.1193-1201.

43. Olaniran, A.O. and Igbinosa, E.O., 2011. Chlorophenols and other related derivatives of environmental concern: properties, distribution and microbial degradation processes. *Chemosphere*, *83*, pp.1297-1306.

44. Murcia, J.J., Hernández-Laverde, M., Rojas, H., Muñoz, E., Navío, J.A. and Hidalgo, M.C., 2018. Study of the effectiveness of the flocculation-photocatalysis in the treatment of wastewater coming from dairy industries. *Journal of Photochemistry and Photobiology A: Chemistry*, *358*, pp.256-264.

45. Kuśmierek, K., 2016. The removal of chlorophenols from aqueous solutions using activated carbon adsorption integrated with H_2O_2 oxidation. *Reaction Kinetics, Mechanisms and Catalysis*, *119*, pp.19-34.

46. Basu, S. and Saha, S., 2019, March. Effect of synthesis method on the photocatalytic activity of TiO_2 nanoparticles. In *AIP Conference Proceedings*, *2087*, pp.020003.

47. Štrbac, D., Aggelopoulos, C.A., Štrbac, G., Dimitropoulos, M., Novaković, M., Ivetić, T. and Yannopoulos, S.N., 2018. Photocatalytic degradation of Naproxen and methylene blue: Comparison between ZnO, TiO_2 and their mixture. *Process Safety and Environmental Protection*, *113*, pp.174-183.

48. Hajipour, M.J., Fromm, K.M., Ashkarran, A.A., de Aberasturi, D.J., de Larramendi, I.R., Rojo, T., Serpooshan, V., Parak, W.J. and Mahmoudi, M., 2012. Antibacterial properties of nanoparticles. *Trends in biotechnology*, *30*, pp.499-511.

49. Yao, S., Feng, X., Lu, J., Zheng, Y., Wang, X., Volinsky, A.A. and Wang, L.N., 2018. Antibacterial activity and inflammation inhibition of ZnO nanoparticles embedded TiO_2 nanotubes. *Nanotechnology*, *29*, pp.244003.

50. Abraham, N., Rufus, A., Unni, C. and Philip, D., 2018. Dye sensitized solar cells using catalytically active CuO-ZnO nanocomposite synthesized by single step method. *Spectrochimica Acta Part A: Molecular and Biomolecular Spectroscopy*, *200*, pp.116-126.

51. Askari, M.B., Banizi, Z.T., Seifi, M., Dehaghi, S.B. and Veisi, P., 2017. Synthesis of TiO_2 nanoparticles and decorated multi-wall carbon nanotube (MWCNT) with anatase TiO_2 nanoparticles and study of optical properties and structural characterization of TiO_2/MWCNT nanocomposite. *Optik-International Journal for Light and Electron Optics*, *149*, pp.447-454.

52. Kiayi, Z., Lotfabad, T.B., Heidarinasab, A. and Shahcheraghi, F., 2019. Microbial degradation of azo dye carmoisine in aqueous medium using Saccharomyces cerevisiae ATCC 9763. *Journal of hazardous materials*, *373*, pp.608-619.

53. Cinperi, N.C., Ozturk, E., Yigit, N.O. and Kitis, M., 2019. Treatment of woolen textile wastewater using membrane bioreactor, nanofiltration and reverse osmosis for reuse in production processes. *Journal of cleaner production*, *223*, pp.837-848.

54. Gupta, K. and Khatri, O.P., 2019. Fast and efficient adsorptive removal of organic dyes and active pharmaceutical ingredient by microporous carbon: Effect of molecular size and charge. *Chemical Engineering Journal*, *378*, pp.122218.

55. Goutam, S.P., Saxena, G., Singh, V., Yadav, A.K., Bharagava, R.N. and Thapa, K.B., 2018. Green synthesis of TiO_2 nanoparticles using leaf extract of Jatropha curcas L. for photocatalytic degradation of tannery wastewater. *Chemical Engineering Journal*, *336*, pp.386-396.

56. Zhou, Y., Lu, J., Zhou, Y. and Liu, Y., 2019. Recent advances for dyes removal using novel adsorbents: A review. *Environmental Pollution*, 252, pp. 352-365.

57. Avlonitis, S.A., Poulios, I., Sotiriou, D., Pappas, M. and Moutesidis, K., 2008. Simulated cotton dye effluents treatment and reuse by nanofiltration. *Desalination*, *221*, pp.259-267.

58. Silva, T.L., Ronix, A., Pezoti, O., Souza, L.S., Leandro, P.K., Bedin, K.C., Beltrame, K.K., Cazetta, A.L. and Almeida, V.C., 2016. Mesoporous activated carbon from industrial laundry sewage sludge: adsorption studies of reactive dye Remazol Brilliant Blue R. *Chemical Engineering Journal*, *303*, pp.467-476.

59. Athanasekou, C.P., Likodimos, V. and Falaras, P., 2018. Recent developments of TiO_2 photocatalysis involving advanced oxidation and reduction reactions in water. *Journal of environmental chemical engineering*, *6*, pp.7386-7394.

60. Pawar, V., Jha, P.K., Panda, S.K., Jha, P.A. and Singh, P., 2018. Band-gap engineering in ZnO thin films: a combined experimental and theoretical study. *Physical Review Applied*, *9*, pp.054001.

61. Samsudin, E.M. and Hamid, S.B.A., 2017. Effect of band gap engineering in anionic-doped TiO_2 photocatalyst. *Applied Surface Science*, *391*, pp.326-336.

62. Luna, A.L., Valenzuela, M.A., Colbeau-Justin, C., Vázquez, P., Rodriguez, J.L., Avendaño, J.R., Alfaro, S., Tirado, S., Garduño, A. and José, M., 2016. Photocatalytic degradation of gallic acid over $CuO–TiO_2$ composites under UV/Vis LEDs irradiation. *Applied Catalysis A: General*, *521*, pp.140-148.

63. Orge, C.A., Faria, J.L. and Pereira, M.F.R., 2017. Photocatalytic ozonation of aniline with TiO_2-carbon composite materials. *Journal of environmental management*, *195*, pp.208-215.

64. Kanagamani, K., Muthukrishnan, P., Saravanakumar, K., Shankar, K. and Kathiresan, A., 2019. Photocatalytic degradation of environmental perilous gentian violet dye using leucaena-mediated zinc oxide nanoparticle and its anticancer activity. *Rare Metals*, *38*, pp.277-286.

65. Alwan, R.M., Kadhim, Q.A., Sahan, K.M., Ali, R.A., Mahdi, R.J., Kassim, N.A. and Jassim, A.N., 2015. Synthesis of zinc oxide nanoparticles via sol–gel route and their characterization. *Nanoscience and Nanotechnology*, *5*, pp.1-6.

66. Dasari, M., Godavarti, U. and Mote, V., 2018. Structural, morphological, magnetic and electrical properties of Ni-doped ZnO nanoparticles synthesized by co-precipitation method. *Process. Appl. Ceram.*, *12*, pp.100-110.

67. Mani, G.K. and Rayappan, J.B.B., 2014. Novel and facile synthesis of randomly interconnected ZnO nanoplatelets using spray pyrolysis and their room temperature sensing characteristics. *Sensors and Actuators B: Chemical*, *198*, pp.125-133.

68. Ealias, A.M. and Saravanakumar, M.P., 2017, November. A review on the classification, characterisation, synthesis of nanoparticles and their application. In *IOP Conf. Ser. Mater. Sci. Eng*, *263*, pp.032019.

69. Kennedy, O.W., Coke, M.L., White, E.R., Shaffer, M.S. and Warburton, P.A., 2018. MBE growth and morphology control of ZnO nanobelts with polar axis perpendicular to growth direction. *Materials Letters*, *212*, pp.51-53.

70. Svetlichnyi, V., Shabalina, A., Lapin, I., Goncharova, D. and Nemoykina, A., 2016. ZnO nanoparticles obtained by pulsed laser ablation and their composite with cotton fabric: Preparation and study of antibacterial activity. *Applied Surface Science*, *372*, pp.20-29.

71. Tripathi, R.M., Bhadwal, A.S., Gupta, R.K., Singh, P., Shrivastav, A. and Shrivastav, B.R., 2014. ZnO nanoflowers: novel biogenic synthesis and enhanced photocatalytic activity. *Journal of Photochemistry and Photobiology B: Biology*, *141*, pp.288-295.

72. Lu, J., Batjikh, I., Hurh, J., Han, Y., Ali, H., Mathiyalagan, R., Ling, C., Ahn, J.C. and Yang, D.C., 2019. Photocatalytic degradation of methylene blue using biosynthesized zinc oxide nanoparticles from bark extract of Kalopanax septemlobus. *Optik*, *182*, pp.980-985.

73. Benkhaya, S., M'rabet, S. and El Harfi, A., 2020. Classifications, properties, recent synthesis and applications of azo dyes. *Heliyon*, *6*, pp.03271.

74. Srivastava, R. and Singh, N., 2019. Importance of natural dye over synthetic dye: a critical. *International Journal of Home Science*, *5*, pp.148-150.

75. Ghaedi, M., Hajati, S., Barazesh, B., Karimi, F. and Ghezelbash, G., 2013. Saccharomyces cerevisiae for the biosorption of basic dyes from binary component systems and the high order derivative spectrophotometric method for simultaneous analysis of Brilliant green and Methylene blue. *Journal of Industrial and Engineering Chemistry*, *19*, pp.227-233.

76. Kumar, S.S., Balasubramanian, P. and Swaminathan, G., 2013. Degradation potential of free and immobilized cells of white rot fungus Phanerochaete chrysosporium on synthetic dyes. *International Journal of ChemTech Research*, *5*, pp.565-571.

77. Rangabhashiyam, S., Lata, S. and Balasubramanian, P., 2018. Biosorption characteristics of methylene blue and malachite green from simulated wastewater onto *Carica* papaya wood biosorbent. *Surfaces and Interfaces*, *10*, pp.197-215.

78. Mullineaux, C.W., 2017. Intracellular Diffusion: How bacteria keep proteins moving. *eLife*, *6*, pp.33590.

79. Rosselló-Móra, R. and Amann, R., 2015. Past and future species definitions for Bacteria and Archaea. *Systematic and Applied Microbiology*, *38*, pp.209-216.

80. Yusof, N.A.A., Zain, N.M. and Pauzi, N., 2019. Synthesis of ZnO nanoparticles with chitosan as stabilizing agent and their antibacterial properties against Gram-positive and Gram-negative bacteria. *International journal of biological macromolecules*, *124*, pp.1132-1136.

81. Momba, M.N.B., Osode, A.N. and Sibewu, M., 2006. The impact of inadequate wastewater treatment on the receiving water bodies–Case study: Buffalo City and Nkokonbe Municipalities of the Eastern Cape Province. *Water Sa*, *32*, pp.687-692.

82. Edokpayi, J.N., Odiyo, J.O., Popoola, E.O. and Msagati, T.A., 2018. Evaluation of microbiological and physicochemical parameters of alternative source of drinking water: a case study of nzhelele river, South Africa. *The open microbiology journal*, *12*, pp.18.

83. World Health Organization, 2003. *Nitrate and nitrite in drinking-water: Background document for development of WHO Guidelines for Drinking-water Quality* (No. WHO/SDE/WSH/04.03/56). World Health Organization.

84. Vargas-Reus, M.A., Memarzadeh, K., Huang, J., Ren, G.G. and Allaker, R.P., 2012. Antimicrobial activity of nanoparticulate metal oxides against peri-implantitis pathogens. *International journal of antimicrobial agents*, *40*, pp.135-139.

85. Elemike, E.E., Onwudiwe, D.C. and Singh, M., 2020. Eco-friendly synthesis of copper oxide, zinc oxide and copper oxide–zinc oxide nanocomposites, and their anticancer applications. *Journal of Inorganic and Organometallic Polymers and Materials*, *30*, pp.400-409.

86. Valero-Romero, M.J., Santaclara, J.G., Oar-Arteta, L., van Koppen, L., Osadchii, D.Y., Gascon, J. and Kapteijn, F., 2019. Photocatalytic properties of TiO_2 and Fe-doped TiO_2 prepared by metal organic framework-mediated synthesis. *Chemical Engineering Journal*, *360*, pp.75-88.

87. Christy, S.R., Priya, L.S., Durka, M., Dinesh, A., Babitha, N. and Arunadevi, S., 2019. Simple Combustion Synthesis, Structural, Morphological, Optical and Catalytic Properties of ZnO Nanoparticles. *Journal of nanoscience and nanotechnology*, *19*, pp.3564-3570.

88. Xu, C., Anusuyadevi, P.R., Aymonier, C., Luque, R. and Marre, S., 2019. Nanostructured materials for photocatalysis. *Chemical Society Reviews*, *48*, pp.3868-3902.

89. Anwar, H., Rana, B.C., Javed, Y., Mustafa, G., Ahmad, M.R., Jamil, Y. and Akhtar, H., 2018. Effect of ZnO on photocatalytic degradation of RhB and its inhibition activity for C. coli bacteria. *Russian Journal of Applied Chemistry*, *91*, pp.143-149.

90. Natarajan, T.S., Thampi, K.R. and Tayade, R.J., 2018. Visible light driven redox-mediator-free dual semiconductor photocatalytic systems for pollutant degradation and the ambiguity in applying Z-scheme concept. *Applied Catalysis B: Environmental*, *227*, pp.296-311.

91. Lin, J., Luo, Z., Liu, J. and Li, P., 2018. Photocatalytic degradation of methylene blue in aqueous solution by using ZnO-SnO_2 nanocomposites. *Materials Science in Semiconductor Processing*, *87*, pp.24-31.

92. Ishwarya, R., Vaseeharan, B., Kalyani, S., Banumathi, B., Govindarajan, M., Alharbi, N.S., Kadaikunnan, S., Al-anbr, M.N., Khaled, J.M. and Benelli, G., 2018. Facile green synthesis of zinc oxide nanoparticles using Ulva lactuca seaweed extract and evaluation of their photocatalytic, antibiofilm and insecticidal activity. *Journal of Photochemistry and Photobiology B: Biology*, *178*, pp.249-258.

93. Siripireddy, B. and Mandal, B.K., 2017. Facile green synthesis of zinc oxide nanoparticles by Eucalyptus globulus and their photocatalytic and antioxidant activity. *Advanced Powder Technology*, *28*, pp.785-797.

94. Hiremath, S., MAL, A.R., Prabha, C. and Vidya, C., 2018. Tamarindus indica mediated biosynthesis of nano TiO_2 and its application in photocatalytic degradation of Titan yellow. *Journal of environmental chemical engineering*, *6*, pp.7338-7346.

95. Khan, R. and Fulekar, M.H., 2016. Biosynthesis of titanium dioxide nanoparticles using Bacillus amyloliquefaciens culture and enhancement of its photocatalytic activity for the degradation of a sulfonated textile dye Reactive Red 31. *Journal of colloid and interface science*, *475*, pp.184-191.

96. Gnanasekaran, L., Hemamalini, R., Saravanan, R., Ravichandran, K., Gracia, F., Agarwal, S. and Gupta, V.K., 2017. Synthesis and characterization of metal oxides (CeO_2, CuO, NiO, Mn_3O_4, SnO_2 and ZnO) nanoparticles as photo catalysts for degradation of textile dyes. *Journal of Photochemistry and Photobiology B: Biology*, *173*, pp.43-49.

97. Honarmand, M.M., Mehr, M.E., Yarahmadi, M. and Siadati, M.H., 2019. Effects of different surfactants on morphology of TiO_2 and Zr-doped TiO_2 nanoparticles and their applications in MB dye photocatalytic degradation. *SN Applied Sciences*, *1*, pp.505.

98. Sahu, K., Singh, J., Satpati, B. and Mohapatra, S., 2018. Facile synthesis of ZnO nanoplates and nanoparticle aggregates for highly efficient photocatalytic degradation of organic dyes. *Journal of Physics and Chemistry of Solids*, *121*, pp.186-195.

99. Rao, M.P., Ponnusamy, V.K., Wu, J.J., Asiri, A.M. and Anandan, S., 2018. Hierarchical CuO microstructures synthesis for visible light driven photocatalytic degradation of Reactive Black-5 dye. *Journal of environmental chemical engineering*, *6*, pp.6059-6068.

100. Sorbiun, M., Mehr, E.S., Ramazani, A. and Fardood, S.T., 2018. Green synthesis of zinc oxide and copper oxide nanoparticles using aqueous extract of oak fruit hull (jaft) and comparing their photocatalytic degradation of basic violet 3. *International Journal of Environmental Research*, *12*, pp.29-37.

101. Jiang, P., Ren, D., He, D., Fu, W., Wang, J. and Gu, M., 2014. An easily sedimentable and effective TiO_2 photocatalyst for removal of dyes in water. *Separation and Purification Technology*, *122*, pp.128-132.

102. Balcha, A., Yadav, O.P. and Dey, T., 2016. Photocatalytic degradation of methylene blue dye by zinc oxide nanoparticles obtained from precipitation and sol-gel methods. *Environmental Science and Pollution Research*, *23*, pp.25485-25493.

103. Lee, C.G., Na, K.H., Kim, W.T., Park, D.C., Yang, W.H. and Choi, W.Y., 2019. TiO_2/ZnO Nanofibers Prepared by Electrospinning and Their Photocatalytic Degradation of Methylene Blue Compared with TiO_2 Nanofibers. *Applied Sciences*, *9*, pp.3404.

104. Khairy, M. and Zakaria, W., 2014. Effect of metal-doping of TiO_2 nanoparticles on their photocatalytic activities toward removal of organic dyes. *Egyptian Journal of Petroleum*, *23*, pp.419-426.

105. Soni, H., Kumar, J.N., Patel, K. and Kumar, R.N., 2016. Photocatalytic decoloration of three commercial dyes in aqueous phase and industrial effluents using TiO_2 nanoparticles. *Desalination and Water Treatment*, *57*, pp.6355-6364.

106. Udayabhanu, J., Kannan, V., Tiwari, M., Natesan, G., Giovanni, B. and Perumal, V., 2018. Nanotitania crystals induced efficient photocatalytic color degradation, antimicrobial and larvicidal activity. *Journal of Photochemistry and Photobiology B: Biology*, 178, pp.496-504.

107. He, Z., Que, W. and He, Y., 2013. Synthesis and characterization of bioinspired hierarchical mesoporous TiO_2 photocatalysts. *Materials Letters*, 94, pp.136-139.

108. Pal, S., Mondal, S., Maity, J. and Mukherjee, R., 2018. Synthesis and characterization of ZnO nanoparticles using moringa oleifera leaf extract: Investigation of photocatalytic and antibacterial activity. *International Journal of Nanoscience and Nanotechnology*, *14*, pp.111-119.

109. Raja, A., Ashokkumar, S., Marthandam, R.P., Jayachandiran, J., Khatiwada, C.P., Kaviyarasu, K., Raman, R.G. and Swaminathan, M., 2018. Eco-friendly preparation of zinc oxide nanoparticles using Tabernaemontana divaricata and its photocatalytic and antimicrobial activity. *Journal of Photochemistry and Photobiology B: Biology*, *181*, pp.53-58.

110. Khataee, A.R., Pons, M.N. and Zahraa, O., 2009. Photocatalytic degradation of three azo dyes using immobilized TiO_2 nanoparticles on glass plates activated by UV light irradiation: Influence of dye molecular structure. *Journal of Hazardous Materials*, *168*, pp.451-457.

111. Mehrjouei, M., Müller, S. and Möller, D., 2015. A review on photocatalytic ozonation used for the treatment of water and wastewater. *Chemical Engineering Journal*, *263*, pp.209-219.

112. Kanwal, A., Qaseem, S., Naeem, M., Ali, S.R., Shaffique, M. and Maqbool, M., 2019. Size-dependent inhibition of bacterial growth by chemically engineered spherical ZnO nanoparticles. *Journal of biological physics*, *45*, pp.147-159.

113. Raghupathi, K.R., Koodali, R.T. and Manna, A.C., 2011. Size-dependent bacterial growth inhibition and mechanism of antibacterial activity of zinc oxide nanoparticles. *Langmuir*, *27*, pp.4020-4028.

114. Agarwal, H., Menon, S., Kumar, S.V. and Rajeshkumar, S., 2018. Mechanistic study on antibacterial action of zinc oxide nanoparticles synthesized using green route. *Chemico-biological interactions*, *286*, pp.60-70.

115. Gabrielyan, L., Hovhannisyan, A., Gevorgyan, V., Ananyan, M. and Trchounian, A., 2019. Antibacterial effects of iron oxide (Fe_3O_4) nanoparticles: distinguishing concentration-dependent effects with different bacterial cells growth and membrane-associated mechanisms. *Applied microbiology and biotechnology*, *103*, pp.2773-2782.

116. Madan, H.R., Sharma, S.C., Suresh, D., Vidya, Y.S., Nagabhushana, H., Rajanaik, H., Anantharaju, K.S., Prashantha, S.C. and Maiya, P.S., 2016. Facile green fabrication of nanostructure ZnO plates, bullets, flower, prismatic tip, closed pine cone: their antibacterial, antioxidant, photoluminescent and photocatalytic properties. *Spectrochimica Acta Part A: Molecular and Biomolecular Spectroscopy*, 152, pp.404-416.

117. Zyoud, A.H., Dwikat, M., Al-Shakhshir, S., Ateeq, S., Ishtaiwa, J., Helal, M.H., Kharoof, M., Alami, S., Kelani, H., Campet, G. and Hilal, H.S., 2017. ZnO nanoparticles in complete photo-mineralization of aqueous gram negative bacteria and their organic content with direct solar light. *Solar Energy Materials and Solar Cells*, *168*, pp.30-37.

118. Zhang, L., Ding, Y., Povey, M. and York, D., 2008. ZnO nanofluids–A potential antibacterial agent. *Progress in Natural Science*, *18*, pp.939-944.

119. Exner, M., Bhattacharya, S., Christiansen, B., Gebel, J., Goroncy-Bermes, P., Hartemann, P., Heeg, P., Ilschner, C., Kramer, A., Larson, E. and Merkens, W., 2017. Antibiotic resistance: What is so special about multidrug-resistant Gram-negative bacteria? *GMS hygiene and infection control*, *12*, pp.1022.

120. Cheesman, M.J., Ilanko, A., Blonk, B. and Cock, I.E., 2017. Developing new antimicrobial therapies: are synergistic combinations of plant extracts/compounds with conventional antibiotics the solution? *Pharmacognosy reviews*, *11*, pp.57.

121. Swathi, N., Sandhiya, D., Rajeshkumar, S. and Lakshmi, T., 2019. Green synthesis of titanium dioxide nanoparticles using Cassia fistula and its antibacterial activity. *International Journal of Research in Pharmaceutical Sciences*, *10*, pp.856-860.

122. Dadi, R., Azouani, R., Traore, M., Mielcarek, C. and Kanaev, A., 2019. Antibacterial activity of ZnO and CuO nanoparticles against gram positive and gram negative strains. *Materials Science and Engineering: C*, *104*, pp.109968.

123. Sharmila, G., Thirumarimurugan, M. and Muthukumaran, C., 2019. Green synthesis of ZnO nanoparticles using Tecoma castanifolia leaf extract: Characterization and evaluation of its antioxidant, bactericidal and anticancer activities. *Microchemical Journal*, *145*, pp.578-587.

124. Amanulla, A.M. and Sundaram, R., 2019. Green synthesis of TiO_2 nanoparticles using orange peel extract for antibacterial, cytotoxicity and humidity sensor applications. *Materials Today: Proceedings*, *8*, pp.323-331.

125. Azam, A., Ahmed, A.S., Oves, M., Khan, M.S. and Memic, A., 2012. Size-dependent antimicrobial properties of CuO nanoparticles against Gram-positive and-negative bacterial strains. *International journal of nanomedicine*, *7*, pp.3527.

126. Ramesh, M., Anbuvannan, M. and Viruthagiri, G., 2015. Green synthesis of ZnO nanoparticles using Solanum nigrum leaf extract and their antibacterial activity. *Spectrochimica Acta Part A: Molecular and Biomolecular Spectroscopy*, *136*, pp.864-870.

127. Subhapriya, S. and Gomathipriya, P., 2018. Green synthesis of titanium dioxide (TiO_2) nanoparticles by Trigonella foenum-graecum extract and its antimicrobial properties. *Microbial pathogenesis*, *116*, pp.215-220.

128. Bhutiya, P.L., Mahajan, M.S., Rasheed, M.A., Pandey, M., Hasan, S.Z. and Misra, N., 2018. Zinc oxide nanorod clusters deposited seaweed cellulose sheet for antimicrobial activity. *International journal of biological macromolecules*, *112*, pp.1264-1271.

129. Akhter, S.M.H., Mahmood, Z., Ahmad, S. and Mohammad, F., 2018. Plant-mediated green synthesis of zinc oxide nanoparticles using Swertia chirayita leaf extract, characterization and its antibacterial efficacy against some common pathogenic bacteria. *BioNanoScience*, *8*(3), pp.811-817.

130. Dhandapani, P., Siddarth, A.S., Kamalasekaran, S., Maruthamuthu, S. and Rajagopal, G., 2014. Bio-approach: ureolytic bacteria mediated synthesis of ZnO

nanocrystals on cotton fabric and evaluation of their antibacterial properties. *Carbohydrate polymers*, *103*, pp.448-455.

133. Akhter, S.M.H., Mohammad, F. and Ahmad, S., 2019. Terminalia belerica Mediated Green Synthesis of Nanoparticles of Copper, Iron and Zinc Metal Oxides as the Alternate Antibacterial Agents Against some Common Pathogens. *BioNanoScience*, *9*, pp.365-372.

134. Thirumalai Arasu, V., Prabhu, D. and Soniya, M., 2010. Stable silver nanoparticle synthesizing methods and its applications. *J. Bio. Sci. Res*, *1*, pp.259-270.

135. Foo, K.L., Hashim, U., Muhammad, K. and Voon, C.H., 2014. Sol–gel synthesized zinc oxide nanorods and their structural and optical investigation for optoelectronic application. *Nanoscale research letters*, *9*, p.429.

136. Feynman, R.P., 1960. There's plenty of room at the bottom. *California Institute of Technology, Engineering and Science magazine*, 7, pp. 1-10.

137. Wu, P., Feng, L., Liang, Y., Zhang, X., Mahmoudi, B. and Kazemnejadi, M., 2020. Magnetic Fe-CO-Mo alloy nano-rods prepared from chemical decomposition of a screw (a top-down approach): An efficient and cheap catalyst for the preparation of dihydropyridine and dihydropyrimidone derivatives. *Applied Catalysis A: General*, *590*, pp.117301.

138. Navale, S.T., Jadhav, V.V., Tehare, K.K., Sagar, R.U.R., Biswas, C.S., Galluzzi, M., Liang, W., Patil, V.B., Mane, R.S. and Stadler, F.J., 2017. Solid-state synthesis strategy of ZnO nanoparticles for the rapid detection of hazardous Cl_2. *Sensors and Actuators B: Chemical*, *238*, pp.1102-1110.

139. Ahmed, S., Chaudhry, S.A. and Ikram, S., 2017. A review on biogenic synthesis of ZnO nanoparticles using plant extracts and microbes: a prospect towards green chemistry. *Journal of Photochemistry and Photobiology B: Biology*, *166*, pp.272-284.

140. Lingaraju, K., Naika, H.R., Nagabhushana, H. and Nagaraju, G., 2019. Euphorbia heterophylla (L.) mediated fabrication of ZnO NPs: characterization and evaluation of antibacterial and anticancer properties. *Biocatalysis and Agricultural Biotechnology*, *18*, pp.100894.

141. Brimson, J.M., Onlamoon, N., Tencomnao, T. and Thitilertdecha, P., 2019. Clerodendrum petasites S. Moore: The therapeutic potential of phytochemicals, hispidulin, vanillic acid, verbascoside, and apigenin. *Biomedicine & Pharmacotherapy*, *118*, pp.109319.

142. Sharmila, G., Muthukumaran, C., Sandiya, K., Santhiya, S., Pradeep, R.S., Kumar, N.M., Suriyanarayanan, N. and Thirumarimurugan, M., 2018. Biosynthesis, characterization, and antibacterial activity of zinc oxide nanoparticles derived from Bauhinia tomentosa leaf extract. *Journal of Nanostructure in Chemistry*, *8*, pp.293-299.

143. Fatemi, M., Mollania, N., Momeni-Moghaddam, M. and Sadeghifar, F., 2018. Extracellular biosynthesis of magnetic iron oxide nanoparticles by Bacillus cereus strain HMH1: Characterization and in vitro cytotoxicity analysis on MCF-7 and 3T3 cell lines. *Journal of biotechnology*, *270*, pp.1-11.

144. Subbaiya, R., Saravanan, M., Priya, A.R., Shankar, K.R., Selvam, M., Ovais, M., Balajee, R. and Barabadi, H., 2017. Biomimetic synthesis of silver nanoparticles from Streptomyces atrovirens and their potential anticancer activity against human breast cancer cells. *IET nanobiotechnology*, *11*, pp.965-972.

145. He, S., Guo, Z., Zhang, Y., Zhang, S., Wang, J. and Gu, N., 2007. Biosynthesis of gold nanoparticles using the bacteria Rhodopseudomonas capsulata. *Materials Letters*, *61*, pp.3984-3987.

146. Ahmad, A., Senapati, S., Khan, M.I., Kumar, R., Ramani, R., Srinivas, V. and Sastry, M., 2003. Intracellular synthesis of gold nanoparticles by a novel alkalotolerant actinomycete, Rhodococcus species. *Nanotechnology*, *14*, p.824.

147. Pugazhenthiran, N., Anandan, S., Kathiravan, G., Prakash, N.K.U., Crawford, S. and Ashokkumar, M., 2009. Microbial synthesis of silver nanoparticles by Bacillus sp. *Journal of Nanoparticle Research*, *11*, p.1811.

148. Camas, M., Camas, A.S. and Kyeremeh, K., 2018. Extracellular Synthesis and Characterization of Gold Nanoparticles Using Mycobacterium sp. BRS2A-AR2 Isolated from the Aerial Roots of the Ghanaian Mangrove Plant, Rhizophora racemosa. *Indian journal of microbiology*, *58*, pp.214-221.

149. Rajendran, K., Karunagaran, V., Mahanty, B. and Sen, S., 2015. Biosynthesis of hematite nanoparticles and its cytotoxic effect on HepG2 cancer cells. *International journal of biological macromolecules*, *74*, pp.376-381.

150. Ibrahem, K.H., Salman, J.A.S. and Ali, F.A., 2014. Effect of Titanium Nanoparticles Biosynthesis by Lactobacillus Crispatus on Urease, Hemolysin& Biofilm Forming by Some Bacteria Causing Recurrent UTI in Iraqi Women. *European Scientific Journal*, *10*, pp.1-9.

151.. Jayaseelan, C., Rahuman, A.A., Roopan, S.M., Kirthi, A.V., Venkatesan, J., Kim, S.K., Iyappan, M. and Siva, C., 2013. Biological approach to synthesize TiO_2 nanoparticles using Aeromonas hydrophila and its antibacterial activity. *Spectrochimica Acta Part A: Molecular and Biomolecular Spectroscopy*, *107*, pp.82-89.

152. Taran, M., Rad, M. and Alavi, M., 2017. Antibacterial activity of copper oxide (CuO) nanoparticles biosynthesized by Bacillus sp. FU4: optimization of experiment design. *Pharmaceutical Sciences*, *23*, pp.198-206.

153. Rajan, A., Cherian, E. and Baskar, G., 2016. Biosynthesis of zinc oxide nanoparticles using Aspergillus fumigatus JCF and its antibacterial activity. *Int J Mod Sci Technol*, *1*, pp.52-7.

154. El-Batal, A.I., El-Sayyad, G.S., Mosallam, F.M. and Fathy, R.M., 2020. Penicillium chrysogenum-mediated mycogenic synthesis of copper oxide nanoparticles using gamma rays for in vitro antimicrobial activity against some plant pathogens. *Journal of Cluster Science*, *31*, pp.79-90.

155. Órdenes-Aenishanslins, N.A., Saona, L.A., Durán-Toro, V.M., Monrás, J.P., Bravo, D.M. and Pérez-Donoso, J.M., 2014. Use of titanium dioxide nanoparticles biosynthesized by Bacillus mycoides in quantum dot sensitized solar cells. *Microbial cell factories*, *13*, pp.90.

156. Singh, B.N., Rawat, A.K.S., Khan, W., Naqvi, A.H. and Singh, B.R., 2014. Biosynthesis of stable antioxidant ZnO nanoparticles by Pseudomonas aeruginosa rhamnolipids. *PLoS One*, *9*, pp.106937.

157. Dhandapani, P., Siddarth, A.S., Kamalasekaran, S., Maruthamuthu, S. and Rajagopal, G., 2014. Bio-approach: ureolytic bacteria mediated synthesis of ZnO nanocrystals on cotton fabric and evaluation of their antibacterial properties. *Carbohydrate polymers*, *103*, pp.448-455.

158. Kirthi, A.V., Rahuman, A.A., Rajakumar, G., Marimuthu, S., Santhoshkumar, T., Jayaseelan, C., Elango, G., Zahir, A.A., Kamaraj, C. and Bagavan, A., 2011. Biosynthesis of titanium dioxide nanoparticles using bacterium Bacillus subtilis. *Materials Letters*, *65*, pp.2745-2747.

159. Mashrai, A., Khanam, H. and Aljawfi, R.N., 2017. Biological synthesis of ZnO nanoparticles using C. albicans and studying their catalytic performance in the synthesis of steroidal pyrazolines. *Arabian Journal of Chemistry*, *10*, pp.1530-1536.

160. Gopinath, K., Karthika, V., Sundaravadivelan, C., Gowri, S. and Arumugam, A., 2015. Mycogenesis of cerium oxide nanoparticles using Aspergillus niger culture filtrate and their applications for antibacterial and larvicidal activities. *Journal of Nanostructure in Chemistry*, *5*, pp.295-303.

161. Matinise, N., Fuku, X.G., Kaviyarasu, K., Mayedwa, N. and Maaza, M., 2017. ZnO nanoparticles via Moringa oleifera green synthesis: physical properties & mechanism of formation. *Applied Surface Science*, *406*, pp.339-347.

162. Jeronsia, J.E., Joseph, L.A., Vinosha, P.A., Mary, A.J. and Das, S.J., 2019. Camellia sinensis leaf extract mediated synthesis of copper oxide nanostructures for potential biomedical applications. *Materials Today: Proceedings*, *8*, pp.214-222.

163. Madan, H.R., Sharma, S.C., Suresh, D., Vidya, Y.S., Nagabhushana, H., Rajanaik, H., Anantharaju, K.S., Prashantha, S.C. and Maiya, P.S., 2016. Facile green fabrication of nanostructure ZnO plates, bullets, flower, prismatic tip, closed pine cone: their antibacterial, antioxidant, photoluminescent and photocatalytic properties. *Spectrochimica Acta Part A: Molecular and Biomolecular Spectroscopy*, *152*, pp.404-416

164. Kalaiselvi, A., Roopan, S.M., Madhumitha, G., Ramalingam, C., Al-Dhabi, N.A. and Arasu, M.V., 2016. Catharanthus roseus-mediated zinc oxide nanoparticles against photocatalytic application of phenol red under UV@ 365 nm. *CURRENT SCIENCE*, *111*, pp.1811.

165. Ganesan, S., Babu, I.G., Mahendran, D., Arulselvi, P.I., Elangovan, N., Geetha, N. and Venkatachalam, P., 2016. Green engineering of titanium dioxide nanoparticles using Ageratina altissima (L.) King & HE Robines. medicinal plant aqueous leaf extracts for enhanced photocatalytic activity. *Ann. Phytomed.*, *5*, pp.69-75.

166. Stan, M., Popa, A., Toloman, D., Dehelean, A., Lung, I. and Katona, G., 2015. Enhanced photocatalytic degradation properties of zinc oxide nanoparticles synthesized by using plant extracts. *Materials Science in Semiconductor Processing*, *39*, pp.23-29.

167. Surendra, T.V., Roopan, S.M., Al-Dhabi, N.A., Arasu, M.V., Sarkar, G. and Suthindhiran, K., 2016. Vegetable peel waste for the production of ZnO nanoparticles and its toxicological efficiency, antifungal, hemolytic, and antibacterial activities. *Nanoscale research letters*, *11*, pp.546.

168. Sundrarajan, M., Ambika, S. and Bharathi, K., 2015. Plant-extract mediated synthesis of ZnO nanoparticles using Pongamia pinnata and their activity against pathogenic bacteria. *Advanced Powder Technology*, *26*, pp.1294-1299.

169. Khatami, M., Varma, R.S., Zafarnia, N., Yaghoobi, H., Sarani, M. and Kumar, V.G., 2018. Applications of green synthesized Ag, ZnO and Ag/ZnO nanoparticles for making clinical antimicrobial wound-healing bandages. *Sustainable Chemistry and Pharmacy*, *10*, pp.9-15.

170. Pallela, P.N.V.K., Ummey, S., Ruddaraju, L.K., Kollu, P., Khan, S. and Pammi, S.V.N., 2019. Antibacterial activity assessment and characterization of green synthesized CuO nano rods using Asparagus racemosus roots extract. *SN Applied Sciences*, *1*, p.421.

171. Thakur, B.K., Kumar, A. and Kumar, D., 2019. Green synthesis of titanium dioxide nanoparticles using Azadirachta indica leaf extract and evaluation of their antibacterial activity. *South African Journal of Botany*, *124*, pp.223-227.

172. Ramesh, M., Anbuvannan, M. and Viruthagiri, G., 2015. Green synthesis of ZnO nanoparticles using Solanum nigrum leaf extract and their antibacterial activity. *Spectrochimica Acta Part A: Molecular and Biomolecular Spectroscopy*, *136*, pp.864-870.

173. Awwad, A.M. and Amer, M.W., 2020. Biosynthesis of copper oxide nanoparticles using Ailanthus altissima leaf extract and antibacterial activity. *Chemistry International*, *6*, pp.210-217.

174. Kashale, A.A., Gattu, K.P., Ghule, K., Ingole, V.H., Dhanayat, S., Sharma, R., Chang, J.Y. and Ghule, A.V., 2016. Biomediated green synthesis of TiO_2 nanoparticles for lithium ion battery application. *Composites Part B: Engineering*, *99*, pp.297-304.

175. Chatterjee, A., Ajantha, M., Talekar, A., Revathy, N. and Abraham, J., 2017. Biosynthesis, antimicrobial and cytotoxic effects of titanium dioxide nanoparticles using Vigna unguiculata seeds. *Materials Letters.*, *9*, pp.95-99.

176. Santhoshkumar, T., Rahuman, A.A., Jayaseelan, C., Rajakumar, G., Marimuthu, S., Kirthi, A.V., Velayutham, K., Thomas, J., Venkatesan, J. and Kim, S.K., 2014. Green synthesis of titanium dioxide nanoparticles using Psidium guajava extract and its antibacterial and antioxidant properties. *Asian Pacific journal of tropical medicine*, *7*, pp.968-976

177. Murali, M., Mahendra, C., Rajashekar, N., Sudarshana, M.S., Raveesha, K.A. and Amruthesh, K.N., 2017. Antibacterial and antioxidant properties of biosynthesized zinc oxide nanoparticles from Ceropegia candelabrum L.–an endemic species. *Spectrochimica Acta Part A: Molecular and Biomolecular Spectroscopy*, *179*, pp.104-109.

178. Bhutiya, P.L., Mahajan, M.S., Rasheed, M.A., Pandey, M., Hasan, S.Z. and Misra, N., 2018. Zinc oxide nanorod clusters deposited seaweed cellulose sheet for antimicrobial activity. *International journal of biological macromolecules*, *112*, pp.1264-1271.

179. Khatami, M., Alijani, H.Q., Heli, H. and Sharifi, I., 2018. Rectangular shaped zinc oxide nanoparticles: Green synthesis by Stevia and its biomedical efficiency. *Ceramics International*, *44*, pp.15596-15602.

180. Nagaraj, E., Karuppannan, K., Shanmugam, P. and Venugopal, S., 2019. Exploration of bio-synthesized copper oxide nanoparticles using pterolobium hexapetalum leaf extract by photocatalytic activity and biological evaluations. *Journal of Cluster Science*, *30*, pp.1157-1168.

181. Ngoepe, N.M., Mbita, Z., Mathipa, M., Mketo, N., Ntsendwana, B. and Hintsho-Mbita, N.C., 2018. Biogenic synthesis of ZnO nanoparticles using Monsonia burkeana for use in photocatalytic, antibacterial and anticancer applications. *Ceramics International*, *44*, pp.16999-17006.

182. Sharmila, G., Muthukumaran, C., Sandiya, K., Santhiya, S., Pradeep, R.S., Kumar, N.M., Suriyanarayanan, N. and Thirumarimurugan, M., 2018. Biosynthesis, characterization, and antibacterial activity of zinc oxide nanoparticles derived from Bauhinia tomentosa leaf extract. *Journal of Nanostructure in Chemistry*, *8*, pp.293-299.

183. Mahlaule-Glory, L.M., Mbita, Z., Ntsendwana, B., Mathipa, M.M., Mketo, N. and Hintsho-Mbita, N.C., 2019. ZnO nanoparticles via Sutherlandia frutescens plant extract: physical and biological properties. *Materials Research Express*, *6*, pp.085006.

184. Elemike, E.E., Onwudiwe, D.C. and Singh, M., 2020. Eco-friendly synthesis of copper oxide, zinc oxide and copper oxide–zinc oxide nanocomposites, and their anticancer applications. *Journal of Inorganic and Organometallic Polymers and Materials*, *30*, pp.400-409.

185. Al-Hadeethi, Y., Umar, A., Al-Heniti, S.H., Kumar, R., Kim, S.H., Zhang, X. and Raffah, B.M., 2017. 2D Sn-doped ZnO ultrathin nanosheet networks for enhanced acetone gas sensing application. *Ceramics International*, *43*, pp.2418-2423.

186. Bhuyan, T., Mishra, K., Khanuja, M., Prasad, R. and Varma, A., 2015. Biosynthesis of zinc oxide nanoparticles from Azadirachta indica for antibacterial and photocatalytic applications. *Materials Science in Semiconductor Processing*, *32*, pp.55-61.

187. Karnan, T. and Selvakumar, S.A.S., 2016. Biosynthesis of ZnO nanoparticles using rambutan (Nephelium lappaceumL.) peel extract and their photocatalytic activity on methyl orange dye. *Journal of molecular Structure*, *1125*, pp.358-365.

188. Ong, C.B., Ng, L.Y. and Mohammad, A.W., 2018. A review of ZnO nanoparticles as solar photocatalysts: synthesis, mechanisms and applications. *Renewable and Sustainable Energy Reviews*, *81*, pp.536-551.

189. Erhart, P. and Albe, K., 2006. Diffusion of zinc vacancies and interstitials in zinc oxide. *Applied physics letters*, *88*, pp.201918.

190. Fu, L. and Fu, Z., 2015. Plectranthus amboinicus leaf extract–assisted biosynthesis of ZnO nanoparticles and their photocatalytic activity. *Ceramics International*, *41*, pp.2492-2496.

191. Ma, S.S., Xu, P., Cai, Z.L., Li, Q., Ye, Z.L. and Zhou, Y.M., 2018. Template-Assisted Hydrothermal Growth of One-Dimensional Zinc Oxide Nanowires for Photocatalytic Application. *Journal of nanoscience and nanotechnology*, *18*, pp.5113-5118.

192. Bhattacharjee, A. and Ahmaruzzaman, M., 2018. α-Amino acid assisted facile synthesis of two-dimensional ZnO nanotriangles for removal of noxious pollutants from water phase. *Journal of Environmental Chemical Engineering*, *6*, pp.4970-4979.

193. Zhu, L., Li, Y. and Zeng, W., 2018. Hydrothermal synthesis of hierarchical flower-like ZnO nanostructure and its enhanced ethanol gas-sensing properties. *Applied Surface Science*, 427, pp.281-287.

194. Hassan, N.K., Hashim, M.R. and Bououdina, M., 2013. One-dimensional ZnO nanostructure growth prepared by thermal evaporation on different substrates: ultraviolet emission as a function of size and dimensionality. *Ceramics International*, *39*, pp.7439-7444.

195. Ju, D., Xu, H., Zhang, J., Guo, J. and Cao, B., 2014. Direct hydrothermal growth of ZnO nanosheets on electrode for ethanol sensing. *Sensors and Actuators B: Chemical*, *201*, pp.444-451.

196. Zhang, X., Qin, J., Xue, Y., Yu, P., Zhang, B., Wang, L. and Liu, R., 2014. Effect of aspect ratio and surface defects on the photocatalytic activity of ZnO nanorods. *Scientific reports*, *4*, p.4596.

197. Kusior, A., Banas, J., Trenczek-Zajac, A., Zubrzycka, P., Micek-Ilnicka, A. and Radecka, M., 2018. Structural properties of TiO_2 nanomaterials. *Journal of Molecular Structure*, *1157*, pp.327-336.

198. Allen, N.S., Mahdjoub, N., Vishnyakov, V., Kelly, P.J. and Kriek, R.J., 2018. The effect of crystalline phase (anatase, brookite and rutile) and size on the photocatalytic activity of calcined polymorphic titanium dioxide (TiO_2). *Polymer degradation and stability*, *150*, pp.31-36.

199. Maheu, C., Cardenas, L., Puzenat, E., Afanasiev, P. and Geantet, C., 2018. UPS and UV spectroscopies combined to position the energy levels of TiO_2 anatase and rutile nanopowders. *Physical Chemistry Chemical Physics*, *20*, pp.25629-25637.

200. Reyes-Coronado, D., Rodríguez-Gattorno, G., Espinosa-Pesqueira, M.E., Cab, C., de Coss, R.D. and Oskam, G., 2008. Phase-pure TiO_2 nanoparticles: anatase, brookite and rutile. *Nanotechnology*, *19*, p.145605.

201. Choudhury, B. and Choudhury, A., 2014. Oxygen defect dependent variation of band gap, Urbach energy and luminescence property of anatase, anatase–rutile mixed phase and of rutile phases of TiO_2 nanoparticles. *Physica E: Low-Dimensional Systems and Nanostructures*, *56*, pp.364-371.

202. Lin, S.H., Chiou, C.H., Chang, C.K. and Juang, R.S., 2011. Photocatalytic degradation of phenol on different phases of TiO_2 particles in aqueous suspensions under UV irradiation. *Journal of environmental management*, *92*, pp.3098-3104.

203. Elsellami, L., Dappozze, F., Fessi, N., Houas, A. and Guillard, C., 2018. Highly photocatalytic activity of nanocrystalline TiO_2 (anatase, rutile) powders prepared from $TiCl_4$ by sol–gel method in aqueous solutions. *Process Safety and Environmental Protection*, *113*, pp.109-121.

204. Sang, L., Zhao, Y. and Burda, C., 2014. TiO_2 nanoparticles as functional building blocks. *Chemical reviews*, *114*, pp.9283-9318.

205. Landmann, M., Rauls, E. and Schmidt, W.G., 2012. The electronic structure and optical response of rutile, anatase and brookite TiO_2. *Journal of physics: condensed matter*, *24*, pp.195503.

206. Chamanzadeh, Z., Noormohammadi, M. and Zahedifar, M., 2017. Enhanced photovoltaic performance of dye sensitized solar cell using TiO_2 and ZnO nanoparticles on top of free standing TiO_2 nanotube arrays. *Materials Science in Semiconductor Processing*, *61*, pp.107-113.

207. Sagadevan, S., Vennila, S., Lett, J.A., Marlinda, A.R., Hamizi, N.A.B. and Johan, M.R., 2019. Tailoring the structural, morphological, optical, thermal and dielectric characteristics of ZnO nanoparticles using starch as a capping agent. *Results in Physics*, *15*, pp.102543.

208. Geetha, N., Sivaranjani, S., Ayeshamariam, A., Siva Bharathy, M., Nivetha, S., Kaviyarasu, K. and Jayachandran, M., 2018. High performance photo-catalyst based on nanosized ZnO–TiO_2 nanoplatelets for removal of RhB under visible light irradiation. *Journal of Advanced Microscopy Research*, *13*, pp.12-19.

209. Brahmia, O., 2016. Photocatalytic degradation of a textile dye under UV and solar light irradiation using TiO_2 and ZnO nanoparticles. *International Journal Advance Chem Enginnering Biological Science*, *3*, pp.225-227.

210. da Trindade, L.G., Hata, G.Y., Souza, J.C., Soares, M.R., Leite, E.R., Pereira, E.C., Longo, E. and Mazzo, T.M., 2020. Preparation and characterization of hematite nanoparticles-decorated zinc oxide particles (ZnO/Fe_2O_3) as photoelectrodes for solar cell applications. *Journal of Materials Science*, *55*, pp.2923-2936.

211. Hassan, S.M., Ahmed, A.I. and Mannaa, M.A., 2018. Structural, photocatalytic, biological and catalytic properties of SnO_2/TiO_2 nanoparticles. *Ceramics International*, *44*, pp.6201-6211.

212. James, E.M., Barr, T.J. and Meyer, G.J., 2018. Evidence for an Electronic State at the Interface between the SnO_2 Core and the TiO_2 Shell in Mesoporous SnO_2/TiO_2 Thin Films. *ACS Applied Energy Materials*, *1*, pp.859-867.

213. Gnanasekaran, L., Hemamalini, R., Rajendran, S., Qin, J., Yola, M.L., Atar, N. and Gracia, F., 2019. Nanosized Fe_3O_4 incorporated on a TiO_2 surface for the enhanced photocatalytic degradation of organic pollutants. *Journal of Molecular Liquids*, *287*, pp.110967.

214. Yang, C.C., Doong, R.A., Chen, K.F., Chen, G.S. and Tsai, Y.P., 2018. The photocatalytic degradation of methylene blue by green semiconductor films that is induced by irradiation by a light-emitting diode and visible light. *Journal of the Air & Waste Management Association*, *68*, pp.29-38.

215. Luna, A.L., Valenzuela, M.A., Colbeau-Justin, C., Vázquez, P., Rodriguez, J.L., Avendaño, J.R., Alfaro, S., Tirado, S., Garduño, A. and José, M., 2016. Photocatalytic degradation of gallic acid over CuO–TiO_2 composites under UV/Vis LEDs irradiation. *Applied Catalysis A: General*, *521*, pp.140-148.

216. Saeed, M., Muneer, M., Khosa, M.K.K., Akram, N., Khalid, S., Adeel, M., Nisar, A. and Sherazi, S., 2019. Azadirachta indica leaves extract assisted green synthesis of Ag-TiO_2 for degradation of Methylene blue and Rhodamine B dyes in aqueous medium. *Green Processing and Synthesis*, *8*, pp.659-666.

217. Huang, J.H., Chen, J.X., Tu, Y.F., Tian, Y., Zhou, D., Zheng, G., Sang, J.P. and Fu, Q.M., 2018. Preparation and photocatalytic activity of CuO/ZnO composite nanostructured films. *Materials Research Express*, *6*, p.015035.

218. Bharathi, P., Harish, S., Archana, J., Navaneethan, M., Ponnusamy, S., Muthamizhchelvan, C., Shimomura, M. and Hayakawa, Y., 2019. Enhanced charge transfer and separation of hierarchical CuO/ZnO composites: The synergistic effect of photocatalysis for the mineralization of organic pollutant in water. *Applied Surface Science*, *484*, pp.884-891.

219. Adnan, M.M., Julkapli, N.M., Amir, M.N.I. and Maamor, A., 2019. Effect on different TiO_2 photocatalyst supports on photodecolorization of synthetic dyes: a review. *International journal of environmental science and technology*, *16*, pp.547-566.

220. Natarajan, T.S., Lee, J.Y., Bajaj, H.C., Jo, W.K. and Tayade, R.J., 2017. Synthesis of multiwall carbon nanotubes/TiO_2 nanotube composites with enhanced photocatalytic decomposition efficiency. *Catalysis Today*, *282*, pp.13-23.

221. Saud, P.S., Pant, B., Alam, A.M., Ghouri, Z.K., Park, M. and Kim, H.Y., 2015. Carbon quantum dots anchored TiO_2 nanofibers: Effective photocatalyst for waste water treatment. *Ceramics International*, *41*, pp.11953-11959.

222. Tie, W., Zheng, Z., Xu, C., Zheng, Z., Bhattacharyya, S.S., He, W. and Lee, S.H., 2019. Facile synthesis of carbon nanotubes covalently modified with ZnO nanorods for enhanced photodecomposition of dyes. *Journal of colloid and interface science*, *537*, pp.652-660.

223. Singhal, S., Dixit, S. and Shukla, A.K., 2018. Self-assembly of the Ag deposited ZnO/carbon nanospheres: A resourceful photocatalyst for efficient photocatalytic degradation of methylene blue dye in water. Advanced Powder Technology, *29*, pp.3483-3492.

224. Allègre, C.J., Poirier, J.P., Humler, E. and Hofmann, A.W., 1995. The chemical composition of the Earth. *Earth and Planetary Science Letters*, *134*, pp.515-526.

225. Pace, N.R., 2001. The universal nature of biochemistry. *Proceedings of the National Academy of Sciences*, *98*, pp.805-808.

226. Ohfuji, H., Irifune, T., Litasov, K.D., Yamashita, T., Isobe, F., Afanasiev, V.P. and Pokhilenko, N.P., 2015. Natural occurrence of pure nano-polycrystalline diamond from impact crater. *Scientific reports*, *5*, pp.14702.

227. Luque, F.J., Huizenga, J.M., Crespo-Feo, E., Wada, H., Ortega, L. and Barrenechea, J.F., 2014. Vein graphite deposits: geological settings, origin, and economic significance. *Mineralium Deposita*, *49*, pp.261-277.

228. Kroto, H.W., Heath, J.R., O'Brien, S.C., Curl, R.F. and Smalley, R.E., 1985. C60: Buckminsterfullerene. *Nature*, *318*, pp.162.

229. Che, G., Lakshmi, B.B., Martin, C.R., Fisher, E.R. and Ruoff, R.S., 1998. Chemical vapor deposition based synthesis of carbon nanotubes and nanofibers using a template method. *Chemistry of Materials*, *10*, pp.260-267.

230. Khan, M.M., Khan, W., Kumar, A. and Alhazaa, A.N., 2018. Plasma enhanced chemical vapour deposition growth and physical properties of single-walled carbon nanotubes. *Materials Letters*, *219*, pp.269-272.

231. Bronner, C., Durr, R.A., Rizzo, D.J., Lee, Y.L., Marangoni, T., Kalayjian, A.M., Rodriguez, H., Zhao, W., Louie, S.G., Fischer, F.R. and Crommie, M.F., 2018. Hierarchical on-surface synthesis of graphene nanoribbon heterojunctions. *ACS nano*, *12*, pp.2193-2200.

232. Liu, Z., Zhou, Z., Xiong, W. and Zhang, Q., 2018. Controlled synthesis of carbon nanospheres via the modulation of the hydrophilic length of the assembled surfactant micelles. *Langmuir*, *34*, pp.10389-10396.

233. Miao, X., Qu, D., Yang, D., Nie, B., Zhao, Y., Fan, H. and Sun, Z., 2018. Synthesis of carbon dots with multiple color emission by controlled graphitization and surface functionalization. *Advanced Materials*, *30*, pp.1704740.

234. Adam, M., Hart, A., Stevens, L.A., Wood, J., Robinson, J.P. and Rigby, S.P., 2018. Microwave synthesis of carbon onions in fractal aggregates using heavy oil as a precursor. *Carbon*, *138*, pp.427-435.

235. Bayat, N., Rezaei, M. and Meshkani, F., 2016. Hydrogen and carbon nanofibers synthesis by methane decomposition over Ni–Pd/Al_2O_3 catalyst. *International Journal of Hydrogen Energy*, *41*, pp.5494-5503.

236. Zhao, X., Chen, H., Kong, F., Zhang, Y., Wang, S., Liu, S., Lucia, L.A., Fatehi, P. and Pang, H., 2019. Fabrication, characteristics and applications of carbon materials with different morphologies and porous structures produced from wood liquefaction: a review. *Chemical Engineering Journal*, *364*, pp.226-243.

237. Zdolšek, N., Rocha, R.P., Krstić, J., Trtić-Petrović, T., Šljukić, B., Figueiredo, J.L. and Vujković, M.J., 2019. Electrochemical investigation of ionic liquid-derived porous carbon materials for supercapacitors: pseudocapacitance versus electrical double layer. *Electrochimica Acta*, *298*, pp.541-551.

238. Ruoff, R.S. and Lorents, D.C., 1995. Mechanical and thermal properties of carbon nanotubes. *carbon*, *33*, pp.925-930.

239. Sarkar, B., Mandal, S., Tsang, Y.F., Kumar, P., Kim, K.H. and Ok, Y.S., 2018. Designer carbon nanotubes for contaminant removal in water and wastewater: A critical review. *Science of the Total Environment*, *612*, pp.561-581.

240. Laka, K., Kganyago, P., Mketo, N., Tetana, Z.N., Hintsho-Mbita, N.C. and Mbita, Z., 2018. Fly Ash Derived β-Cyclodextrin Carbon Nanospheres as Potential Drug Delivery Vehicles. *Advanced Science, Engineering and Medicine*, *10*, pp.9-13.

241. Xu, F., Tang, Z., Huang, S., Chen, L., Liang, Y., Mai, W., Zhong, H., Fu, R. and Wu, D., 2015. Facile synthesis of ultrahigh-surface-area hollow carbon nanospheres for enhanced adsorption and energy storage. *Nature communications*, *6*, p.7221.

242. Kundu, S., Chowdhury, I.H. and Naskar, M.K., 2018. Hierarchical porous carbon nanospheres for efficient removal of toxic organic water contaminants of phenol and methylene blue. *Journal of Chemical & Engineering Data*, *63*, pp.559-573.

243. Nieto-Márquez, A., Romero, R., Romero, A. and Valverde, J.L., 2011. Carbon nanospheres: synthesis, physicochemical properties and applications. *Journal of Materials chemistry*, *21*, pp.1664-1672.

244. Gutiérrez-García, C.J., Ambriz-Torres, J.M., de Jesús Contreras-Navarrete, J., Granados-Martínez, F.G., García-Ruiz, D.L., García-González, L., Zamora-Peredo, L., Ortega-Varela, L.F., Richaud, A., Méndez, F. and Domratcheva-Lvova, L., 2019. Synthesis of carbon spheres by atmospheric pressure chemical vapor deposition from a serial of aromatic hydrocarbon precursors. *Physica E: Low-dimensional Systems and Nanostructures*, *112*, pp.78-85.

245. Xiong, H., Moyo, M., Motchelaho, M.A., Tetana, Z.N., Dube, S.M., Jewell, L.L. and Coville, N.J., 2014. Fischer–Tropsch synthesis: Iron catalysts supported on N-doped carbon spheres prepared by chemical vapor deposition and hydrothermal approaches. *Journal of catalysis*, *311*, pp.80-87.

246. Huang, S., Gao, Y., Zhang, Y., Chen, S. and Xiao, Q., 2019. Thermal oxidation etching strategy towards mesoporous hollow carbon spheres. *Materials Letters*, *240*, pp.253-257.

247. Teo, K.B., Singh, C., Chowalla, M. and Milne, W.I., 2003. Catalytic synthesis of carbon nanotubes and nanofibers. *Encyclopedia of nanoscience and nanotechnology*, *10*, pp.1-22.

248. Merchan-Merchan, W., Saveliev, A.V., Kennedy, L. and Jimenez, W.C., 2010. Combustion synthesis of carbon nanotubes and related nanostructures. *Progress in Energy and Combustion Science*, *36*, pp.696-727.

249. Lobo, L.S., 2017. Nucleation and growth of carbon nanotubes and nanofibers: mechanism and catalytic geometry control. *Carbon*, *114*, pp.411-417.

250. Martin-Gullon, I., Vera, J., Conesa, J.A., González, J.L. and Merino, C., 2006. Differences between carbon nanofibers produced using Fe and Ni catalysts in a floating catalyst reactor. *Carbon*, *44*, pp.1572-1580.

251. Vera-Agullo, J., Varela-Rizo, H., Conesa, J.A., Almansa, C., Merino, C. and Martin-Gullon, I., 2007. Evidence for growth mechanism and helix-spiral cone structure of stacked-cup carbon nanofibers. *Carbon*, *45*, pp.2751-2758.

252. Zheng, G.B., Kouda, K., Sano, H., Uchiyama, Y., Shi, Y.F. and Quan, H.J., 2004. A model for the structure and growth of carbon nanofibers synthesized by the CVD method using nickel as a catalyst. *Carbon*, *42*, pp.635-640.

253. Rambau, K.M., Musyoka, N.M., Manyala, N., Ren, J., Langmi, H.W. and Mathe, M.K., 2018. Preparation of carbon nanofibers/tubes using waste tyres pyrolysis oil and coal fly ash derived catalyst. *Journal of Environmental Science and Health, Part A*, *53*, pp.1115-1122.

254. Yuan, Z., Cheng, X., Zhong, L., Wu, R. and Zheng, Y., 2019. Preparation, characterization and performance of an electrospun carbon nanofiber mat applied in hexavalent chromium removal from aqueous solution. *Journal of Environmental Sciences*, *77*, pp.75-84.

255. Kenzhin, R.M., Bauman, Y.I., Volodin, A.M., Mishakov, I.V. and Vedyagin, A.A., 2018. Synthesis of carbon nanofibers by catalytic CVD of chlorobenzene over bulk nickel alloy. *Applied Surface Science*, *427*, pp.505-510.

256. Díaz, J.A., Martínez-Fernández, M., Romero, A. and Valverde, J.L., 2013. Synthesis of carbon nanofibers supported cobalt catalysts for Fischer–Tropsch process. *Fuel*, *111*, pp.422-429.

257. Suda, Y., Maruyama, K., Iida, T., Takikawa, H., Ue, H., Shimizu, K. and Umeda, Y., 2015. High-yield synthesis of helical carbon nanofibers using iron oxide fine powder as a catalyst. *Crystals*, *5*, pp.47-60.

258. Hlekelele, L., Franklyn, P.J., Dziike, F. and Durbach, S.H., 2018. TiO_2 composited with carbon nanofibers or nitrogen-doped carbon nanotubes synthesized using coal fly ash as a catalyst: bisphenol-A photodegradation efficiency evaluation. *New Journal of Chemistry*, *42*, pp.4531-4542.

259. Hoekstra, J., Geus, J.W. and Jenneskens, L.W., BASF Corp, 2018. *Process for producing carbon nanofibers and/or carbon nanotubes*. U.S. Patent Application 10/010,867.

260. Hintsho, N., Shaikjee, A., Masenda, H., Naidoo, D., Billing, D., Franklyn, P. and Durbach, S., 2014. Direct synthesis of carbon nanofibers from South African coal fly ash. *Nanoscale research letters*, *9*, pp.387.

261. Hintsho, N., Shaikjee, A., Tripathi, P.K., Franklyn, P. and Durbach, S., 2015. The effect of CO 2 on the CVD synthesis of carbon nanomaterials using fly ash as a catalyst. *RSC Advances*, *5*, pp.53776-53781.

262. Hintsho, N., Shaikjee, A., Triphati, P.K., Masenda, H., Naidoo, D., Franklyn, P. and Durbach, S., 2016. Effect of nitrogen and hydrogen gases on the synthesis of carbon nanomaterials from coal waste fly ash as a catalyst. *Journal of nanoscience and nanotechnology*, *16*, pp.4672-4683.

263. Smith, R., Ventura, D. and Prince, J.T., 2015. LC-MS alignment in theory and practice: a comprehensive algorithmic review. *Briefings in bioinformatics*, *16*, pp.104-117.

264. Gulcin, I., Kaya, R., Goren, A.C., Akincioglu, H., Topal, M., Bingol, Z., Cetin Çakmak, K., Ozturk Sarikaya, S.B., Durmaz, L. and Alwasel, S., 2019. Anticholinergic, antidiabetic and antioxidant activities of Cinnamon (Cinnamomum verum) bark extracts: polyphenol contents analysis by LC-MS/MS. *International Journal of Food Properties*, *22*, pp.1511-1526.

265. Betts, T.A. and Palkendo, J.A., 2018. Teaching undergraduates LC–MS/MS theory and operation via multiple reaction monitoring (MRM) method development. *Journal of Chemical Education*, *95*, pp.1035-1039.

266. Qu, W., Yuan, T., Yin, G., Xu, S., Zhang, Q. and Su, H., 2019. Effect of properties of activated carbon on malachite green adsorption. *Fuel*, *249*, pp.45-53.

267. Mouni, L., Belkhiri, L., Bollinger, J.C., Bouzaza, A., Assadi, A., Tirri, A., Dahmoune, F., Madani, K. and Remini, H., 2018. Removal of Methylene Blue from aqueous solutions by adsorption on Kaolin: Kinetic and equilibrium studies. *Applied Clay Science*, *153*, pp.38-45.

268. Goldstein, J.I., Newbury, D.E., Michael, J.R., Ritchie, N.W., Scott, J.H.J. and Joy, D.C., 2017. *Scanning electron microscopy and X-ray microanalysis*. *4*, pp.65-121.

269. Qi, W., Du, J., Peng, Y., Wu, W., Zhang, Z., Li, X., Li, K., Zhang, K., Gong, C., Luo, M. and Peng, H., 2018. Hydrothermal synthesis of TiO_2 nanorods arrays on ITO. *Materials Chemistry and Physics*, *207*, pp.435-441.

270. Tavengwa, N.T., Hintsho, N., Durbach, S., Weiersbye, I., Cukrowska, E. and Chimuka, L., 2016. Extraction of explosive compounds from aqueous solutions by solid phase extraction using β-cyclodextrin functionalized carbon nanofibers as sorbents. *Journal of environmental chemical engineering*, *4*, pp.2450-2457.

271. Cunha, R., Paupitz, R., Yoon, K., Van Duin, A.C., Elías, A.L., Carozo, V., Dasgupta, A., Fujisawa, K., Lopez, N.P., Araujo, P.T. and Terrones, M., 2018. Raman spectroscopy revealing noble gas adsorption on single-walled carbon nanotube bundles. *Carbon*, *127*, pp.312-319.

272. Zhang, K., Wang, J., Zou, J., Cai, W. and Zhang, Q., 2018. Low excitation of Raman D band in [2+ 1] cycloaddition functionalized single-walled carbon nanotubes. *Carbon*, *138*, pp.188-196.

273. Korepanov, V.I., Chan, S.Y., Hsu, H.C. and Hamaguchi, H.O., 2019. Phonon confinement and size effect in Raman spectra of ZnO nanoparticles. *Heliyon*, *5*, pp.01222.

275. Kasinathan, K., Kennedy, J., Elayaperumal, M., Henini, M. and Malik, M., 2016. Photodegradation of organic pollutants RhB dye using UV simulated sunlight on ceria based TiO_2 nanomaterials for antibacterial applications. *Scientific reports*, *6*, pp.38064.

276. Haider, A.J., AL–Anbari, R.H., Kadhim, G.R. and Salame, C.T., 2017. Exploring potential environmental applications of TiO_2 nanoparticles. *Energy Procedia*, *119*, pp.332-345.

277. Viter, R., Tereshchenko, A., Smyntyna, V., Ogorodniichuk, J., Starodub, N., Yakimova, R., Khranovskyy, V. and Ramanavicius, A., 2017. Toward development of optical biosensors based on photoluminescence of TiO_2 nanoparticles for the detection of Salmonella. *Sensors and Actuators B: Chemical*, *252*, pp.95-102.

278. Pellegrino, F., Pellutiè, L., Sordello, F., Minero, C., Ortel, E., Hodoroaba, V.D. and Maurino, V., 2017. Influence of agglomeration and aggregation on the

photocatalytic activity of TiO_2 nanoparticles. *Applied Catalysis B: Environmental*, *216*, pp.80-87.

279. Munir, S., Shah, S.M. and Hussain, H., 2016. Effect of carrier concentration on the optical band gap of TiO_2 nanoparticles. *Materials & Design*, *92*, pp.64-72.

280. Fazio, G., Ferrighi, L. and Di Valentin, C., 2015. Spherical versus faceted anatase TiO_2 nanoparticles: a model study of structural and electronic properties. *The Journal of Physical Chemistry C*, *119*, pp.20735-20746.

281. Rosales, M., Zoltan, T., Yadarola, C., Mosquera, E., Gracia, F. and García, A., 2019. The influence of the morphology of 1D TiO_2 nanostructures on photogeneration of reactive oxygen species and enhanced photocatalytic activity. *Journal of Molecular Liquids*, *281*, pp.59-69.

282. Wasly, H.S., El-Sadek, M.A. and Batoo, K.M., 2019. Novel synthesis, structural, optical properties and antibacterial activity of ZnO nanoparticles. *Materials Research Express*, *6*, pp.055003.

283. Senguttuvan, J., Paulsamy, S. and Karthika, K., 2014. Phytochemical analysis and evaluation of leaf and root parts of the medicinal herb, Hypochaeris radicata L. for in vitro antioxidant activities. *Asian Pacific journal of tropical biomedicine*, *4*, pp.359-367.

284. Mamphiswana, N.D., Mashela, P.W. and Mdee, L.K., 2010. Distribution of total phenolics and antioxidant activity in fruit, leaf, stem and root of Monsonia burkeana. *African Journal of Agricultural Research*, *5*, pp.2570-2575.

285. Kassim, M., Achoui, M., Mustafa, M.R., Mohd, M.A. and Yusoff, K.M., 2010. Ellagic acid, phenolic acids, and flavonoids in Malaysian honey extracts demonstrate in vitro anti-inflammatory activity. *Nutrition research*, *30*, pp.650-659.

286. Bhuyan, T., Mishra, K., Khanuja, M., Prasad, R. and Varma, A., 2015. Biosynthesis of zinc oxide nanoparticles from *Azadirachta indica* for antibacterial and photocatalytic applications. *Materials Science in Semiconductor Processing*, *32*, pp.55-61.

287. Pan, Z., Lin, Y., Sarkar, B., Owens, G. and Chen, Z., 2020. Green synthesis of iron nanoparticles using red peanut skin extract: Synthesis mechanism,

characterization and effect of conditions on chromium removal. *Journal of Colloid and Interface Science*, *558*, pp.106-114.

288. Peter, I.J., Praveen, E., Vignesh, G. and Nithiananthi, P., 2017. ZnO nanostructures with different morphology for enhanced photocatalytic activity. *Materials Research Express*, *4*, pp.124003.

289. Gao, L., Li, Y., Ren, J., Wang, S., Wang, R., Fu, G. and Hu, Y., 2017. Passivation of defect states in anatase TiO_2 hollow spheres with Mg doping: realizing efficient photocatalytic overall water splitting. *Applied Catalysis B: Environmental*, *202*, pp.127-133.

290. Peng, T., Ray, S., Veeravalli, S.S., Lalman, J.A. and Arefi-Khonsari, F., 2018. The role of hydrothermal conditions in determining 1D TiO_2 nanomaterials bandgap energies and crystal phases. *Materials Research Bulletin*, *105*, pp.104-113.

291. Houas, A., Lachheb, H., Ksibi, M., Elaloui, E., Guillard, C. and Herrmann, J.M., 2001. Photocatalytic degradation pathway of methylene blue in water. *Applied Catalysis B: Environmental*, *31*, pp.145-157.

292. Bubacz, K., Choina, J., Dolat, D. and Morawski, A.W., 2010. Methylene Blue and Phenol Photocatalytic Degradation on Nanoparticles of Anatase TiO_2. *Polish Journal of Environmental Studies*, *19*, pp.685-691.

293. Han, C., Yang, H. and Xue, X., 2015. Kinetics of photocatalytic degradation of methylene blue over $CaTiO_3$. *Journal of Wuhan University of Technology-Mater. Sci. Ed.*, *30*, pp.1103-1107.

294. Ling, C.M., Mohamed, A.R. and Bhatia, S., 2004. Performance of photocatalytic reactors using immobilized TiO_2 film for the degradation of phenol and methylene blue dye present in water stream. *Chemosphere*, *57*, pp.547-554.

295. Kaur, J., Bansal, S. and Singhal, S., 2013. Photocatalytic degradation of methyl orange using ZnO nanopowders synthesized via thermal decomposition of oxalate precursor method. *Physica B: Condensed Matter*, *416*, pp.33-38.

296. Trandafilović, L.V., Jovanović, D.J., Zhang, X., Ptasińska, S. and Dramićanin, M.D., 2017. Enhanced photocatalytic degradation of methylene blue and methyl

orange by ZnO: Eu nanoparticles. *Applied Catalysis B: Environmental*, *203*, pp.740-752.

297. Sivalingam, G., Priya, M.H. and Madras, G., 2004. Kinetics of the photodegradation of substituted phenols by solution combustion synthesized TiO_2. *Applied Catalysis B: Environmental*, *51*, pp.67-76.

298. Gnanaprakasam, A., Sivakumar, V.M., Sivayogavalli, P.L. and Thirumarimurugan, M., 2015. Characterization of TiO_2 and ZnO nanoparticles and their applications in photocatalytic degradation of azodyes. *Ecotoxicology and environmental safety*, *121*, pp.121-125.

299. Ashajyothi, C., Harish, K.H., Dubey, N. and Chandrakanth, R.K., 2016. Antibiofilm activity of biogenic copper and zinc oxide nanoparticles-antimicrobials collegiate against multiple drug resistant bacteria: a nanoscale approach. *Journal of Nanostructure in Chemistry*, *6*, pp.329-341.

300. Liu, J.Z., Jellbauer, S., Poe, A.J., Ton, V., Pesciaroli, M., Kehl-Fie, T.E., Restrepo, N.A., Hosking, M.P., Edwards, R.A., Battistoni, A. and Pasquali, P., 2012. Zinc sequestration by the neutrophil protein calprotectin enhances Salmonella growth in the inflamed gut. *Cell host & microbe*, *11*, pp.227-239.

301. Tetana, Z.N., 2014. *Boron and nitrogen doped carbons for photochemical degradation reactions* (Doctoral dissertation), pp.157.

302. Mutuma, B.K., Matsoso, B.J., Ranganathan, K., Keartland, J.M., Wamwangi, D. and Coville, N.J., 2017. Generation of radical species in CVD grown pristine and N-doped solid carbon spheres using H_2 and Ar as carrier gases. *RSC advances*, *7*, pp.21187-21195.

303. Mhlanga, S.D., Coville, N.J., Iyuke, S.E., Afolabi, A.S., Abdulkareem, A.S. and Kunjuzwa, N., 2010. Controlled syntheses of carbon spheres in a swirled floating catalytic chemical vapour deposition vertical reactor. *Journal of Experimental Nanoscience*, *5*, pp.40-51.

304. Pasini, S.M., Batistella, M.A., de Souza, S.M.G.U., Wang, J., Hotza, D. and de Souza, A.A.U., 2019. Thermal degradation and flammability of TiO_2–polyetherimide nanocomposite fibers. *Polymer Bulletin*, *77*, pp.1-22.

305. Mansfield, E., Kar, A. and Hooker, S.A., 2010. Applications of TGA in quality control of SWCNTs. *Analytical and bioanalytical chemistry*, *396*, pp.1071-1077.

306. Wang KH, Hsieh YH, Wu CH., 2000. The pH and anion effects on the heterogeneous photocatalytic degradation of o–methylbenzoic acid in TiO_2 aqueous suspension. *Chemosphere*, 2000;40, pp.389–394.

307. Kumar, A. and Pandey, G., 2017. A review on the factors affecting the photocatalytic degradation of hazardous materials. *Material. Science. Enginnering. International. Journal*, *1*, pp.1-10.

308. Bazli, L., Siavashi, M. and Shiravi, A., 2019. A review of carbon nanotube/TiO_2 composite prepared via sol-gel method. *Journal of Composites and Compounds*, *1*, pp.1-9.

309. Cao, Q., Yu, Q., Connell, D.W. and Yu, G., 2013. Titania/carbon nanotube composite (TiO_2/CNT) and its application for removal of organic pollutants. *Clean Technologies and Environmental Policy*, *15*, pp.871-880.

Appendices

Supplementary

Chapter 4: Mass spectrum of *Monsonia burkeana* water extract and Tauc plot

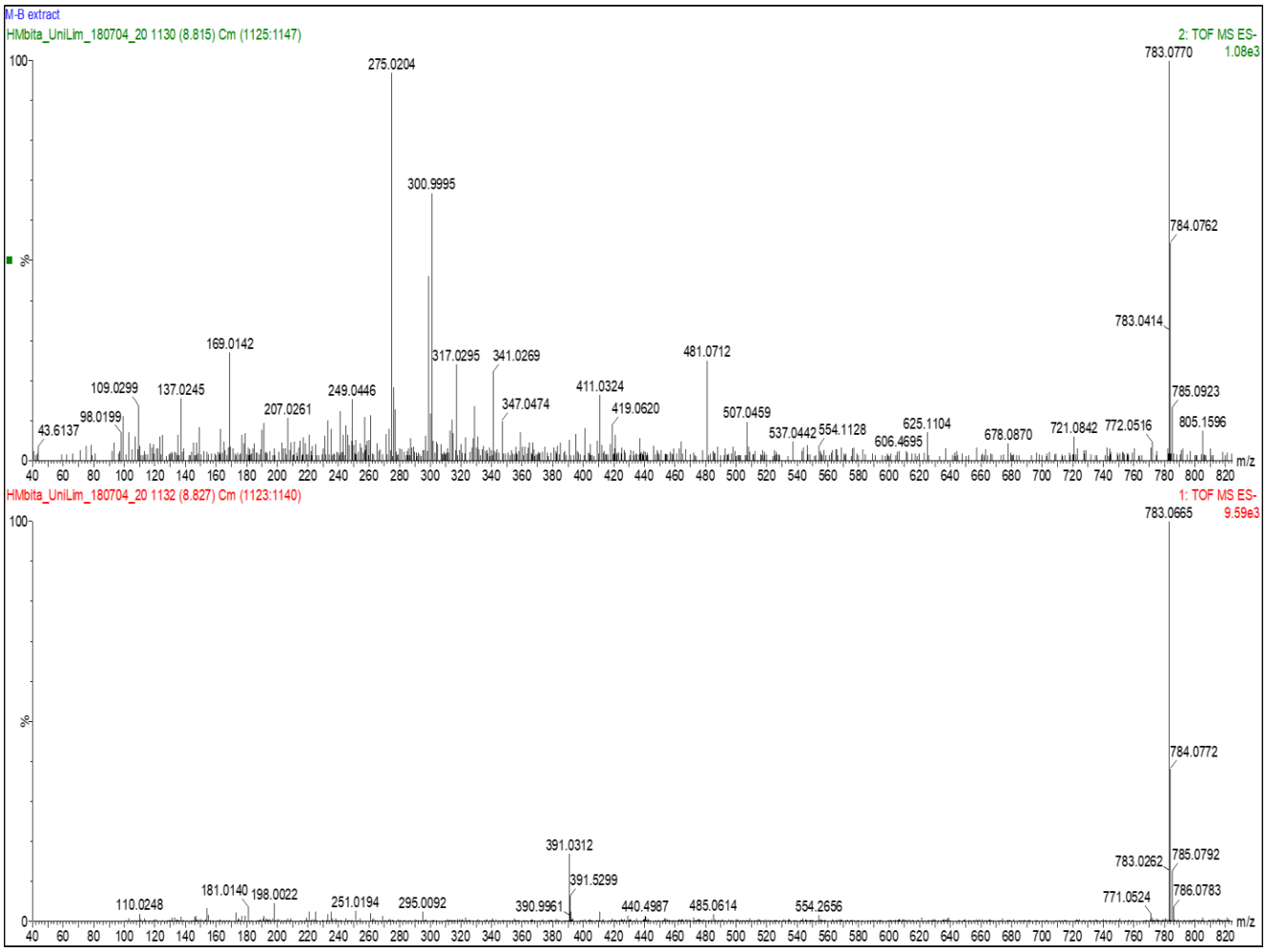

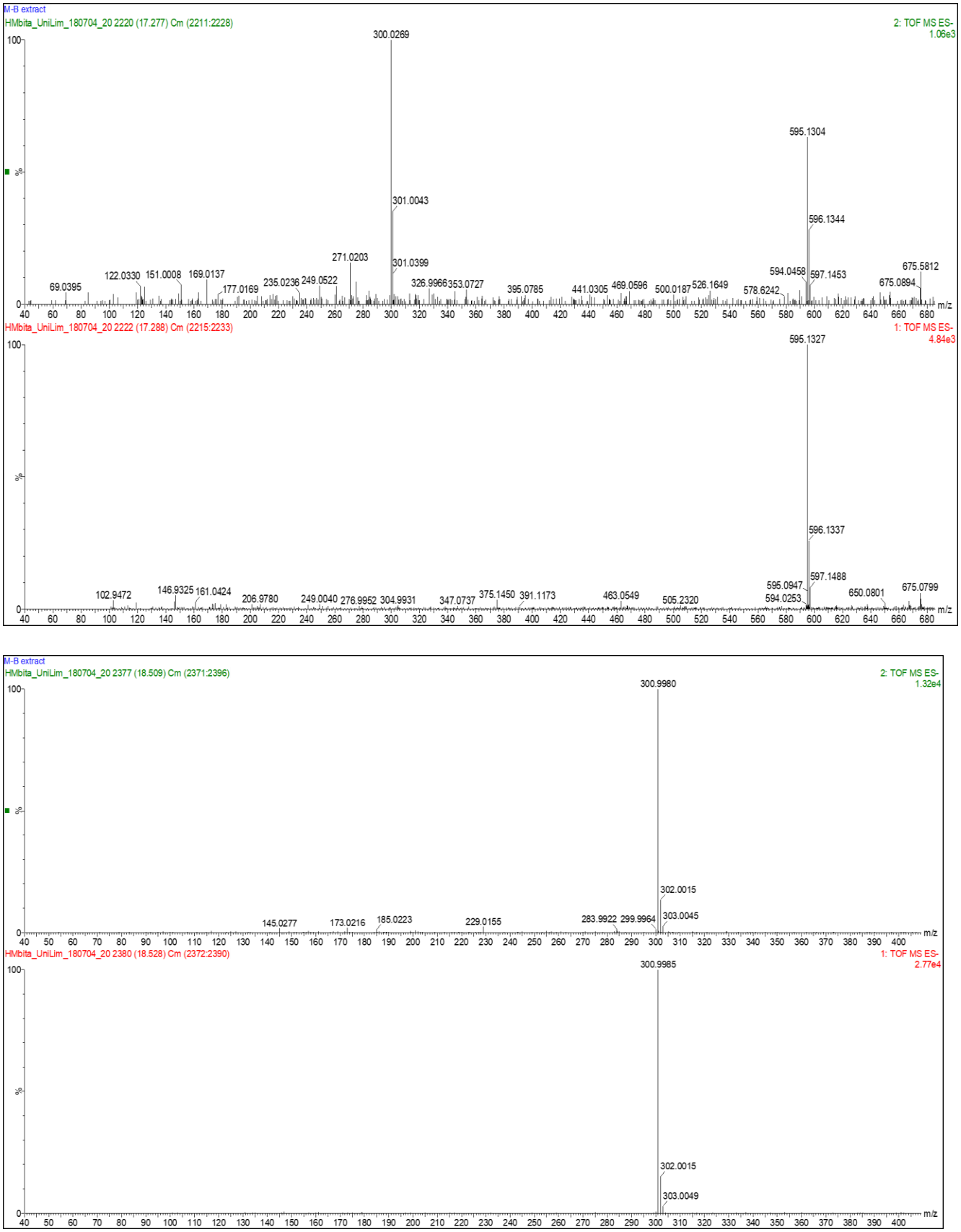

Figure S1 1: Mass spectrum of *Monsonia burkeana* water extract.

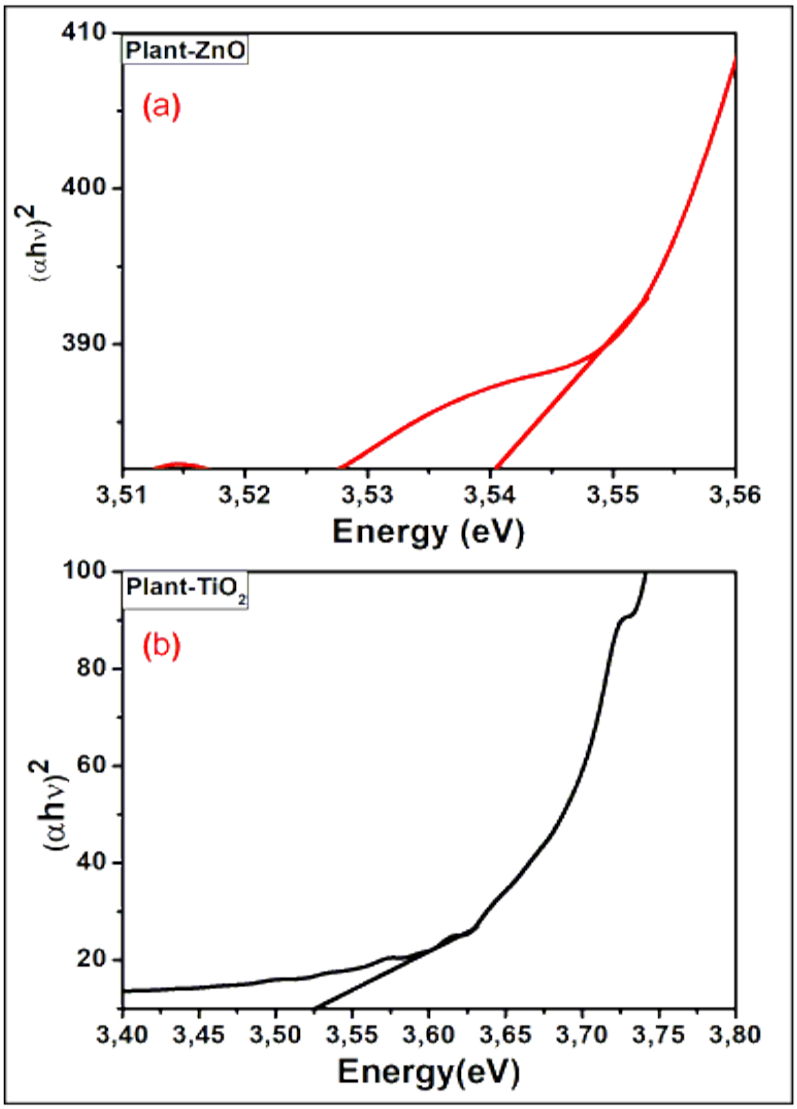

Figure S1 2: Tauc plot of (a) ZnO and (b)TiO_2 nanoparticles.

Chapter 5: EDS Spectra of the various synthesised metal oxide composites

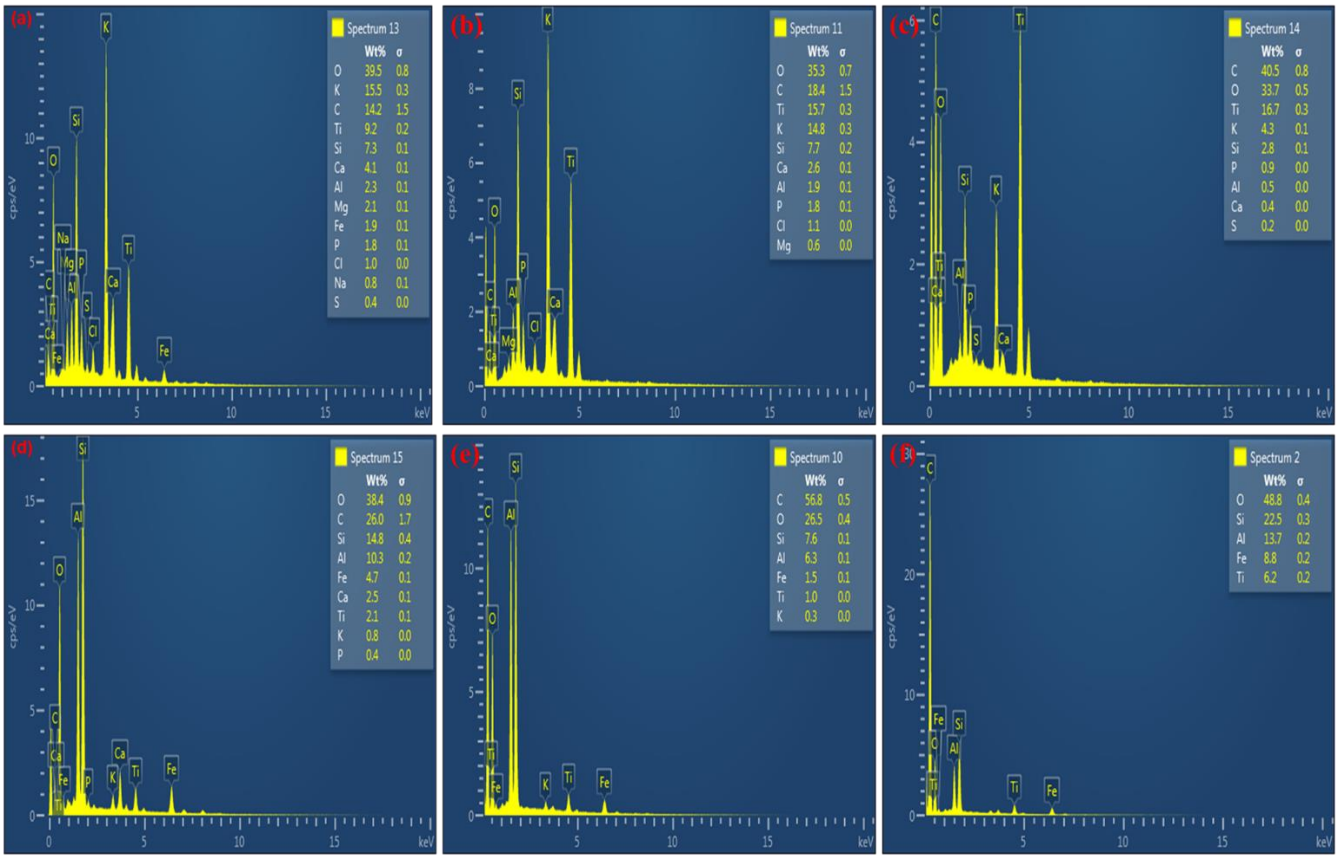

Figure S1 3: EDS (a) 5%TiO_2/CSs (b) 10%TiO_2/CSs (c) 20%-TiO_2/CSs (d) 5%-TiO_2/CNFs (e) 10%-TiO_2/CNFs (f) 20%-TiO_2/CNFs.

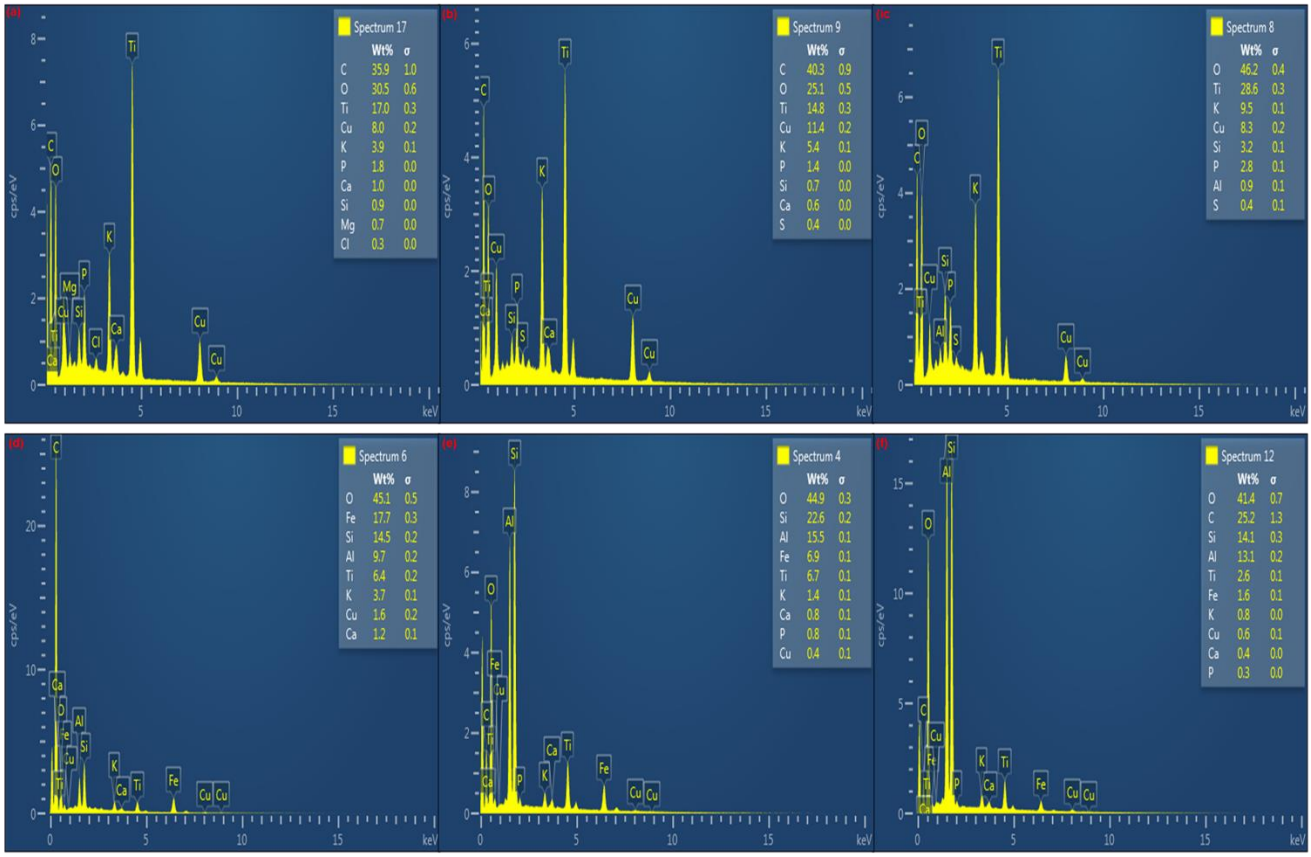

Figure S1 4: EDS (a) 2%-CuO/TiO_2/CSs (b) 6%-CuO/TiO_2/CSs (c) 10%-CuO/TiO_2/CSs (d) 2%-CuO/TiO_2/CNFs (e) 6%-CuO/TiO_2/CNFs (f) 10%-CuO/TiO_2/CNFs.